NORTHWESTERN UNIVERSITY

Nanoscale Surface Engineering of Solid Oxide Electrochemical Cell Electrodes for Stability Enhancement, Characterization, and Reactivation

A DISSERTATION

SUBMITTED TO THE GRADUATE SCHOOL
IN PARTIAL FULFILLMENT OF THE REQUIREMENTS

for the degree

DOCTOR OF PHILOSOPHY

Materials Science and Engineering

By

Travis Anthony Schmauss

EVANSTON, ILLINOIS

June 2022

© Copyright Travis Anthony Schmauss 2022

All Rights Reserved

Abstract

Solid oxide fuel and electrolysis cells (SOFCs and SOECs) must be engineered with the entire lifetime of their performance in mind. Electrochemical activity will decrease as degradative processes take effect, leading to higher overpotentials and decreased power outputs. Materials science and engineering can stave off these inefficiencies through an understanding of degradative mechanisms while allowing the development of strategies to overcome, reverse, or mitigate them.

Degradative processes occur most acutely in the electrodes of the cells, both in the oxygen and the fuel electrode; this dissertation explores both. For the former, atomic layer deposition (ALD) is investigated as a strategy to abate the degradation associated with the coarsening of nanoparticle-infiltrated systems, electrode architectures that have very high initial performance for the oxygen reduction reaction, but which, due to the mobility of the surface particles at the operating temperatures of SOFCs, rapidly reduce their catalytic area. The system under consideration is ALD-ZrO_2 atop the perovskite $Sr_{0.5}Sm_{0.5}CoO_{3-\delta}$ infiltrated into Gd-doped ceria. ALD coverage is found to be highly prone to deposition gradients based on the complexity of electrode microstructure: higher aspect ratios lead to increased rates of impingement on electrode surfaces, each collision a chance for thermal decomposition of the organometallic precursor.

The understanding borne of the limitations of ALD then leads to the development of a method that leverages a truly ideal ALD precursor, trimethylaluminum, which forms conformal Al_2O_3 even through microstructurally complex infiltrated electrodes. In this case, however, Al_2O_3 is electrochemically inert, and its function is instead in serving as a mold, cast around electrode surface features, one that can then be digested and quantified using acids and plasma spectroscopy to back-calculate the exact surface area covered. This technique fits a niche for measuring the

surface areas of relatively low (~cm^2) absolute surface area sintered electrodes, useful for solid oxide electrode development and possibly for other heterogenous catalysts.

Attention switches to the fuel electrode, in which a promising class of electrode based on the perovskite structure, but with reducible cations, forms socketed surface metal particles upon exposure to fuel environments. The systems explored are the (Ni,Fe) and (Ru,Fe) alloy forming Fe, Ni, and Ru-doped strontium titanate perovskites (STFN and STFR). One principle benefit of an all-oxide-supported fuel electrode is redox stability; this is investigated by redox-cycling STFN after long periods of time (250 h) in reducing atmosphere, in which performance degrades due to phase decomposition of the perovskite to a Ruddlesden-Popper phase as Fe concomitantly reduces, further enriching the (Ni,Fe) exsolved particles. After redox cycling, performance is regained, but Ni does not fully re-incorporate into the perovskite lattice. Upon subsequent re-reduction, the existing NiO phase left behind acts as a nucleation site for metal reduction, and the areal density of exsolved particles decreases while average particle size increases. While redox cycling cannot completely reverse decomposition, it can completely burn out solid carbon deposited via operation in C-based fuel environment; this effect is demonstrated with STFR benchmarked against a conventional cermet anode.

Finally, an analytic study is presented that focuses on SOFCs in combination with carbon capture in the context of vehicles. Given the unique ability of the SOFC to output a concentrated stream of CO_2 when operating on energy-dense, C-based fuels, the combination of SOFCs with onboard carbon capture is appealing for the decarbonization of difficult-to-abate vehicles. The primary advantage of the combination is the ability to serve large amounts of energy dense fuels with a relatively small electrochemical conversion device, therefore the best fit is for extremely

large classes of vehicles like maritime merchant ships which require extreme amounts of onboard energy.

Acknowledgment

I would like to thank with all my heart my friends, family, colleagues, and mentors who have had my back as I chose the path of earning a PhD, and in her own special category, Marysol Encarnación, who agreed to be my fiancée sometime near the end of this journey. I am also grateful to the American taxpayers for their funding of the Department of Energy and National Science Foundation which in turn funded this work.

I've had a great time. Despite lessons learned the hard way, the all-nighters in lab, and the sometimes-lackadaisical responses to conference presentations and papers, it was all worth it. And that's because of a confluence of factors: Prof. Scott Barnett has created an incredibly supportive and good-natured research group, and together we're guided by purpose and meaning as we develop a technology with a real path to serving future civilization with sustainable energy. What an absolute privilege it is to work in a group like this.

Under the unparalleled guidance and support of Scott Barnett, I never felt dismay for long if results were going pear-shaped. And I'm proud of the results borne of that process! Even during the novel coronavirus pandemic of 2020-2022 (reader, let's hope), Scott and the group kept our cool and focused on the science we all love. Our group is one of a kind. Thank you to my graduate student mentors Justin Railsback and Matthew Lu who showed me very early on how fun it was to work with our systems. Thank you to the wonderful post-docs Roberto Scipioni, Tianrang (Tim) Yang, Beom-Kyeong (Big King) Park, Junsung Hong, Yubo Zhang, Colin Campbell, and Elahe Moazzen from whom I learned so much. Thank you to the visiting scholars Shanlin Zhang, Julian Ascolani-Yael, and Alessandro Donazzi with whom I had such immense pleasure to work. Thanks to the other Barnett group members of yesteryear: Nick Geisendorfer, Qinyuan Liu, Xiankai Yu, and Hongqian (Sharon) Wang. And thanks to the current graduate students: Jakob Reinke, Dalton

Cox, and Jerren Grimes. Very special thanks to those who had to deal with me through my managerial capacity, my mentees Hao Chen, John (Jack) Pieterse, and again, Jakob Reinke.

Outside of our group, thank you to my committee members who have agreed to keep this work in check, Professors Sossina Haile and Peter Voorhees, and Doctor Neil Schweitzer. Prof. Haile taught me wonderful principles of solid state ionics, and I truly believe TAing for her class was a golden opportunity, allowing me to immerse myself in the fundamentals. The kinetics and phase transformations I learned in Prof. Voorhees's class were instrumental in my understanding of the systems to follow in this dissertation. And I'd like to thank my out-of-department choice, Dr. Schweitzer, for helping me with ALD, BET, and through my collaborator Alessandro, some heterogenous catalysis. And thank you to our collaborator Dr. Liliana Mogni and Dr. Mariano Santaya who hosted me in their lab in San Carlos de Bariloche, Argentina in 2019 and facilitated an unforgettable month of adventure. And thanks also to my current roommate and Haile group member, Louis Wang, who so fortuitously dropped into my living situation, leading to so many-invaluable late-night discussions about fuel cell technology and experimental methods. It never felt like overworking because with you it was so fun to talk about this stuff!

I also want to thank the members of the Northwestern Climate Technology Club (formerly, Northwestern Energy Technology Group) for being the best group of young scholars to collectively wrap our heads around the hyper-object that is the climate crisis.

And thanks also to my friends of no research-relation, but ones I've still made out here at Northwestern: Kelly, Kerim, Abhi, Mark, Yeonjun, Arya, and Ben.

Finally, thank you to my parents Gregory and Karen, my sister Stephanie, and all my lovely family, including those who have moved on. You all helped raise me, so this dissertation is indebted to you.

List of Abbreviations

ALD	Atomic Layer Deposition
BET	Brunauer-Emmett-Teller
BEV	Battery Electric Vehicle
CCFCV	Carbon Capture Fuel Cell Vehicle
CTE	Coefficient of Thermal Expansion
DRT	Distribution of Relaxation Times
ECM	Equivalent Circuit Modeling
EDS/EDX	Energy Dispersive X-ray Spectroscopy
EIS	Electrochemical Impedance Spectroscopy
FIB-SEM	Focused Ion beam Scanning Electron Microscopy
GDC/CGO	Gadolinia-Doped Ceria (e.g., $Gd_{0.1}Ce_{0.9}O_{1.5}$)
H2FCV	Hydrogen Fuel Cell Vehicle
HER	Hydrogen Evolution Reaction
HOR	Hydrogen Oxidation Reaction
ICEV	Internal Combustion Engine Vehicle
ICP-OES	Inductively-Coupled Plasma Optical Emission Spectroscopy
LIB	Lithium-Ion Battery
LSCF	Strontium and Cobalt-doped Lanthanum Ferrite (e.g., $La_{0.6}Sr_{0.4}Co_{0.2}Fe_{0.8}O_{3-\delta}$)
LSM	Strontium-doped Lanthanum Manganite (i.e. $(La_{0.8}Sr_{0.2})_{0.98}MnO_{3-\delta}$)
MIEC	Mixed Ionic Electronic Conductor
OCV	Open-Circuit Voltage
OER	Oxygen Evolution Reaction

ORR	Oxygen Reduction Reaction
PPD	Peak Power Density
R-P	Ruddlesden-Popper (phase)
ScSZ	Scandia-stabilized Zirconia (e.g., ZrO_2 with 10 mol% Sc_2O_3)
SDC	Samaria-doped Ceria (e.g., $Sm_{0.2}Ce_{0.8}O_{2-\delta}$)
SEM	Scanning Electron Microscopy
SOC	Solid Oxide Cell
SOEC	Solid Oxide Electrolysis Cell
SOFC	Solid Oxide Fuel Cell
SSC	Strontium Samarium Cobalt Oxide (e.g., $Sr_{0.5}Sm_{0.5}CoO_{3-\delta}$)
STEM	Scanning Transmission Electron Microscopy
STF	Iron-doped Strontium Titanate (e.g., $SrTi_{0.3}Fe_{0.7}O_{3-\delta}$)
STFN	Nickel and Iron-doped Strontium Titanate (e.g., $SrTi_{0.3}Fe_{0.63}Ni_{0.07}O_{3-\delta}$)
STFR	Ruthenium and Iron-doped Strontium Titanate (e.g., $SrTi_{0.3}Fe_{0.7}Ru_{0.07}O_{3-\delta}$)
TDMAZ	Tetrakis(dimethylamido)Zirconium(IV) (i.e., $Zr(NMe_2)_4$)
TEM	Transmission Electron Microscopy
TG	Thermogravimetric analysis
TMA	Trimethylaluminum
TPB	Triple Phase Boundary or Three Phase Boundary
XRD	X-Ray Diffraction
YSZ	Yttria-Stabilized Zirconia (e.g., ZrO_2 with 8 mol% Y_2O_3)

Table of Contents

Abstract 3
Acknowledgment 6
List of Abbreviations 8
Table of Contents 10
List of Illustrations, Figures, and Graphs 13
List of Tables 18
1 Introduction 19
2 Background 24
2.1 The Solid Oxide Electrochemical Cell 24
2.2 Electrochemical devices and testing 29
2.3 Oxygen Electrode Materials 31
2.4 Fuel Electrode Materials 32
2.4.1 Cermet anodes 32
2.4.2 Perovskite anodes 33
2.4.3 Exsolved Anodes 33
2.5 Degradation Phenomena in SOFC Electrodes 35
2.5.1 Coarsening 35
2.5.2 Cation surface segregation (Oxygen Electrode) 36
2.5.3 Chromium Poisoning (Oxygen Electrode) 37
2.5.4 Coking (Fuel Electrode) 37
2.5.5 Sulfur Poisoning (Fuel Electrode) 38
2.5.6 Redox Cycling (Fuel Electrode) 38
2.6 Electrolytes and cell architecture 39
2.7 Atomic Layer Deposition 40
3 Methods 43
3.1 Cell Preparation 43
3.1.1 SSC-GDC and LSCF Oxygen Electrodes 43
3.1.2 SSC powder characterization 44
3.1.3 STF(N) Symmetric Fuel Electrode Synthesis 44
3.1.4 Ni/YSZ synthesis 45
3.2 Atomic Layer Deposition 45
3.2.1 ZrO_2 atomic layer deposition 45
3.2.2 Al_2O_3 Atomic Layer Deposition 46
3.3 Electrochemical characterization 46
3.3.1 SSC-GDC and LSCF Testing 46
3.3.2 Hydrogen and Redox Testing 47
3.3.3 Accelerated Coke Testing 48
3.4 X-ray characterization 49

3.5 Electron Microscopy 49
3.5.1 Scanning 49
3.5.2 Scanning transmission 50
3.6 ICP-OES 50
3.7 BET Surface Area Measurement 50
4 Atomic Layer Deposition of Zirconia for Coarsening Inhibition of Infiltrated Solid Oxide Oxygen Electrodes 52
4.1 Abstract 52
4.2 Introduction 53
4.3 Results 55
4.3.1 Electrochemical characterization 55
4.3.2 ALD zirconia layer characterization 58
4.3.3 SSC-ZrO_2 stability 65
4.4 Discussion 69
4.5 Conclusions 72
5 Atomic Layer Deposition of Alumina for Surface Area Determination of Solid Oxide Electrodes 74
5.1 Abstract 74
5.2 Introduction 75
5.3 Description of the Methodology 78
5.4 Validation 80
5.5 Vignettes demonstrating usage 85
5.5.1 Coarsening of PrO_x Infiltrations 85
5.5.2 Exsolution of Metal Particle Decorations 87
5.6 Conclusions 88
6 In-situ Exsolution and Redox Reactivation of Ni- and Ru-based Metal Alloys from Strontium Iron Titanate Perovskite Solid Oxide Fuel Electrodes 89
6.1 Abstract 89
6.2 Introduction 90
6.3 Results and Discussion 92
6.3.1 Electrochemical Measurement 93
6.4 STFN Performance as an Oxygen Electrode 102
6.5 X-ray Diffraction 103
6.6 Electron Microscopy 113
6.7 Conclusion 117
6.8 Addendum: STFR and Ni/YSZ operated in ethanol with redox cycling 119
7 Viability of Vehicles with Solid Oxide Fuel Cells and Onboard Carbon Capture 124
7.1 Abstract 124
7.2 Introduction 124

7.3 C-Based Fuel and CO_2 Storage Requirements 128
7.4 Technology Comparisons across Vehicle Classes 131
7.5 Infrastructure, Phased Adoption, and CO_2 Footprint 135
7.6 Technological Challenges 137
7.6.1 Dual-chamber, pressurized tank 138
7.6.2 CO_2 compressor 138
7.6.3 Thermal integration 138
7.6.4 SOFC development and manufacturing 139
7.6.5 Matching duty cycles 140
7.6.6 Fuel and exhaust composition 141
7.7 Summary and Future Outlook 141
References 144
Vita 153

List of Illustrations, Figures, and Graphs

Figure 2.1 A schematic representation of a solid oxide fuel cell (SOFC) and solid oxide electrolysis cell (SOEC). 25
Figure 2.2 Fuel cell operation voltage with associated losses. Sourced by permission from Lu et al.[10] 26
Figure 2.3 Example experimental results in which cell power, represented on the opposite y-axis, hits a maximum and decreases. Unpublished cell data courtesy Dr. Yubo Zhang. 27
Figure 2.4 A typical impedance plot with equivalent circuit modeling. 30
Figure 2.5 The active sites of two classes of electrode based on the forms of their conduction. Figure adapted from Lu et al. with permission.[10] 31
Figure 2.6 The "ALD Window" in which precursors result in conformal, uniform coverage of complex substrates. Temperatures that are too high or too low can result in abnormally high or low growth-per-cycle.[53] 41
Figure 3.1 Redox cycle with a temperature excursion to 850°C during oxidation. 47
Figure 3.2 A bubbler system that allows a user to switch from hydrogen in water to hydrogen in ethanol without interruption of an electrochemical experiment. 48
Figure 4.1 Bode and Nyquist plots of EIS spectra from 0, 30, and 60 cycles ALD-ZrO_2-coated SSC–GDC cells, taken at 600°C (a) shortly after the initial heating of the cell to 600°C, (b) after approximately 48 hours of ageing at 750°C, and (c) after approximately 1000 hours of ageing at 750°C. Data is fit with an equivalent circuit model consisting of an inductor, resistor, high frequency RQ element, and low frequency Gerischer element in series.[18] 56
Figure 4.2 Time dependence of the polarization resistance measured in air at 600°C for cells with 0, 30, and 60 cycle ALD-ZrO_2 coated SSC–GDC electrodes. Cells were maintained at an accelerated ageing temperature of 750°C except during periodic interruptions for EIS measurements. 57
Figure 4.3 Life-test trials for three cells produced and tested with the same conditions as in the main body text, except with 800°C ageing temperatures and thicker ~35 um SSC-GDC and ~20 um LSM electrodes. Data duplicated with permission from the thesis of Kevin Zhao, Northwestern University.[82] 57
Figure 4.4 Time dependence of the polarization resistance for LSCF electrodes measured in air at 750°C for cells with 0, 1, 10, and 100 cycles of ALD-ZrO_2. 58
Figure 4.5 STEM images of SSC powders, with (a) 0, (b) 3, (c) 30, and (d) 60 cycles of ALD-ZrO_2 with superimposed measurements of representative coating thicknesses. Sub-monolayer growth is visible in (b) transitioning to a layer-by-layer growth-per-cycle at higher cycle numbers. 60
Figure 4.6 (a) EDS line-scans of an SSC–GDC cathode coated with 300 cycles of ALD-ZrO_2. The Zr Kα signal is significant near the surface, within the microstructurally less complex LSM current collector, and rapidly diminishes over a ~20 μm depth as LSM transitions into the narrower pores of SSC–GDC. (b) An SEM micrograph of the three-layer region from which the

line-scans in (a) were collected. (c) A comparison of the Zr Kα peaks taken in the near-surface (LSM) region and within the active region of the tested electrode (labeled “2” and “1” in (b), respectively). 62
Figure 4.7 Zr counts (teal line) into an LSM-current collector then SSC-GDC system with 5 s precursor exposure times with no noticeable improvement rendered, 240°C deposition..... 63
Figure 4.8 Zr counts (teal line) into an LSM-current collector then SSC-GDC system with 5 s precursor exposure time at 120°C deposition temperature. 64
Figure 4.9 SEM and EDS line-scan for an LSCF electrode with 50 cycles of deposition and 5 s pulse lengths, showing a conformal coating achieved. 64
Figure 4.10 Water-soluble surface strontium in SSC powder annealed for varying times at 750°C. The ionic amount of Sr is normalized by the mass of SSC used for measurement. At annealing times 10 hours and beyond, the Sr concentration does not evolve over time, indicating a relative robustness of SSC against cation surface migration. 66
Figure 4.11 XRD spectra of (a) pristine SSC powder with an SrCO3 impurity, (b) SSC powder with ALD-ZrO_2 and without annealing, (c) ALD-ZrO_2-coated SSC after 10 hours of annealing at 750°C. Reference phase data and PDF card numbers are included in the 6 bottom panels for comparison, with zirconia being represented by the maximum intensity peaks from five major crystal systems. 67
Figure 4.12 XRD result of SSC powder with ALD-ZrO_2 annealed at 800°C for 10 hours. The largest peak for SSC, ~33°, recedes into a small shoulder on a larger Sm-zirconate peak, while the other peaks of SSC greatly diminish in favor of Sr- and Sm-zirconates and Co_3O4. Evidence of crystalline zirconia phases is not found. The unbalanced reaction chemistry is: $ZrO_2 + Sr_{0.5}Sm_{0.5}CoO_3 \rightarrow SrZrO_3 + Sm_{1.22}Zr_{2.78}O_{7.39} + Co_3O_4$. The PDF card number for the Sm-zirconate is 04-021-6444; the other phases are included in main text Figure 4.11. 68
Figure 4.13 XRD peak-shape comparison from broad (pristine sample) to narrow (annealed samples) with the sample having undergone ALD treatment narrowing less than the sample without, implying a smaller average crystallite size. PDF card numbers are included. 69
Figure 5.1 Process overview for the surface area determination technique using ALD and ICP-OES. 79
Figure 5.2 Tracking the signal of Al diffused into porous electrode scaffolds by SEM/EDS line-scan, with the top depicting an infiltrated oxygen electrode, PrOx-LSM/GDC, and the bottom a Ni/YSZ support. Fracture cross-sections are also shown. 81
Figure 5.3 Micrograph of self-supported bulk LSM/GDC fired to create quantities large enough for BET measurement (~1 g material per measurement). The microstructure is equivalent so electrodes fired atop GDC substrates..... 83
Figure 5.4 Comparison between methodologies of surface area determination, two using the ALD method (one deriving Al_2O_3 volume by ICP-OES, the other by its mass) and the last using BET theory. Also shown is the signal and error from ICP-OES on samples that were not coated with ALD-Al_2O_3. 84

Figure 5.5 Comparison between the (a) as-fired LSM/GDC, (b) PrO_x-infiltrated LSM/GDC after 16 h at 700°C, and (c) PrO_x-infiltrated LSM/GDC after 1040 h at 700°C. Morphological differences are subtle and would be difficult to identify by sight..... 86
Figure 5.6 Increase in surface area relative to bare LSM-GDC as measured by the ALD surface area technique. Two samples with low ageing show a wide disparity in PrO_x loading which is linearly related to the surface area increase. After 1 kh, the surface area increase has been highly reduced by coarsening and possibly Pr-dissolution into GDC. 86
Figure 5.7 SEM-acquired microstructures of (a) STF and (b) reduced STF, (c) $S_{1.00}$TFN and (d) reduced $S_{1.00}$TFN, and (e) $S_{0.95}$TFN and (f) reduced $S_{0.95}$TFN. All scale bars 500 nm. 87
Figure 5.8 ALD-derived surface areas for STF, stoichiometric $S_{1.00}$TFN, and A-site deficient STFN ($S_{0.95}$TFN)..... 88
Figure 6.1 Total polarization resistance of STF, stoichiometric STFN, and A-site deficient STFN in H_2 (3% H_2O) at 700°C, with elevated temperature oxidation every 250 hours at 850°C. 93
Figure 6.2 Nyquist and bode plots of initial, 250 h, and reset electrochemical performance for STF, stoichiometric STFN, and A-site deficient STFN. The data is modeling with an inductor, resistor, and two RQ elements at ~0.5 Hz and 50 Hz. 96
Figure 6.3 Polarization broken into ohmic resistance, the first high frequency RQ element associated with charge transfer (R_{CT}), and the second low frequency RQ element associated with adsorption/dissociation (R_{AD}) for STF, stoichiometric STFN, and A-site deficient STFN..... 97
Figure 6.4 The behavior of STF in its first 250 hour reduction. The behavior, associated with H_2 adsorption/dissociation, suggests that the exsolved Fe catalyst phase nucleates after 24 h. 99
Figure 6.5 Distribution of Relaxation Time (DRT) analysis of the 5-times redox life-test of STF, stoichiometric STFN ($S_{1.00}$TFN), and A-site deficient STFN ($S_{0.95}$TFN). Panels (a)-(c) depict the impedance of the first 250 hours of ageing, (d)-(f) the impedance at each reset point before ageing, and (g)-(i) the impedance after 250 hours of ageing of each reset cycle. 101
Figure 6.6 Performance of STFN in air initially and after one and two redox cycles. 103
Figure 6.7 Early attempts to measure the reduced state of STFN yielded hydrated phases only stable at low temperatures as a result of ex-situ sample preparation. Here stoichiometric STFN was reduced in 30% H_2 at 850°C, driving more extreme exsolution and phase transformation than the main 700°C condition of the study. 104
Figure 6.8 Ex-situ and in-situ XRD demonstrate that the cooling procedure used to test ex-situ results in the loss of the Ruddlesden-Popper phase due to low temperature instability of either Fe metal or the R-P phase itself, for (a) stoichiometric $S_{1.00}$TFN and (b) A-site deficient $S_{0.95}$TFN. 105
Figure 6.9 Initial structure of STF, stoichiometric $S_{1.00}$TFN, and A-site deficient $S_{0.95}$TFN in air at 700°C. The $S_{0.95}$TFN sample includes a proportion of excess bulk NiO after synthesis..... 106
Figure 6.10 X-ray diffraction data for STF, stoichiometric $S_{1.00}$TFN, and A-site deficient $S_{0.95}$TFN after reduction. (a) In-situ data after 4 h in 97% H_2 + 3% H_2O. (b) Ex-situ data after 24 h in 97% H_2 + 3% H_2O. 107

Figure 6.11 Rietveld refinement for $S_{0.95}$TFN after 4 h exposure to 97% H_2 (3% H_2O), in-situ at 700°C. 108
Figure 6.12 Vegard's law applied to 24 (Ni,Fe) alloy compositions and 54 for pure Ni. Data from the PDF4+ crystallographic database.[130] 109
Figure 6.13 In-situ XRD during the reduction process for (a) stoichiometric $S_{1.00}$TFN and (b) A-site deficient $S_{0.95}$TFN 111
Figure 6.14 Re-oxidation behavior in-situ showing, from bottom to top, the initial oxidized state, the reduced state (4 h), the oxide formation upon re-oxidizing for 1 h at 700°C, and after 1 additional h at 850°C. All spectra recorded at 700°C for (a) stoichiometric $S_{1.00}$TFN and (b) A-site deficient $S_{0.95}$TFN 112
Figure 6.15 Scanning electron microscopy for over various stages of reduction and oxidation for (a) STF, (b) stoichiometric $S_{1.00}$TFN, and (c) A-site deficient $S_{0.95}$TFN 114
Figure 6.16 (a) Secondary electron STEM of the 1 kh redox-cycled S1.00TFN sample, (b) high angle annular dark-field, and (c) EDS elemental maps (note the reduced scale-bar, each element is tiled to be seen separately.) 116
Figure 6.17 Impedance results of an accelerated coking experiment in which STFR and Ni/YSZ are subjected to hydrogen bubbled first through water, and then through anhydrous ethanol. .. 120
Figure 6.18 Post-mortem of (a) STFR and (b) Ni/YSZ after ramping down in a hydrogen 6% ethanol environment 121
Figure 6.19 Carbon formation on the free surface of the post-mortem STFR cell. Image formed by two images of different focus to highlight in-plane both the cell and coke. 123
Figure 7.1 Schematic illustration of a Carbon Capture Fuel Cell Vehicle (CCFCV) and associated infrastructure. The vehicle includes a solid oxide fuel cell (SOFC) for efficient electrical generation from hydrocarbon or alcohol fuels. Fueling is with any of biofuels, fossil fuels, or electrolytic fuels produced using renewable electricity. The captured CO_2 can be stored in a separate tank or in a unified tank with a movable partition, as shown, to minimize net storage volume. After offloading, the CO2 can either be used in electrolytic fuel production or sequestered. Different infrastructure designs and fuel choices can yield an overall CO2 impact ranging from mitigatory to net negative. 126
Figure 7.2 (a) Density of CO_2 versus pressure, at and below its critical temperature (T_C). A similar density is achieved past its critical pressure (P_C). H_2 is also shown for comparison, highlighting the relative ease of compressing CO_2. Comparison of the volumes (b) and masses (c) of different fuels corresponding to 1 GJ (lower heating value) of stored energy, and of the CO_2 produced by oxidation of the fuels. [Note: GJ is used as a convenient measure; 1 GJ corresponds to the energy in 31 L of gasoline, approximately the size of a small automobile's fuel tank.] Values are given for tank pressures of either 250 or 700 bar at 31.1 °C. Also shown are values for hydrogen and a representative Li-ion battery 129
Figure 7.3 Volume (bars outlined in blue) and weight (bars outlined in red) of the vehicle power system for ICEVs, BEVs, H2FCVs, and CCFCVs with ethanol and 250 bar storage. (a) shows

the case of a medium-sized tanker ship (e.g., Wärtsilä WSD42 111K). (b) shows a light-duty sedan of ~500 km range (e.g., Toyota Mirai and Tesla Model S); For (a), the stored energy is by far the predominant portion of total power system weight and volume. 132
Figure 7.4 Schematic diagram of the proposed carbon capture fuel cell vehicle (CCFCV) energy conversion system. In this depiction, the SOFC is integrated with a LIB, as would be particularly advantageous for managing the variable load of smaller vehicle classes – this approach has been proposed both with low-temperature fuel cells[168-173] and SOFCs,[166, 174, 175] and provides several advantages. In the hybrid system, the SOFC provides a fairly steady power output at the average value required by the vehicle, effectively range-extending the battery. A battery pack that is small by BEV standards then provides the relatively high power required for acceleration (and for terrestrial vehicles, rapid charging during regenerative braking). In larger and steadier-power vehicles, the relative size of the LIB in the power system can be decreased or eliminated completely so long as initial SOFC startup is externally powered (e.g., via the grid). 137

List of Tables

Table 6.1 Degradation rates for STF and STFN life-tests broken into two steady-state segments, the degradation within one reduction period (after 150 h) and the degradation between redox-reset periods (starting with the first reset at t=250 h) 95
Table 6.2 Percent increases in R_{AD} throughout the experiment and after redox cycling. 99
Table 7.1 Input parameters for Figure 7.2(b), a volumetric comparison between various hydrocarbon and alcohol fuels, as well as a representative Li-ion battery and hydrogen, at 31.1°C. (Note that for the most volume-sensitive applications, tank volume can be further decreased by employing a mixture of fuels that balance to be 1:1 volumetrically with their product CO_2. For example, at 250 bar, a mixture of 51% methane to 49% propane results in 65.0 l/GJ, versus the best single fuel, propane at 70.4 l/GJ. At 700 bar, 55%/45% methane/propane results in 55.6 l/GJ versus propane at 60.6 l/GJ. It may be beneficial to add a percentage of water to the higher C-number fuels in order to run on-board partial steam reformation. To this end, the fact that most of these fuels have volumes lower than their resulting CO_2 allows for penalty-free inclusion of a few percent H_2O content. One could also tailor a mixture if considering a specific utilization efficiency, as mentioned in the previous section. 131
Table 7.2 Input parameters for Figure 7.2(c), a gravimetric comparison between various hydrocarbon and alcohol fuels, as well as for a representative Li-ion battery and hydrogen..... 131
Table 7.3 Input parameters for volumetric and gravimetric calculations of four simplified power systems in an Aframax-class tanker ship, shown in Figure 3a, based on the Wärtsilä WSD 42 111K.[151] Heavy fuel oil is used as the fuel for the ICEV. The H2FCV is taken to run on 700 bar hydrogen, and the CCFCV on 250 bar ethanol. For the fuel cell vehicles, fuel cell and drive unit volume and weight are taken as the automotive examples in subsequent Table 7.4 scaled by the increased power of the ship. Unlike for the sedan, weight and volume of a supplementary battery to the fuel cell systems are not considered here given the more constant duty cycle of a tanker, i.e., in the absence of instantaneous changes in power like for regenerative braking. 134
Table 7.4 Input parameters for volumetric and gravimetric calculations of four simplified power systems in a four-door sedan, shown in Figure 3b. The miles-per-gallon-equivalent (MPGe) of the CCFCV is estimated as the 2020 Toyota Mirai H2FCV MPGe multiplied by a factor representing the increase in fuel-to-electrical energy efficiency of SOFCs/PEMFCs (60%/50%).[154] For the CCFCV, the fuel cell maximum power output is taken to be 25 kW as needed for highway driving, whereas the hybrid battery pack is taken to be 15 kWh, sufficient to provide an ~60 km electric-only range. The packaged BEV battery (i.e., including active and inactive material) is taken to be 100 kWh (e.g., 2019 Tesla Model S P100D). Batteries for the H2FCV and CCFCV borrow the energy density and specific energy of the packaged Tesla battery for ease of comparison (despite, for example, that year's model of the Mirai using a nickel-metal hydride battery). The H2FCV is taken to run on 700 bar hydrogen, and the CCFCV on 250 bar ethanol (the tank volume and weight set by the product CO_2). 135

1 Introduction

The great project for this generation is averting climate catastrophe. Climate change, or by its name of greater expediency, the climate crisis, if left unchecked, will lead to billions of lives affected for the worse or ended by its force to create deadly heat waves, exacerbate ocean storms, intensify fires, and disrupt ecologies.[1] The "discount rate," which states a dollar today is worth more than a dollar tomorrow, is one of the tenets of our global economics; future human life, however, cannot be discounted.[2] A living person in 2100 is worth just as much as one now. Therefore, the only humane response in light of our understanding of the causes of climate change is to cease and desist our CO_2 emissions, even at high cost, to stop their compounded impact on all future generations.

Much of this effort will be sociopolitical, and much will be technical; this dissertation is necessarily concerned with the latter. The 21st century way of life in developed nations is enabled by cheap and abundant energy; as more countries further their development, they too will expect a greater per capita energy intensity for their citizens. In the US, our 2020 primary energy mix was 82% fossil carbon-based; in India it was 90%.[3] Where renewables are online, they are used almost exclusively for grid electricity; even harder to decarbonize are the cement and steel used in building out infrastructure, the process heat to power manufacturing, and the energy intensive fuels needed to run global commerce and fly us through the air to conduct our expansive lives.[4, 5] Society has relied on the crutch of fossil fuels with unpriced externalities, a loan taken against future welfare. Short-term, these fuels are tremendous caches of seemingly "free" energy for the taking; long-term, they are precursors to a polar gas with a resonance able to send the Earth's reflected thermal energy back down towards it.

The electrochemical devices studied in this dissertation may be related to the abatement of a large percentage of global CO_2 emissions. They are not primary sources of power; this will be the domain of wind, solar, geothermal, tidal, and other planetary-scale energetic processes. Instead, they are energy storage and conversion devices, useful in making the electrons from renewables better adapted to our sometimes-difficult use cases, such as our need for 24/7 grid uptime in the dark dead of winter, or power on the rolling high seas.

That technology under study is the solid oxide electrochemical cell. Its useful principle is that it requires reactions to be electrochemical ones, in which charge carriers are forced to travel non-negligible distances to reorganize into lower energy forms. With this decoupling, we can use electricity as a product or a reactant. In its electricity-generating form, the device is known as a solid oxide fuel cell (SOFC). In its electricity-consuming and fuel generating form, it is a solid oxide electrolysis cell (SOEC). An analog to the SOFC is an internal combustion engine; a fuel is provided, and the SOFC/engine converts the fuel's free energy into useful work (that work is electrical for the SOFC, mechanical for the engine). But because the reactions in the case of thermochemistry are irreversible, there is no "engine" analog for the SOEC. One cannot turn the engine with a lever and create gasoline. But, due to the reversibility of electrochemical reactions, we can do just that to make hydrogen from water, or more complex hydrocarbons by the addition of CO_2.

This dissertation is motivated by the decarbonization of two major sectors, grid electricity (25%), and energy-intensive transportation (6%).[4, 6] It may be connected to the decarbonization of many other sectors by way of hydrogen generation—industrial heat may use it for combustion, mining for thermochemical reduction of ore, and aviation via the production of energy-dense synthetic fuels. Grid electricity, the major slice of the pie, is in dire need of economic forms of

energy storage. The longer the duration of our energy storage technologies, the deeper we can allow inherently intermittent renewables to penetrate the energy mix. The well-matured Li-ion battery is approaching its cost floor, and is suitable for some 4 hours of grid-level discharge.[7] Other, bulkier energy storage technologies like redox flow or iron-air batteries are being commercialized to address day- or days-long storage. All these batteries are limited in capacity to the redox potential of their reactant electrodes, effectively built into the devices. The fuel cell, however, is decoupled from its products and reactants, both being externally storable fluids, and can charge/discharge for indefinite durations, so even seasonal storage is possible, so long as fuel (SOFC) or electricity (SOEC) is provided. This decoupling is the primary functional difference between a fuel cell and a battery.

There are several varieties of fuel and electrolysis cell. Almost all of these operate at temperatures below that of the solid oxide fuel cell; however, it is the rather hot operating temperature of the solid oxide system that allows for cheaper, more abundant catalysts to be used for kick-starting the necessary electrochemical reactions. Iron, titanium, and cobalt rather than iridium and platinum, for example. Thermodynamically, the efficiency of the fuel cell is worse the higher the temperature, so an effort is underway to lower operating temperature, which additionally enables cheaper balance-of-stack components (e.g., interconnects and sealants) and slows certain degradation paths. However, efficiency losses in practice are thermally activated and the gap between theoretical efficiency and operating efficiency widens at lower temperature, ensuring the optimal temperature will continue to remain relatively high.[8] In electrolysis mode, higher temperature gives greater efficiencies, too. So, the study of SOFCs/SOECs will continue to be the domain of high temperature specialists, one in which atoms in the solid state are comparatively

more mobile: great for transport processes, but perhaps bad for keeping devices operating for many thousands of hours. There are “no moving parts” except for the atoms themselves.

High temperature operation also enables SOFCs to operate on other fuels with relative impunity (provided some degree of reforming), including ones of higher energy density than hydrogen, while still remaining carbon-neutral, such as electrolytic fuels (ammonia, methane) and biofuels (biomethane, bioethanol), enabling the SOFC to be potentially useful not just for stationary power but for transportation, too. The main commercial fuel for SOFCs currently in industrial use is methane by way of natural gas. As will be discussed in Chapter 7, carbon capture is particularly amenable with SOFCs given the exhaust stream is uncontaminated by ambient air. While fossil methane may still be carbon-neutralized via carbon capture, the world still demands sustainable energy storage, and SOFCs and SOECs are well-positioned to provide just that.

The promise of the SOFC is related to its efficiency when operating with relatively abundant materials, and its projected economic cost is correlated to such efficiency. The total cost of ownership is a term that reflects both the capital expense and operating expense over the lifetime of an asset. For SOFCs, the simplest way to reduce the annualized total cost of ownership is to increase the lifetime of the stack. The US Department of Energy is targeting a degradation rate of SOFC performance of 0.2%/1,000 h, which amounts to a 5-year stack lifetime, about the same as a jet engine.[9] However, for stationary assets, this is still quite short-lived. For this reason, studying and combatting degradative processes in next-generation solid oxide materials is the major research aim of this dissertation. Other ways to address cost are employing even less expensive catalysts, developing advanced manufacturing methods with high yields and material utilization, and simply allowing economies of scale to develop.

Next-generation materials are often reported with impressive 0-hour performance and are often only stability-tested for a matter of hours to days. One of the unique specialties of the Barnett group is intensive materials studies of long-term degradation processes, with studies regularly including >1 kh tests, sometimes under accelerated aging conditions to simulate an entire 40,000 h lifetime. Accelerated ageing is critical in studying materials meant to perform for years, but it is difficult in practice, because speeding up kinetics often also means shifting thermodynamics, so analysis needs to be careful, with these studies paired with advanced characterization to elucidate real in-operando degradation mechanisms. With that understanding, electrode materials can be iterated or techniques to stave off degradation employed. It is through this process that the mutually inclusive science and engineering of the field of Materials Science and Engineering is put to use in creating advanced energy devices.

Chapter 2 will break down the necessary background information pertaining to solid oxide cell operating principles, materials structure-property relationships, and degradation processes. Chapter 3 will present a collection of experimental methods carried out to fabricate, test, and characterize solid oxide samples. Study results will lead off with Chapter 4 as degradation abatement in the oxygen electrode through atomic layer deposition is considered. Atomic layer deposition will be further explored in Chapter 5 as a means to characterize the surface area of either oxygen or fuel electrode. In Chapter 6, focus switches to the fuel electrode, exploring the concept of exsolved, socketed metal catalyst particles. Finally, Chapter 7 discusses solid oxide technology in context with carbon capture onboard heavy vehicles.

2 Background

The basic makeup of any electrochemical system is the inclusion of an anode (negative electrode—electrons flow away from it), electrolyte, and cathode (positive electrode—towards which electrons flow). All electrochemical systems deal with reduction and oxidation, with the charged ions needed to complete those reactions transported through the electrolyte, the electrons for charge balance in turn going through an external circuit (that circuit can be the electrical grid, for example). Two distinct forms of conduction are used: ionic and electronic, decoupled from each other, allowing electrical energy to be converted directly from chemical energy; fuel cells are a subclass of electrochemical device that oxidize a fuel to make this conversion. Solid oxide fuel cells (SOFCs) are a further subclass that specifically use a solid oxide electrolyte. Other fuel cell systems are defined by their respective electrolytes: proton exchange/polymer electrolyte membrane (PEM), protonic ceramic (PCFC), molten carbonate (MCFC), and solid acid (SAFC), to name others.

The examples below will focus on the hydrogen/water redox pair both for the simplicity it lends to the analysis, but also because hydrogen is the fuel on which the future of solid oxide cells as a green technology is largely staked. Also, most lab-based studies of solid oxide fuel electrodes focus on operation under hydrogen conditions, including all experiments in this dissertation, save for a brief experiment under mixed hydrogen/ethanol conditions.

2.1 The Solid Oxide Electrochemical Cell

Shown schematically below (Figure 2.1) are the two modes of operation for the solid oxide electrochemical cell. To run in the fuel cell regime, current is drawn from the energy of the formation of water. To run in the electrolysis regime, current is inputted to split water into fuel,

increasing chemical energy. Both modes are possible with the same exact device (although in practice, materials optimization would differ).

When the circuit in red in Figure 2.1 is closed but is maintained at zero voltage, such as what would happen when the atmosphere is the same on each side of the cell, the spontaneous water splitting and water forming reactions are still occurring at an equilibrium rate with no net current. When atmospheres of different effective pO_2 are on either side of the cell, but the connection in red is not closed, no current flows, but a voltage is still measurable, the open circuit voltage (OCV).

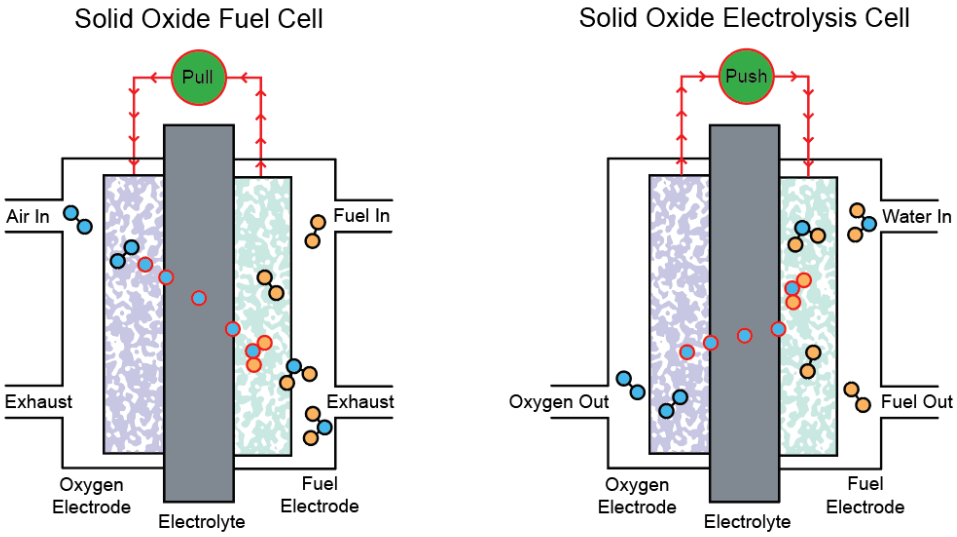

Figure 2.1 A schematic representation of a solid oxide fuel cell (SOFC) and solid oxide electrolysis cell (SOEC).

Below are the prototypical half-reactions found at each electrode for a hydrogen fuel source, the first being the Hydrogen Oxidation Reaction (HOR) (Equation 2.1) and the second the Oxygen Reduction Reaction (ORR) (Equation 2.2).

$$H_2 + O^{2-} \Leftrightarrow H_2O + 2e^- \qquad \textbf{(Equation 2.1)}$$

$$\frac{1}{2}O_2 + 2e^- \Leftrightarrow O^{2-} \qquad \textbf{(Equation 2.2)}$$

The ideal potential of a fuel cell with supplied chemical gradients is called the Nernst potential, shown below in (Equation **2.3**.

$$E = E^{\circ} - \frac{RT}{nF}\ln\frac{[p(H_2O)]}{[p(H_2)p(O_2)^{1/2}]} \qquad \textbf{(Equation 2.3)}$$

Here E, the reversible cell voltage, is determined by the constants E°, R, T, n, and F (respectively: the standard state voltage for the reactants, the gas constant, temperature, number of electrons involved in the reaction, and Faraday's constant) and the activities of the products and reactants, estimated here as partial pressures. The potential difference across the cell is related to the thermodynamic energy of formation of water, attenuated by the concentration of existing product and reactants.

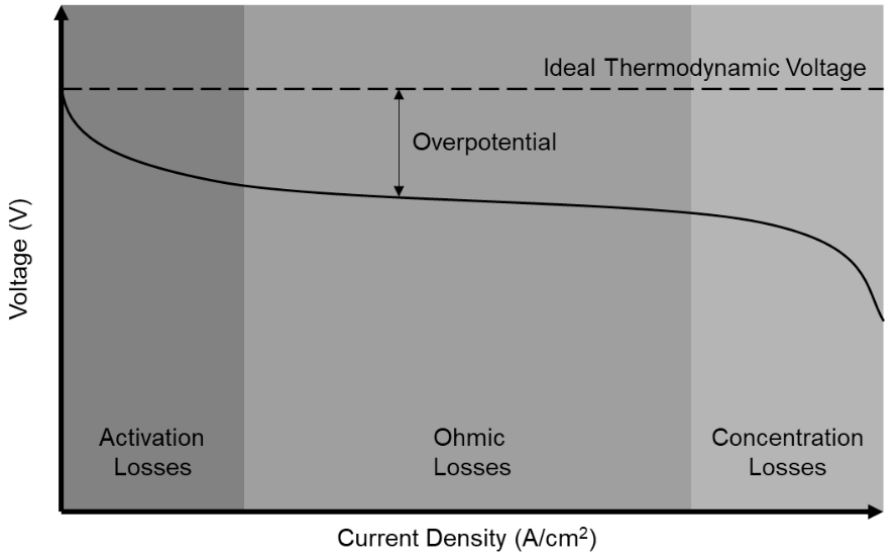

Figure 2.2 Fuel cell operation voltage with associated losses. Sourced by permission from Lu et al.[10]

However, due to kinetic losses during practical fuel cell operation—summarized in the figure above as slow reaction rates (activation losses), joule heating (ohmic losses), and hindered gas transport (concentration losses)—the obtained operation voltage will be lower than the ideal thermodynamic voltage, or Nernst potential, by the differences represented in (Equation **2.4**.

$$E_{operational} = E_{Nernst} - \eta_{activation} - \eta_{ohmic} - \eta_{transport} \quad \textbf{(Equation 2.4)}$$

The quintessential measure of a solid oxide fuel cell's performance is its peak power density (PPD), which is the product of current and voltage—as is apparent in Figure 2.2, as current density exceeds a certain middling amount, drawing more current may result in a decrease of power as overpotential increases (and energy is lost to heat). The voltage also drops as water is formed on the anode side, decreasing the ideal thermodynamic voltage. Typical experimental results are shown in Figure 2.3.

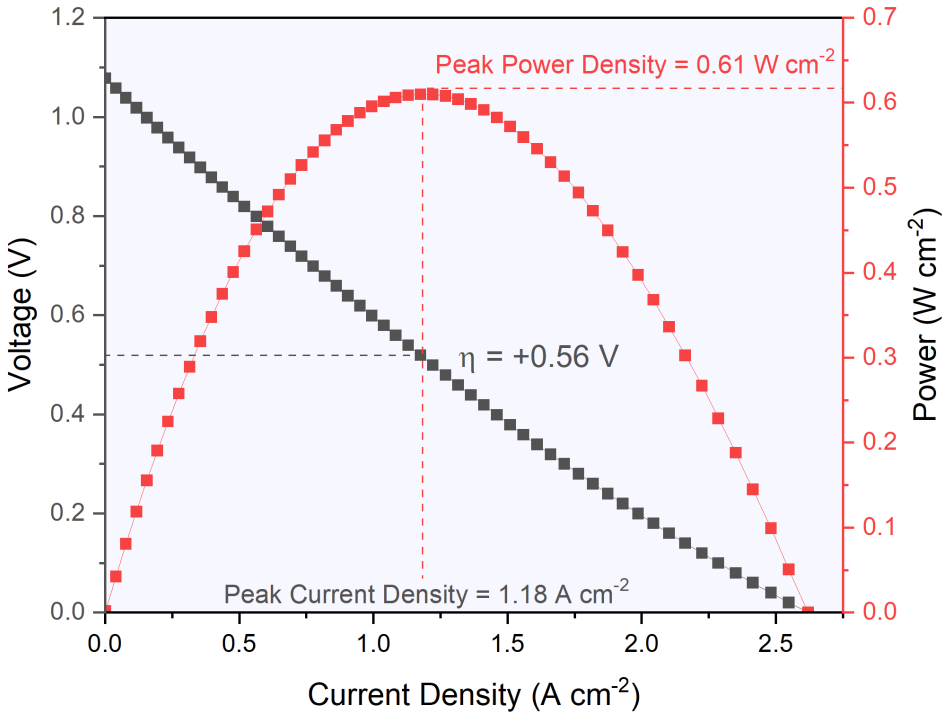

Figure 2.3 Example experimental results in which cell power, represented on the opposite y-axis, hits a maximum and decreases. Unpublished cell data courtesy Dr. Yubo Zhang.

Minimizing overpotentials (η) allows the peak current density to occur at greater power—the crux of SOFC development. The activation overpotential, η_{act}, is what this dissertation primarily seeks to lower, as it is the largest contribution to the resistance in practical applications. It can be approximated from the Butler-Volmer form of the overpotential equation at low currents as

$$\eta_{act} = \frac{2RT}{nF}\operatorname{asinh}\left(\frac{j}{2j_0}\right) \qquad \textbf{(Equation 2.5)}$$

which, when only a small range of current is examined with electrochemical impedance spectroscopy (EIS), can be approximated as a linear resistance called the cell's polarization resistance, R_p:

$$R_p = -\left[\frac{dV}{dj}\right]_{j\approx 0} \approx -\frac{RT}{nFj_0} \qquad \textbf{(Equation 2.6)}$$

where j_0 is the exchange current density, the rate of the forward and reverse reaction at equilibrium, which is a measure of catalytic performance. j_0, can further be described as the product of the exchange current for a smooth surface area, j_0' , and a roughness factor that is the true rough surface area, A, divided by the projected surface area, A', making

$$j_0 = j_0'\frac{A}{A'} = nFc_R^* f_1 \exp(-\Delta G/(RT)) \qquad \textbf{(Equation 2.7)}$$

where it is a function of the reactant concentration, c_R^*, the activation energy barrier, ΔG, temperatures, and the number of reaction sites, and the decay rate of the activated reactant species into products, f_1. The equation is written here this way to emphasize the different parameters that can be tuned to increase j_0, and thus the electrode and cell performance.[11]

The polarization resistance (as a function of time) is therefore the main quantitative metric by which electrode performance will be assessed throughout the dissertation.

2.2 Electrochemical devices and testing

As mentioned, a fuel cell comprises an anode, electrolyte, and cathode to complete the two electrochemical half-reactions involved in forming water. Laboratory testing of this "full cell" configuration offers the truest representation of real-world performance, because real-world SOFCs are full cells in series with each other to provide sufficient power. The downside of studying electrochemical processes in full cell devices is that it is difficult to identify the rate-limiting components of the devices—the frequency-dependent responses of the anode often overlap those of the cathode. Other electrochemical cells can utilize a reference electrode of known potential and place it such that polarization can be measured through one electrode. In solid oxide cells, thick electrolytes and extremely good alignment of the working and counter electrode are required for reliable decoupling.[12] Full cells also rely on good sealing to maintain internal reducing conditions, but often times pinholes develop and OCV will drop with increased pO_2 over time, adding an additional layer of obfuscation of the origin of degradation.

Therefore, a convenient way to study an electrode material is the symmetric cell configuration, which is structured as (electrode | electrolyte | electrode) and in which the cell is ensconced in a uniform gas environment, and OCV = 0. Alternating current electrochemical impedance spectroscopy (EIS) can then be used to study the forward and reverse reactions of oxygen reduction/evolution (ORR/OER), in the case of tests in air, or hydrogen oxidation/evolution (HOR/HER), in the case of tests in humidified hydrogen.

Deconvoluting EIS data is extremely important in identifying contributions to polarization resistance, when possible. Each step in an electrochemical process has a characteristic frequency, or time constant, under which it can sometimes be identified. Faster time constants correlate to generally faster, lower resistance processes. Some processes are easily identifiable by the shape of

the Bode plot, which plots imaginary impedance as a function of frequency, but others are overlapped and obfuscated, and may benefit from the use of Distribution of Relaxation Times (DRT) analysis, which uses Tikhonov regularization to frequency dependent impedance and converts it to time-dependent relaxation processes.[13]

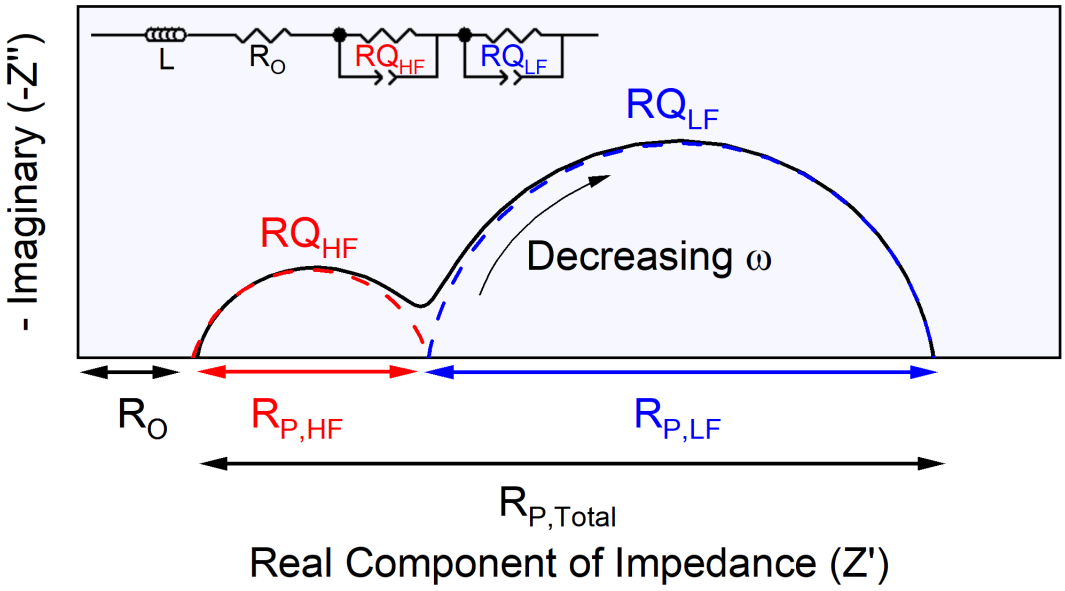

Figure 2.4 A typical impedance plot with equivalent circuit modeling.

Nyquist plots (Figure 2.4) show the complex impedance broken into its real (Z') and imaginary (Z'') components; at high frequency, the ohmic contribution to impedance (R_O) is entirely in the real domain, so contributions from electronic/ionic conduction can be easily measured. At lower frequency, complex impedances develop, which often take the shape of depressed semicircles, characteristic of resistances coupled with imperfect capacitance. They are often modeled as a resistor in parallel with a constant-phase-element, denoted Q, to form an RQ element. In the above figure, there are two processes, one at high frequency (RQ_{HF}) and one at low (RQ_{LF}). Each process has an associated resistance, and the resistances in sum form $R_{P,Total}$. Identifying, modeling, and fitting these elements are together referred to as Equivalent Circuit Modeling (ECM).[14]

2.3 Oxygen Electrode Materials

Historically, the largest polarization resistance in an SOC stemmed from the oxygen electrode, warranting an especially concerted effort in improving and sustaining its performance.[15] This is due to the high activation barrier of the ORR absent an effective catalyst, the reaction often described as "sluggish." (Recently, however, researchers argue that this is notion is becoming outdated and the fuel electrode is becoming the most resistive component.[16])

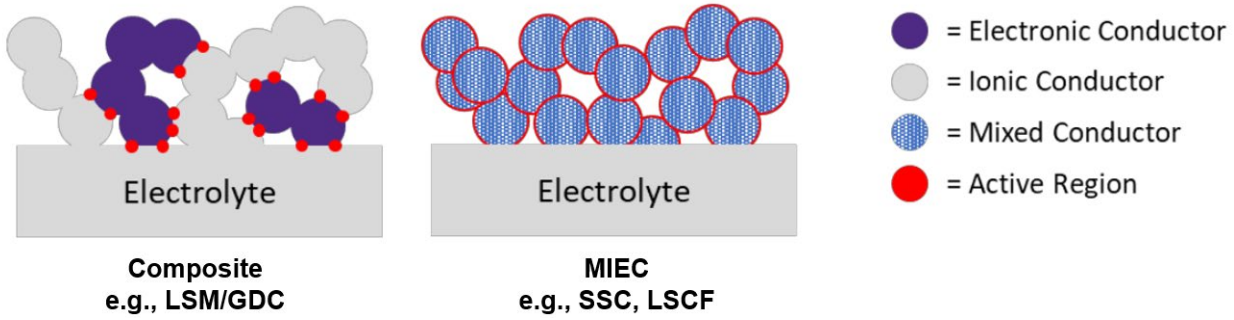

Figure 2.5 The active sites of two classes of electrode based on the forms of their conduction. Figure adapted from Lu et al. with permission.[10]

The highest performance oxygen electrodes incorporate mixed ionic/electronic conducting materials (MIECs), leading to the highest available surface area for the ORR, which requires both forms of conduction to proceed. The MIEC can be structured as a single phase, or it can be added atop a structure (itself ionically or of mixed conductivity) via wet impregnation, also known as infiltration. This technique flushes a solution containing the ions of the stoichiometric amount of, e.g., a perovskite, through a parent scaffold. Citric acid, a chelating agent, stabilizes and disperses the elements into a gel network at low temperature; this is known as the modified Pechini method.[17] Then, at high temperature (~850°C), the well-mixed elements of the gel form the desired oxide, at a temperature lower than via conventional solid state synthesis (~1200°C), which often uses oxide or carbonate precursors. This results in finer microstructures, ~50 nm, versus the ~μm of solid

state synthesis. The cases of infiltrated electrodes will be labeled "Infiltrant-Scaffold," e.g. "SSC-GDC" or "SSC-STFC."

The oxygen electrode work in this project (Chapter 4) primarily focused on infiltrated electrodes, especially the SSC-GDC ($Sr_{0.5}Sm_{0.5}CoO_{3-\delta}$-$Ce_{0.9}Gd_{0.1}O_{1.95}$) system due to a recent comprehensive study into its coarsening kinetics.[18] In addition, LSCF ($La_{0.6}Sr_{0.4}Co_{0.2}Fe_{0.8}O_{3-\delta}$) was studied as it is a well-documented single-phase MIEC.[15] Finally, a composite electrode, $(La_{0.8}Sr_{0.2})_{0.98}MnO_{3-\delta}$/Gd-doped ceria (LSM/GDC), was characterized in Chapter 5. Composites like these will be delineated with a slash to differentiate them from the infiltrated systems above (but note well that the literature uses hyphens). This system was then infiltrated with praseodymium oxide, PrO_x, itself a high performance MIEC,[19] in order to track the surface area increase after infiltration, forming PrO_x-LSM/GDC.

Composite systems with a specific phase handling ionic conduction and one for electronic conduction form what's known as a "Three/Triple Phase Boundary" or TPB with the third phase being gas. This interface is in the form of a line in the composite of Figure 2.5 (the cross-section reducing the dimensionality of the line down to a red point). In the MIEC on the right of the figure, the "TPB" line is now a plane and is represented by the red lines, increasing the active area by an order of dimensionality. MIEC materials are therefore considered a step-change in SOFC performance.

2.4 Fuel Electrode Materials

2.4.1 Cermet anodes

Traditional anodes are of a cermet (ceramic/metallic) structure with similar phase fractions of NiO and YSZ, or NiO and GDC. The NiO is typically reduced to metallic Ni upon first exposure to fuel, and porosity develops through the cell as 41% of the volume of NiO is removed.[20]

Compared to traditional cathode materials, such as composite LSM/YSZ, well-processed Ni-composite anodes have remained relatively unmatched in terms of power density. Their flaws come from their inflexibility against coking, sulfur poisoning, nickel agglomeration, and low redox stability.[21] Compositing instead with ceria (SDC or GDC) offers coking resistance, and ceria itself is HOR-active, especially with hydrocarbon fuels.

2.4.2 Perovskite anodes

While to date perovskite anodes have struggled to surpass the polarization resistance of cermets like Ni/GDC (although Ni/YSZ was surpassed by Zhu et al.),[22] they offer greater redox and coking stability (mechanisms that are developed below). Coking resistance has been suggested to be by way of their oxygen ion conductivity; that is, adsorbed carbon can be quickly oxidized by surface oxygen species even in a low pO_2 atmosphere.

Many of the perovskites used in oxygen electrodes are not stable in reducing atmospheres—elements like Fe and Co are reducible in anode-relevant pO_2.

Low electronic conductivity is the major detriment of all-perovskite anode materials.[23] The necessary conductivity for an anode of sufficiently low ohmic resistance is ~100 S/cm.[24] This is easily met with metals, with conductivities around 10^5 S/cm. Some perovskite materials have exceeded this but only in dry hydrogen;[25] much more typical is <10 S/cm, such as for Fe-doped strontium titanate.[26]

2.4.3 Exsolved Anodes

Recently with renewed interest, perovskite anodes have been used in exsolution-type systems in order to generate active metal particles on their surfaces; a case study with $Sr(Ti,Fe,Ni)O_{3-\delta}$ will be extensively covered in the introduction to Chapter 6. These particles,

typically Ni, Co, Fe, and/or Ru, have previously demonstrated catalytic activity for the HOR or carbon monoxide oxidation.

Decomposition in the context of solid oxide cell electrodes implies thermochemical reduction of the desired polycation oxide to stabler oxides and metals. As a degradation mode, decomposition is unintended and results from operating in an environment of slow, but nonetheless thermodynamically preferred, phase transformation. Exsolution, on the other hand, is the intentional loss of a particular cation or cations from a solid solution and into a surface metal phase in the beginning seconds to hours of operation. The initial switch from oxidizing to reducing atmosphere causes a cascade of Schottky defects (in the case of Ni, $\emptyset \rightarrow V_{Ni}'' + V_O^{\bullet\bullet}$) in the parent oxide lattice or can lead to an additional concomitant oxide phase transformation, for example, from the perovskite structure to the alternating rock-salt/perovskite, i.e., Ruddlesden-Popper, structure. This process is considered in-situ self-assembly and it is unique in the synthesis methods available to SOFC fabrication.

A critical nucleus is required for the new phase to form, which can occur sub-surface or superficially depending on the system and conditions.[27] Neagu et al. found that the particle will grow until the availability of cations is depleted[28]—this can be a localized effect, wherein the surface perovskite has been drained of exsolvable cation and further bulk exsolvable species can no longer diffuse through the phase boundaries.

Because the cation depletion is highly localized, a phase transformation of the host perovskite is often reported. A-site rich perovskites spontaneously transform to the Ruddlesden-Popper structure, in which a rock-salt layer comprised of the A-site oxide (in many cases, SrO) alternates in layers with the perovskite, with the number of perovskite layers equaling n before reaching another SrO. Hence, the most extreme R-P phase for strontium titanate, then, is the n=1

Sr_2TiO_4, which can also be written $(SrO)(SrTiO_3)_{n=1}$. Many systems have been found to display this exsolution effect, whereby either single metal species or binary or even ternary alloys are reported to exsolve.

Previous studies have revealed a superiority of the A-site deficient form of perovskites.[22, 29] This strategy reduces A-site occupancy to both coax exsolution and cause the ensuing perovskite to be less off-stoichiometry.[30-32] Another strategy often employed is "pre-reduction" of the anode for increased stability, sometimes at the expense of 0-hour performance.

2.5 Degradation Phenomena in SOFC Electrodes

Except for microstructural coarsening, the dominant degradation pathways in oxygen and fuel electrodes differ, and to a certain extent, under fuel and electrolysis conditions as well. In the following, I will briefly remark on the main degradation pathways in fuel cell mode of both electrodes, referencing review articles where applicable. For some degradation pathways, materials innovation has allowed for an avoidance/mitigation of the pathway itself; in others, the general philosophy is to make initial performance high enough that "headroom" is created, slowing the electrode to degrade and still operative satisfactorily above a threshold of performance.

2.5.1 Coarsening

For many finely processed SOC electrodes, especially ones with nanoscale features such as the infiltrated electrodes under consideration, coarsening is a major degradation mode. Nanoparticles with high volumetric specific surface area allow for an increased number of catalytic sites, leading to exceptionally high 0-hour performance. However, via Ostwald ripening,[33] these nanoparticles sinter and coalesce over time, reducing the area of the energetic air-catalyst interface, and leading to an increased average particle size and decreased overall number of particles. In the infiltrated, nano-structured SSC-GDC system, a model was produced

to predict the effects of coarsening throughout the projected 40,000 h lifetime of the cathode. The time dependence of the resistance was stated as[18]

$$R_{P,C} = \sqrt{\frac{R_S}{\sigma_{ion} Cf}} (l_{C,0}^n + K_D t)^{1/2n} \coth\left(L(l_{C,0}^n + K_D t)^{-1/2n} \sqrt{\frac{Cf}{\sigma_{ion} R_S}}\right) \quad \textbf{(Equation 2.8)}$$

with parameters from literature and others that were fit using experimental data across different temperatures. Once modeled, a %/kh degradation rate can be calculated as an assay of cell stability. A region that balanced a DOE target degradation rate, <0.5%/kh,[34] and a sufficiently high initial performance, <0.2 Ω•cm^2, was mapped, demonstrating that the lowest operating temperature for SSC-GDC is found to be 600°C with a starting particle diameter of 35 nm.

2.5.2 Cation surface segregation (Oxygen Electrode)

Certain A-site species in perovskite electrodes, e.g., Sr in SSC and LSCF, have the propensity to diffuse to the air interface and form active-site blocking Sr-based compounds like SrO or $SrCO_3$ atop oxygen electrodes.[35] In LSCF, a single-phase cathode without nanoparticle infiltration, Sr-segregation is the dominant degradation mechanism and is exacerbated at high temperature.[36] A recent study has shown that an electrostatic driving force between Sr^{2+} (Sr'_{Sm}) and O^{2-} vacancies ($V_O^{\bullet\bullet}$) at the surface is an important factor inducing the formation of a surface insulating layer of SrO(s).[37] This is an especially deleterious effect as only a small amount of surface SrO is needed to shut down a disproportionately large percentage of cell activity, due to its favorability of blocking especially active but fewer Co-terminated surface sites, as seen in an analogous $La_{0.6}Sr_{0.4}CoO_{3-\delta}$ system.[38]

2.5.3 Chromium Poisoning (Oxygen Electrode)

Interconnects, or the components that turn a collection of SOFCs into an SOFC stack, are most cost-effectively made from ferritic stainless steel with 17-22% chromium in order to resist the oxidizing atmosphere of the oxygen electrode at high temperature.[39] A protective chromia surface layer, Cr_2O_3, that is still electronically conductive, forms on the interconnect materials, but it is this same oxide layer that is subject to volatilization in the form of the more highly oxidized $CrO_2(OH)_2$ and CrO_3 species. The volatile chromia species can then deposit within the oxygen electrode and block active sites, with exact mechanisms under debate and differing by electrode material. This degradation phenomenon has been identified as the single largest contributor to decreased SOFC stack lifetimes.[9] Strategies to mitigate it are focused on either improving electrode materials so that the performance drop is tolerable (either by being great catalysts at 0-hour or by forming less impactful Cr-containing species) or via the use of Cr getters before volatized Cr can reach the active electrode.[40]

2.5.4 Coking (Fuel Electrode)

When carbon-based fuels (hydrocarbons and alcohols) are used with SOFCs, there is a possibility of solid carbon formation, called coke, the process by which it forms called coking. The most common fuel used in industry with SOFCs is methane, CH_4. A reaction whereby methane cracks is one common way that solid carbon is formed, via $CH_4 \rightarrow C + 2H_2$. Alternatively, either before reaching the cell or in the cell itself, methane can reform into CO (and CO_2) and H_2 (and H_2O) species. CO can then be a coke precursor via the Boudouard reaction, also known as CO disproportionation. This reversible process is a consequence of the thermodynamic equilibrium among C, CO, and CO_2. Nickel, the most common catalyst in fuel electrodes for the HOR, is also an effective catalyst for carbon formation. Carbon forms through a dissolution process, eventually

nucleating as whiskers and pushing Ni particles up and away from the electrode structure; this same technique has been used intentionally to grow carbon nanotubes.[41]

2.5.5 Sulfur Poisoning (Fuel Electrode)

As a consequence of SOFCs having been historically operated with natural gas, sulfur poisoning has been prominently studied. Contaminants, primarily in the form of H_2S, can have a concentration exceeding 1% and can lead to a poisoning of active sites. This will remain a problem if fuels are transitioned to biogas, with an expected ppm of up to 200 ppm.[42] It has been proposed that S species physically adsorb after dissociating from H_2 on the surface of Ni, or that chemical Ni sulfide bonds form. In any case, redox cycling is one possible mechanism to reactive redox-stable anodes by oxidizing S to gaseous SO_x. Sulfur poisoning has also been proposed to occur on the oxygen electrode through reaction with surface SrO species.[43]

2.5.6 Redox Cycling (Fuel Electrode)

Ni-metal composite electrodes require that pO_2 stays below 10^{-16} bar,[44, 45] which can be achieved even at 0.1% H_2 and 99.9% H_2O (therefore electrolysis operation in nearly pure water can be conducted), but in the absence of hydrogen (e.g., the fuel is interrupted), any amount of oxygen in a realistically sized chamber will react to form NiO, resulting in +70% volume expansion.[46] Given oxygen ion conduction through the solid oxide electrolyte, significant pO_2 would ensue. When this occurs with structural nickel, such as in an anode-supported cell, catastrophic failure of the cell may ensue as cracks can lead to a compromised electrolyte. In the case of non-structural but percolated nickel, cracks can still result in a major loss in performance as portions of the electrode become electronically isolated.

Redox cycling on perovskite electrodes is currently not well understood but is the focus of Chapter 6. However, given that the metal phases in exsolved systems are expressed as disparate,

socketed entities within a perovskite matrix, it is not expected that redox cycling should necessarily result in performance loss.

2.6 Electrolytes and cell architecture

While this dissertation is focused on electrode development, two other design considerations are the choice of electrolyte and the cell architecture. The simplest architecture for electrode development is the electrolyte supported symmetric cell, which makes sacrifices on overall performance in order to easily apply thin inks (<50 μm) via screen-printing onto both sides of relatively thick electrolytes (~200 μm), thereby creating relatively large ohmic resistances by consequence of long ionic diffusion distances. A common electrolyte material for oxygen electrode development is Gd-doped ceria, described previously, because it has a conductivity of 0.03 S cm^{-1} at 700°C and is chemically compatible (inert) with the often Sr-containing electrodes. However, in low pO_2 environments, such as for fuel electrode testing, it gains significant electronic conductivity, causing leakage current and lowering OCV.

Therefore, to test in reducing atmospheres, zirconates are often used, and historically they have been the most popular in industry in which operating temperatures remain relatively high (>700°C). Their downsides are that their low temperature conductivity is low, and all must employ a doped-ceria barrier layer to prevent Sr-zirconate formation on the cathode side when used with the most popular cathode materials. ZrO_2 stabilized with 8 mol.% Y_2O_3 (YSZ) displays conductivities of 0.02 S cm^{-1} at 700°C, which can be further improved by instead doping with 9.3% Sc_2O_3, yielding 0.05 S cm^{-1}. Finally, $La_{0.9}Sr_{0.1}Ga_{0.8}Mg_{0.2}O_{3-\delta}$ (LSGM), a perovskite electrolyte, can achieve 700°C ionic conductivity of 0.04 S cm^{-1}.[47] Of these choices, at low temperature operation (<600°C), the conductivities are GDC > LSGM > ScSZ > YSZ, with only LSGM and GDC being realistic electrolytes for ~10 μm thick electrolytes.[15] Bismuth-oxide based

electrolytes have even higher conductivities, but processing is challenging due to their possessing a melting point lower than standard electrode sintering temperatures.

The Barnett group has experimented with anode-supported cell design produced by tape-casting structural Ni/YSZ, which has resulted in our highest performance to date, approaching 3 W cm^{-2} at 750°C in conjunction with other optimization.[48] The primary advantage of this approach is that electrolyte thickness can be reduced to ~2 μm, reducing the necessary ionic diffusion and thus lowering cell ohmic resistance.

Another strategy which can reduce ionic diffusion distance is the cathode-supported cell, in which structural cathode material is tape casted. Efforts in the Barnett group have produced LSM/YSZ supports infiltrated with PrO_x to extend active sites, approaching 2.5 W cm^{-1} at 800°C.[49] One benefit of this approach is that a greater range of anode materials can be used via the screen-print process, such as the STFN featured heavily in this work.[50]

Finally, other cell designs are the metal-supported cell, in which ferritic stainless steel (similar to the interconnect) can be used as structural material, again with a thin electrolyte, offering high redox stability and fast start-up times (particularly useful for transportation applications),[51] and tubular SOFCs, which are still often anode-supported but offer improved volumetric power density.[52]

2.7 Atomic Layer Deposition

Atomic layer deposition is a subset of chemical vapor deposition (CVD) that relies on coating a substrate with two alternating gaseous precursors to produce, typically, an oxide: Reactant A with the desired coating metal, e.g. Al in trimethylaluminum (TMA) or Zr in Tektrakis(dimethylamido)Zirconium(IV) (TDMAZ), and Reactant B, an oxidant, typically one of water vapor, oxygen gas, or ozone. Water vapor is most commonly used.

A deposition proceeds as follows: (1) vacuum is pulled, (2) an inert carrier gas is continuously flowed, (3) Reactant A is pulsed for x ms, (4) the chamber is allowed to purge with nitrogen, (5) Reactant B is pulsed for y ms. The cycle then proceeds back to step (2) for n number of cycles. In this fashion, at a constant, ~1 Å/cycle deposition rate, an oxide is built upon the surface, even a surface of complex morphology.

The benefit of ALD over other thin film deposition techniques is, in theory, its self-limiting conformality. Due to steric hindrance effects of the metallic precursor's end-groups, once a layer has been chemically adsorbed onto all available active sites of the surface, it saturates, and remaining excess reactant flows to the outlet without reacting. Then, Reactant B is used to oxidize away the remaining end-groups forming oxygen terminations on the surface, converting it again to reaction-ready surface.

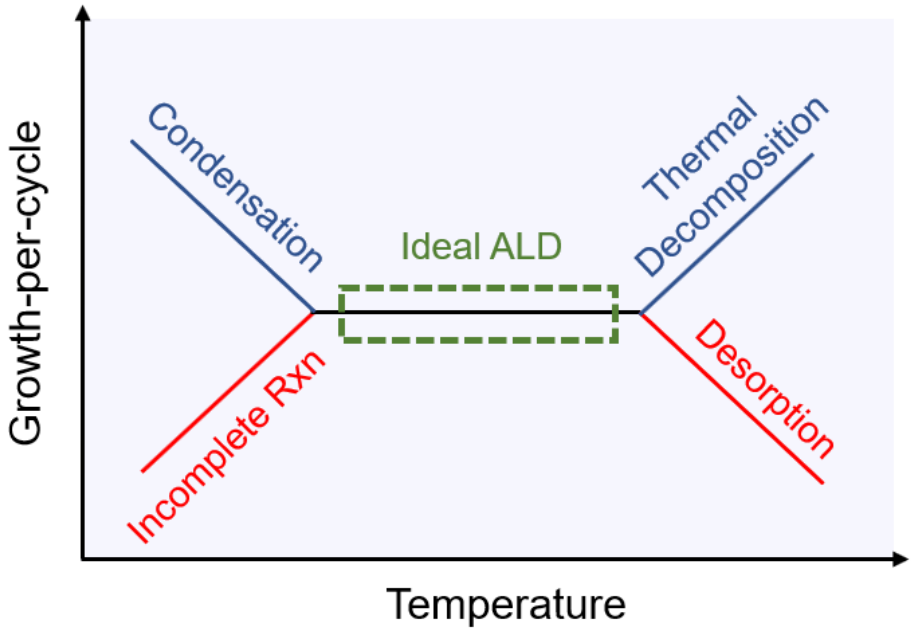

Figure 2.6 The "ALD Window" in which precursors result in conformal, uniform coverage of complex substrates. Temperatures that are too high or too low can result in abnormally high or low growth-per-cycle.[53]

However, ALD is a conceptually ideal case of CVD, and aside from the truly prototypical TMA precursor, almost every other is susceptible to CVD-type deposition aberrations, like thermal decomposition, which lead to uncontrolled growth. An ALD window describes the idealized temperature range at which growth per cycle is limited no matter the amount of reactant flowed in, and around it are four mechanisms that could lead to uneven growth.

While many ALD precursors are effective in conformally coating relatively flat surfaces, deposition onto surfaces with aspect ratios in excess of 100,[54-56] in which precursor gas has to flow through long, narrow passages, suffers from slow diffusion of the precursors and purging of the excess reactant and reaction products, leading to a higher susceptibility to the detracting mechanisms seen in Figure 2.6. The result for high aspect ratio, porous structures, is an unavoidable but mitigatable deposition gradient inward from higher thickness near the structure surface. This "CVD type growth" was noted for Tetrakis(ethylmethylamino)Zirconium(IV) and O_2 precursors deposited into reduced Ni/YSZ to act as oxidation barriers, in which maximum penetration of the precursor was ~30 μm before becoming unmeasurable.[57]

3 Methods

Experimental fabrication and processing were carried out using a combination of resources, with devices fabricated in lab either from powder or using certain components from suppliers. Electrochemical testing was performed using Barnett group equipment, and all other forms of characterization were employed via the expansive shared facilities at Northwestern.

3.1 Cell Preparation

Symmetric oxygen electrode cells and symmetric fuel electrode cells were prepared similarly. In the case of oxygen electrodes, Gd-doped ceria was prepared via pellet pressing of ultra-high surface area $Gd_{0.1}Ce_{0.9}O_{1.95}$ powder (Rhodia) using 1.5 metric tons of pressure. Fuel electrodes were prepared atop commercial scandia-stabilized zirconia (ScSZ) electrolyte pellets of ~200 μm thickness (Fuel Cell Materials Hionic), which either came prepared with an Sm-doped ceria barrier layer ~3 μm, or were later printed with a Gd-doped ceria layer in-house.

3.1.1 SSC-GDC and LSCF Oxygen Electrodes

Cells were processed using the procedure described in Call, Railsback et al.[18] Identical GDC (Rhodia) ink layers were screen printed on opposite sides of dense GDC electrolyte pellets and fired at 1100°C for 4 h, yielding porous scaffolds with ~20 μm thickness and an area of ~0.5 cm^2. A nitrate solution was then infiltrated into the porous GDC and calcined at 800°C for 0.5 h; this procedure was repeated ~8 times to yield stoichiometric SSC nanoparticles decorating the GDC pore surfaces with a volume fraction of ~20%. $La_{0.8}Sr_{0.2}MnO_{3-\delta}$ (LSM) (Praxair) was screen printed over the infiltrated scaffolds and fired at 800°C for 2 h to yield porous current collector layers ~10 μm thick. Other cells used for imaging were identical except for ~35 μm SSC–GDC layers and ~20 μm LSM (a consequence of the variation in screen-printing pressure by operator). LSCF ($La_{0.6}SrCo_{0.2}Fe0.8O_{3-\delta}$) cells were prepared similarly with acquired powder (Praxair,

Washington). For electrochemical testing, silver grids and wires were then affixed to the electrodes.

3.1.2 SSC powder characterization

SSC nanopowder with <50 nm particle size and >25 m^2g^{-1} specific surface area (MilliporeSigma) was used as an analog for the SSC electrodes, allowing additional characterization of the interaction of ALD-ZrO_2 with SSC. Microscopy was done using SSC powder suspended in ethanol, sonicated, and pipetted onto lacey carbon grids. For ICP-OES (described later) SSC powder was prepared by agitating in a vortex mixer for 5 minutes in a solution of MilliPore water and filtered through Amicon Ultra-4 Centrifugal Filter Units. The powder composition was checked by ICP-OES, after dissolving in 1:1 hydrochloric and nitric acid, and was found to be $Sr_{0.47\pm0.01}Sm_{0.42\pm0.01}Co_{1\pm0.12}O_x$.

3.1.3 STF(N) Symmetric Fuel Electrode Synthesis

Solid state synthesis of $SrCO_3$ (Aldrich), TiO_2 (Aldrich), Fe_2O_3 (Alfa Aesar), and $Ni(NO_3)_2 * 6H_2O$ (Strem) was conducted at 1200°C in air following the protocol in Zhu et al.[22] The powders were ball-milled pre- and post- calcination for 4 days in ethanol. The powder was then combined with Heraeus V-737 vehicle with a ratio of 1:1.2 powder:vehicle and processed through a 3-roll mill to produce an ink. This ink was then screen-printed (Sefar, Inc. screens) onto symmetric ScSZ electrolytes (Fuel Cell Materials) with GDC barrier layers (Rhodia – inks were made similarly with 1:1.2 V-737 vehicle, fired at 1400°C for 3 hours) with areas of 0.5 cm^2. The cells were then fired at 1150°C in air for 3 hours. Gold (Heraeus C4300UF) grids were then screen-printed for current collectors and fired in air at 900°C. Silver wires (Alfa Aesar) were braided and attached with silver paste (DAD-87 Shanghai Plastics Research Institute).

3.1.4 Ni/YSZ synthesis

Ni/YSZ composite powder was mixed as 50:50 w/w and ball-milled for 48 hours, before preparing in a 1:1.2 powder:vehicle ink with Heraeus V-737. The procedure then followed as in 3.1.3. For the Ni/YSZ cell used to measure the limits of ALD penetration in Chapter , a symmetric tape-casted Ni/YSZ cell was used that was prepared as in Park et al.[58]

3.2 Atomic Layer Deposition

3.2.1 ZrO_2 atomic layer deposition

ALD was carried out using a Savannah S100 and Arradiance GEMstar-8 ALD system at 250°C. The ALD cycle for SSC-GDC cells consisted in sequence of: (1) 0.15 s pulse of $H_2O_{(v)}$; (2) 5 s N_2 gas purge; (3) 0.40 s pulse tetrakis(dimethylamido)zirconium(IV) (TDMAZ); and (4) 5 s N_2 gas purge. Three sample configurations were coated. SSC powder was coated with 7 cycles by dispersing in ethanol, pipetting onto glass or silicon, and then drying. For STEM studies, SSC powder on TEM grids was coated using 3, 30, and 60 cycles by enclosing the grids in a vented Al-foil cage inside the ALD chamber. SSC–GDC electrodes in symmetric cells were coated with 30, 60, and 300 cycles; deposition on both electrodes was allowed by suspending the cells over the substrate holder using glass slides or clips at the edges of the cells. The ZrO_2 thickness decreases significantly with increasing depth into the electrodes, and this effect is quantified in Atomic Layer Deposition of Zirconia for Coarsening Inhibition of Infiltrated Solid Oxide Oxygen Electrodes. A similar effect presumably also occurs in coating SSC powders, such that ALD coating effects observed in powders are probably reduced due to a lesser ZrO_2 thickness.

The LSCF symmetric cells were coated in an Arradiance GEMStar 8 system, with a recipe of: (0) 5hr degas period at a constant N_2=25 sccm; (1) 5s TDMAZ; (2) 50s N_2 purge; (3) 5s pulse of $H_2O_{(v)}$; (4) 50s N2 purge. Samples of 1, 10, and 100 cycles were produced.

3.2.2 Al_2O_3 Atomic Layer Deposition

ALD was carried out using an Arradiance GEMstar-8 ALD system with trimethylaluminum (TMA) and water vapor as the oxidant. The reactor had a plasma head necessitating only short periods of time in "exposure mode" in which the evacuation actuator valve was closed and precursor was allowed to permeate. The recipe was as follows:

(1) Pump to 15 mTorr (2) Heat to 200°C, (3) Wait 10 minutes, (4) Set N_2 flow to 20 sccm, (5) Wait 1 s (6) Close Chamber, (7) Pulse TMA 11ms, (8) Wait 1.5 s, (9) Open Chamber, (10) Loop to Step 4, 4x, (11) Set N2 flow to 90 sccm, (12) Delay 20 s, (13) Set N_2 flow to 15 sccm, (14) Wait 1 s (15) Close Chamber, (16) Pulse H_2O 11ms, (17) Wait 1.5 s, (18) Open Chamber, (19) Loop to Step 11, 4x, (20) Loop to step 4, 50x.

In this fashion, 50 cycles of TMA at approximately 1.25 Å/cycle were deposited for a total of 6.25 nm.[59] A version of the recipe with 22 ms doses was also used and it resulted in the same concentration of alumina, so 11 ms (4x) was determined to be a saturating dose.

3.3 Electrochemical characterization

Electrochemical impedance spectroscopy (EIS) was conducted with a Zahner IM6 with a 20mV perturbation in the frequency range 50^6 to 0.5 Hz. Impedance fitting was done with either RAVDAV software[60] programmed in Python which relies on the scientific Python stack.[61-63] or Impedance.py software.

3.3.1 SSC-GDC and LSCF Testing

Cells were first ramped to 600°C for an initial EIS measurement and then ramped to the accelerated ageing temperature of 750°C where they remained except for periodic decreases to 600°C for EIS measurements. The cycle of ramping down, testing, and ramping up took ~2 hours and <4% of the total ageing time. A schematic of a similar life-test schedule is given

elsewhere.[18] The SSC–GDC cells were fabricated in the same batch using identical materials and conditions in order to facilitate meaningful comparisons. The dataset for the uncoated SSC–GDC electrode (i.e., with no ALD coating) was first published by Call et al.[18] LSCF was tested similarly but was maintained at 750°C throughout testing and ageing.

3.3.2 Hydrogen and Redox Testing

Symmetric fuel electrodes were tested in 97% H_2 flowed through a room-temperature bubbler, imparting 3% steam, for a total of 100 sccm. A single-bore alumina tube with a closed end was used with the hydrogen being delivered near the cells, nearest to the closed end. The open end of the tube was insulated with alumina and zirconia felts, and sealed with Kapton tape, with a puncture to allow gas egress. In this fashion, the overpressure of hydrogen out of the tube is used to maintain a consistent reducing atmosphere, and hydrogen exits away from the furnace, well below its auto-ignition temperature.

The complete redox cycle used during electrochemical testing is shown in below Figure 3.1. It was designed so that the material is never in a reducing atmosphere above the testing condition of 700°C. The higher oxidation temperature was selected after preliminary testing revealed greater "resetting" behavior in perovskite anodes versus resetting at the operating 700°C condition, and 850°C is a reasonable operating limit for SOFCs.

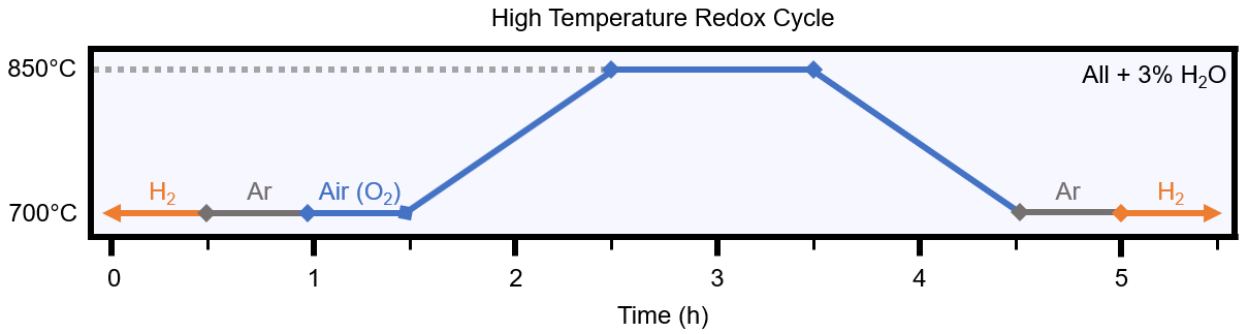

Figure 3.1 Redox cycle with a temperature excursion to 850°C during oxidation.

The oxidant in the redox cycle was room air delivered via pump at ~100 sccm and was also flowed through the room temperature bubbler. The humidified argon step was found to be partially oxidizing, with the manufacturer (UHP, Airgas) specifying <1 ppm O_2.

3.3.3 Accelerated Coke Testing

To examine the propensity for electrode material to coke, a bubbler design was devised to allow a simple change between humidified hydrogen and ethanol + hydrogen. Room temperature water imparts ~3% steam, and room temperature ethanol ~6%. Hydrogen flowed through the ethanol was completely dry. This has the benefit that no steam reforming can take place, and water gas-shift will not remove any deposited carbon. A dual-bubbler system was assembled and is depicted in Figure 3.2.

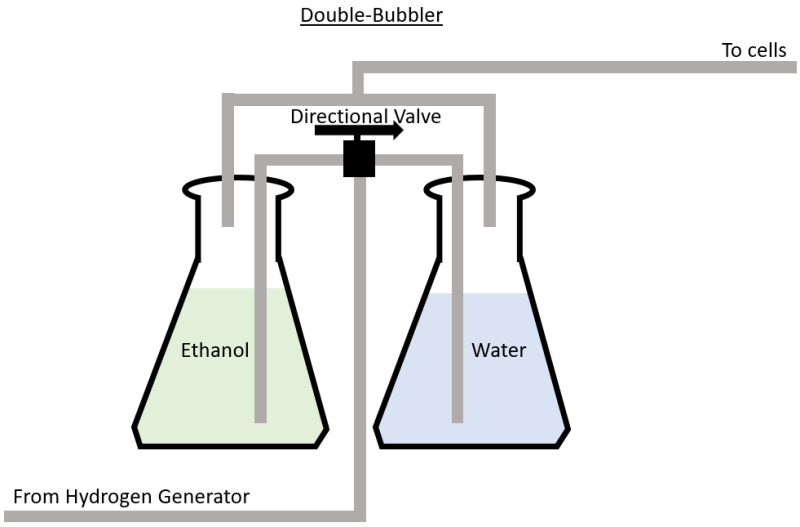

Figure 3.2 A bubbler system that allows a user to switch from hydrogen in water to hydrogen in ethanol without interruption of an electrochemical experiment.

Another benefit of the double-bubbler system is that no purge gas was required when switching between the two solutions as a constant hydrogen overpressure is maintained in each bubbler. In ethanol mode, a nonzero amount of ethanol could still evaporate through the system,

but the direction of the pressure differentials was such that this should be negligible. In a previous iteration of the dual-bubbler system, two directional valves were used in order to truly isolate the active bubbler from the inactive bubbler, but since the bubblers rely on slight over-pressures to stay air-free, this design had the potential to deliver initially significant pO_2 upon switching between bubblers and was therefore a safety hazard.

3.4 X-ray characterization

X-ray powder diffraction was carried out using a STOE Stadi-P, a Scintag XDS2000, and a Smartlab 3kW Gen2, all with Cu Kα radiation in Bragg-Brentano geometry in reflection mode for the latter two but transmission mode for the former. In-situ XRD was carried out on a Smartlab 9kW Gen3 with a combination of synthetic air, nitrogen, and hydrogen, all bubbled through room temperature water. The redox cycles used in in-situ XRD testing resemble that in Figure 3.1 but with half-hour steps replaced with one-hour steps to allow equilibrium to be observed. Rietveld refinement was conducted via the free and open-source GSAS-II software package.[64]

3.5 Electron Microscopy

3.5.1 Scanning

Solid oxide cell samples were prepared for Scanning Electron Microscopy (SEM) either in a fractured state, in which a diamond tip was used to form a fracture plane, or in an epoxy infiltrated, grinded, and polished state. The former technique is preferred to see cell microstructure since the range of depth allows much more cell material to be observed. The latter is preferred in quantifying porosity and obtaining better elemental line scans with Energy Dispersive Spectroscopy (EDS). Fractures can still be used for EDS but will be subject to topological effects. All samples were plasma-coated in ~9 nm osmium for conductivity (OPC). The sole SEM used

throughout the entire dissertation was the Hitachi SU8030. Outfitted with an Oxford AZtec X-max 80 SDD for EDS.

3.5.2 Scanning transmission

Scanning transmission electron microscopy (STEM) was employed on powder samples to resolve sub-nanoscale features. A Hitachi HD-2300 was used in 200 kV primarily in brightfield mode, with EDS capabilities, and resolving limits to ~0.23 nm.

3.6 ICP-OES

Inductively Coupled Plasma Optical Emission Spectroscopy (ICP-OES) is an analytical technique that can report the concentration of ionic species in a solution. It does this by pumping and nebulizing the solution through an argon plasma, which leads to the excitation of electron states into higher energy levels—when the electrons relax, electromagnetic energy is released with characteristic energies that can then be measured by a charge-coupled device (CCD) detector. These energies are compared against the energies measured via reference samples of known concentration (reference samples are used for each new experiment), serially diluted to comprise a large range of possible concentrations (typically 100-0.001 ppm). Concentration (w/w) can be converted to moles by multiplying by the known density and volume of the solution, and stoichiometries can then be extracted (for oxides, oxygen is unknown). This technique was used to quantify surface Sr species (Chapter 4), loading of infiltrated species, and alumina coverage to derive surface area (Chapter 5).

3.7 BET Surface Area Measurement

Brunauer–Emmett–Teller (BET) gas adsorption isotherm theory was used to extra surface area information with a Micromeritics 3Flex instrument using krypton gas. At 77K, the liquid nitrogen boiling temperature, the vapor pressure of krypton is much lower than that of nitrogen,

such that the pressure differential from adsorbed gas onto the sample surface is more significant at lower (<1 m^2) absolute surface areas.

4 Atomic Layer Deposition of Zirconia for Coarsening Inhibition of Infiltrated Solid Oxide Oxygen Electrodes

This chapter has been adapted and expounded upon from the publication, "ZrO_2 atomic layer deposition into $Sr_{0.5}Sm_{0.5}CoO_{3-\delta}$–$Ce_{0.9}Gd_{0.1}O_{2-\delta}$ solid oxide fuel cell cathodes: mechanisms of stability enhancement" by T.A. Schmauss, J.G. Railsback, M.Y. Lu, K.Y. Zhao, and S.A. Barnett.[65]

4.1 Abstract

The application of atomic layer deposition (ALD) on solid oxide fuel cell (SOFC) cathodes has previously yielded mixed results and has been seen to depend on the ALD species, catalyst chemistry, catalyst morphology, and the conditions for deposition. Characterized here is the effect of an ALD zirconia coating within two kinds of SOFC oxygen electrode: $Sr_{0.5}Sm_{0.5}CoO_{3-\delta}$ infiltrated into Gd-doped ceria, $Ce_{0.9}Gd_{0.1}O_{1.95}$, scaffolds (SSC–GDC) and single-phase $La_{0.6}Sr_{0.4}Co_{0.2}Fe0.8O_{3-\delta}$. For the SSC-GDC, island-like ALD-ZrO_2 coatings with approximately monolayer coverage initially yield a higher electrode polarization resistance, R_P, but thereafter the coated electrodes show lower R_P and slower degradation. For example, after ~1000 hour accelerated ageing tests carried out at 750°C, SSC-GDC coated with ~0.3 nm of ALD-ZrO_2 showed an R_P increase of 18% compared to 30% for uncoated SSC-GDC. Strontium surface segregation was not found to be a significant degradation factor. At 750°C, a reaction between the Zr-overlayer and the SSC was observed, producing $SrZrO_3$, Co_3O_4, and $SmCoO_3$. The low R_P values achieved suggest that the reactant products were thin enough to be discontinuous and thus not hinder the oxygen surface exchange process, and yet they acted as a barrier to SSC particle coarsening. For the LSCF, no such performance increase was noted, due to the much more

uniform deposition as well as its primary mode of degradation being Sr surface segregation rather than coarsening.

4.2 Introduction

Low temperature (400–650°C) solid oxide fuel cells (SOFCs) are being developed to improve system economics, e.g., via lowering balance-of-stack costs and extending SOFC stack lifetimes.[15] However, low-temperature oxygen electrodes typically utilize highly active, nano-scale mixed ionic-electronic conductors (MIECs) such as $Sr_{0.5}Sm_{0.5}CoO_{3-\delta}$ (SSC)[66] to accelerate the sluggish oxygen reduction reaction. These electrodes are susceptible to degradation phenomena such as microstructural coarsening that are exacerbated by decreasing electrode feature sizes, but are fabricated as such in an attempt to reduce low-temperature polarization resistance, R_P.[18, 66-68] Recent studies suggest that the need to maintain long-term stability by reducing coarsening will limit the R_P that can be achieved at low temperatures.[68, 69]

Atomic layer deposition (ALD) of thin, conformal ZrO_2 has recently been applied to SOFC cathodes with the aim of limiting degradation.[70] ZrO_2 overlayers were shown to curb degradation of infiltrated $La_{0.6}Sr_{0.4}CoO_{3-\delta}$ (LSC) in $La_{0.80}Sr_{0.20}Ga_{0.83}Mg_{0.17}O_{3-\delta}$ (LSGM) scaffolds[71] and $La_{0.6}Sr_{0.4}Fe_{0.8}Co_{0.2}O_{3-\delta}$ (LSCF)/$Ce_{0.8}Gd_{0.2}O_{1.9}$ (GDC) composite scaffolds.[72] It has been suggested that the applied ALD layers are porous and may exhibit mixed conductivity due to diffusion of impurities (e.g., Fe or Co) from the MIEC into the ZrO_2 lattice, such that the resultant doped zirconia allows for the reduction of O_2. Two mechanisms for the ALD stability improvement have been suggested—suppression of MIEC coarsening and/or inhibition of cation surface segregation. Coarsening could be mitigated if the ALD layer acted as a barrier to the underlying catalytic layer's self-diffusion, whereas it is posited that cation segregation could be mitigated *via* formation of a negative space charge region[71] or a decrease in the number of positive electron holes.[72] However,

other cases of ALD-ZrO_2 applied to both an infiltrated and composite system, e.g., $La_{0.8}Sr_{0.2}FeO_{3-\delta}$–ytrria-stabilized zirconia (LSF–YSZ)[73] and LSCF/GDC,[74] were found to have provided no benefit to performance and were suggested to have irreversibly blocked active sites. In at least the LSF–YSZ case, deposition conditions differed: rather than purging excess reactant/reaction products by continuously flowing carrier gas, vacuum was pulled after each pulse of precursor for their removal.

Results using ALD oxides other than ZrO_2 on SOFC cathodes have been mixed as well. ALD-CoO_x on LSC thin films led to increased polarization resistance,[75] but lower resistance was successfully achieved on an $La_{0.8}Sr_{0.2}MnO_{3-\delta}$ (LSM)/YSZ composite scaffold.[76] Additionally, ALD-Al_2O_3 on $La_{0.8}Sr_{0.2}FeO_{3-\delta}$ (LSF) infiltrated into YSZ,[77] and CeO_x and SrO on LSF, LSC, and $Ba_{0.5}Sr_{0.5}Co_{0.8}Fe_{0.2}O_{3-\delta}$ (BSCF) infiltrated into YSZ,[78] were all found to hinder cell performance, while Bi_2O_3 on LSM scaffolds,[74] LaO_x on LSF/YSZ,[73] and a LaO_x/SrO_x/CoO_x super-cycle onto an LSCF thin film[79] increased performance. Factors of precursor, the underlying catalytic substrate, and the deposition parameters used may all be important in combination for determining the performance of an ALD-modified electrode.

In this study, we analyze the effect of the most commonly applied ALD species, ZrO_2, on the electrochemical properties and stability of cathodes made by infiltrating SSC into GDC scaffolds (SSC–GDC) on a GDC electrolyte. This system was previously studied in detail to model degradative effects, thought mainly to be caused by coarsening;[18] the present results extend the life-testing to ALD-ZrO_2-coated SSC–GDC electrodes. Furthermore, extensive characterization was carried out to determine the actual ALD layer thickness in the electrode active region and the reactions between the ALD layer and the SSC. The results indicate that with careful control of the

ALD-ZrO_2 thickness, electrode stability can be improved due to the presence of a very small amount of zirconate phase in the MIEC active layer.

4.3 Results

The effects of ALD-ZrO_2 on electrode electrochemical characteristics and scaffold chemistry and morphology are described in Section A. The characteristics of the ALD process, particularly the ZrO_2 thickness distribution versus position in the electrode, are described in Section B. Further characterization probing the effects of ALD-ZrO_2 and its interactions with SSC, using SSC nano-powder as a surrogate for the SSC-infiltrated electrode, is detailed in Section C.

4.3.1 Electrochemical characterization

The EIS data of the coated and uncoated cells are summarized in Figure 4.1, with the high-frequency intercept impedance, Z′, set to 0 for all cells to highlight changes in the polarization response. The total polarization resistance values, R_P, measured within 1 h of reaching 600°C, are higher for the ZrO_2-coated cells than for the uncoated cell. However, after ageing for 48 hours at 750°C and returning to 600°C for testing, the coated electrode R_P values have dropped below that of the uncoated electrode, suggesting that the 750°C treatment yields considerable changes in the ZrO_2-coated SSC–GDC cells. A small decrease in polarization resistance for the uncoated electrode is also seen, which has been described previously as a break-in effect.[80, 81]

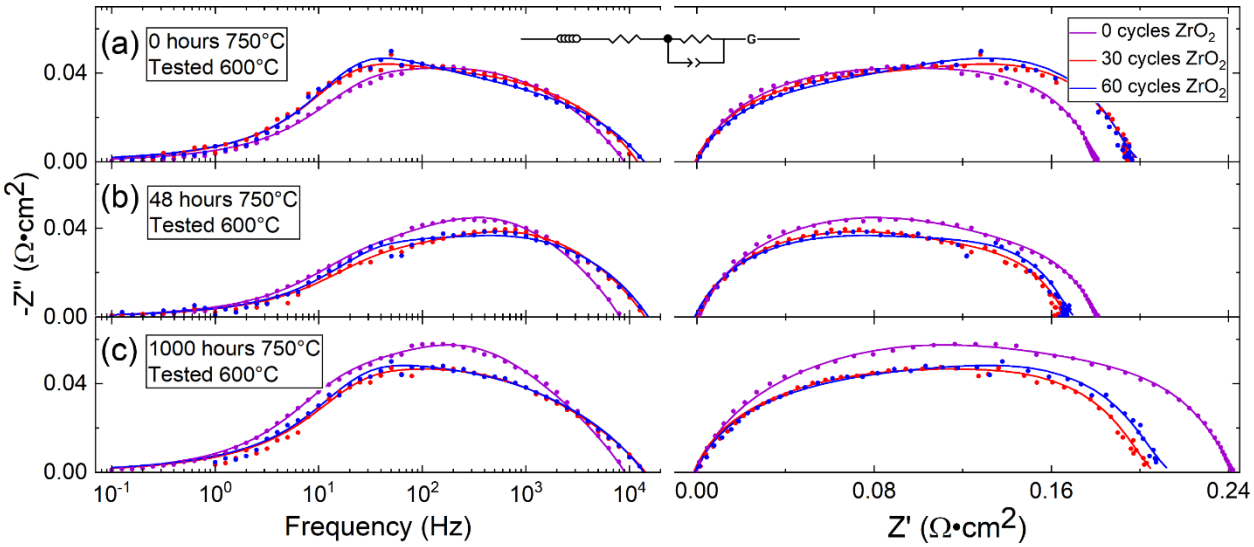

Figure 4.1 Bode and Nyquist plots of EIS spectra from 0, 30, and 60 cycles ALD-ZrO_2-coated SSC–GDC cells, taken at 600°C (a) shortly after the initial heating of the cell to 600°C, (b) after approximately 48 hours of ageing at 750°C, and (c) after approximately 1000 hours of ageing at 750°C. Data is fit with an equivalent circuit model consisting of an inductor, resistor, high frequency RQ element, and low frequency Gerischer element in series.[18]

The spectra were fit well by an equivalent circuit consisting of an inductor associated with the measurement circuit wiring, a resistor representing electrolyte ohmic resistance, a high frequency RQ element usually associated with solid–solid interfaces, and a low frequency Gerischer element accounting for electrochemical reaction and oxygen transport processes in the electrode, all in series.[18] R_P values, taken as the sum of the RQ and Gerischer resistances, were logged periodically throughout the life test and are displayed in Figure 4.2. After an initial decrease, R_P values steadily increase during the tests. However, the time rates of R_P increase for the ZrO_2-coated electrodes are less than for the uncoated electrode. These trends were reproduced in a second set of life tests aged at 800°C, with the best overall performance again achieved by the 30-cycle ALD-ZrO_2 coating cell (Figure 4.3). In summary, the electrochemical results show a small but clearly measurable improvement in stability for the ALD-modified electrodes.

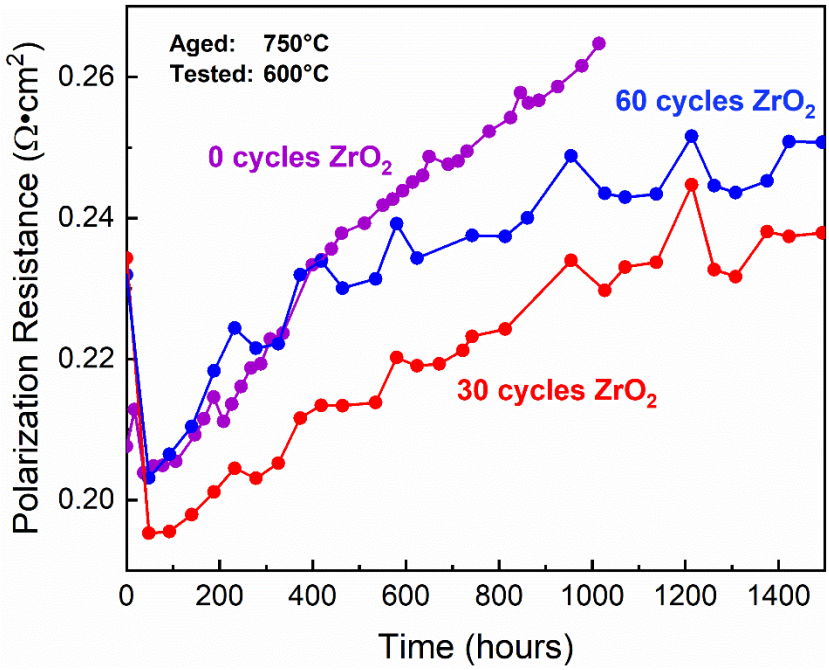

Figure 4.2 Time dependence of the polarization resistance measured in air at 600°C for cells with 0, 30, and 60 cycle ALD-ZrO_2 coated SSC–GDC electrodes. Cells were maintained at an accelerated ageing temperature of 750°C except during periodic interruptions for EIS measurements.

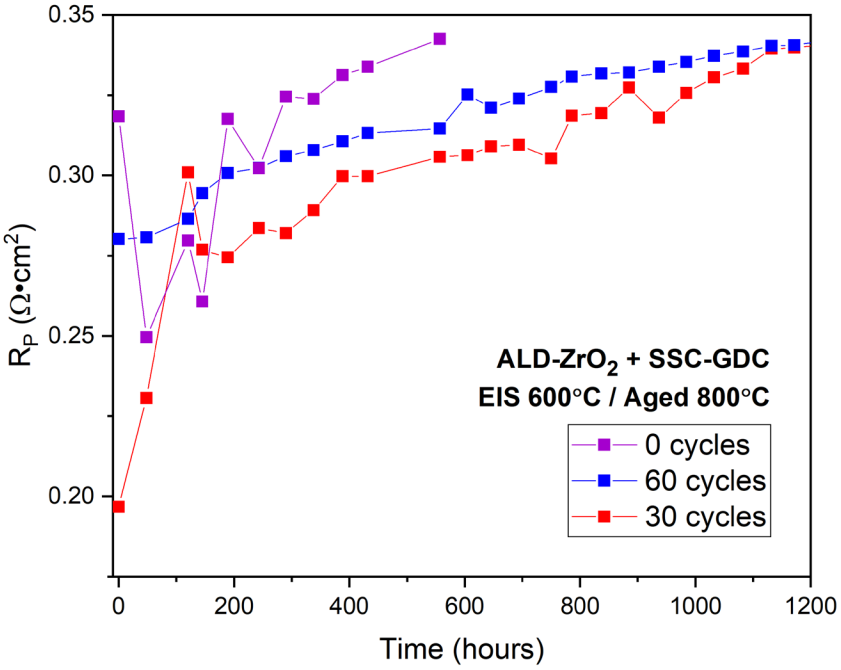

Figure 4.3 Life-test trials for three cells produced and tested with the same conditions as in the main body text, except with 800°C ageing temperatures and thicker ~35 um SSC-GDC and ~20

um LSM electrodes. Data duplicated with permission from the thesis of Kevin Zhao, Northwestern University.[82]

In testing of the LSCF electrodes, the results were similarly fit, and 0, 1, 10, and 100 cycles were compared in a similar life-test that maintained a testing and ageing temperature of 750°C, shown in Figure 4.4.

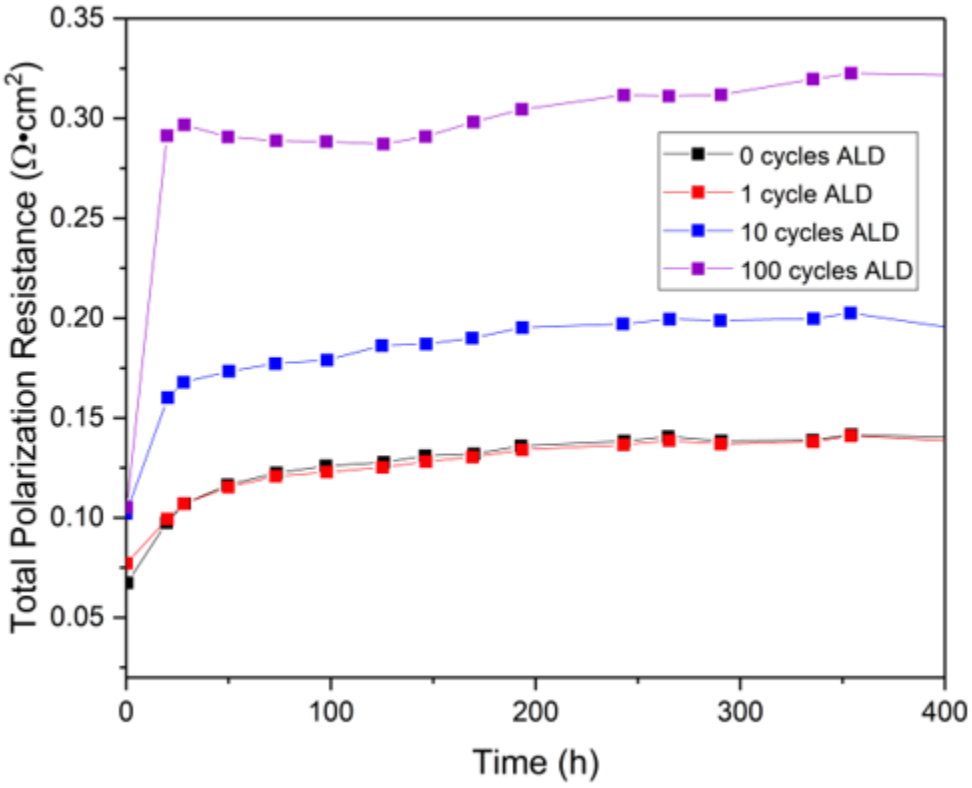

Figure 4.4 Time dependence of the polarization resistance for LSCF electrodes measured in air at 750°C for cells with 0, 1, 10, and 100 cycles of ALD-ZrO_2.

4.3.2 ALD zirconia layer characterization

It is well known that ALD coating thickness can decrease with increasing depth into a porous structure, depending on the ALD cycle conditions.[55, 83] This results when the distance that a precursor molecule has to traverse before adsorbing onto unreacted surface, relative to the pore size, is large, and subject to slow Knudsen-limited diffusion. Depending on the ALD precursor, this diffusion distance can be overcome with long soak times, but for less stable precursors, each

collision with inner pore surfaces subjects the precursor to a possibility of CVD-like thermal decomposition.[53, 84] Furthermore, it is difficult to directly measure the ALD thickness *versus* depth within the porous electrode given the discrepancy in length scales between coating and scaffold. Thus, an indirect method was used to estimate ALD zirconia thickness *versus* depth in the electrode: the nominal zirconia thickness at the electrode free surface was scaled using the measured Zr content *versus* position.

The ALD coating thickness was characterized by depositing onto ~16 nm SSC powder; this provided a surrogate that was similar to the infiltrated SSC electrode of ~50 nm starting particle size,[18] but with two advantages. First, depth of penetration effects were minimized for the thin, loosely-packed powder bed compared to the electrode, providing a thickness representative of the electrode free surface. Second, the powder could be prepared for STEM imaging with minimal processing, and hence minimal artifacts. Figure 4.5(a) and (b) show the morphology of uncoated powder and after 3 ALD cycles, respectively. The 3-cycle case shows a discontinuous coating of ~3 nm diameter ZrO_2 islands on the surface of the SSC, so it is difficult to estimate the nominal thickness. Such island formation has been reported in very thin ALD layers.[85, 86] Using the same Zr precursor and deposition temperature as in the present case, a uniformly thick layer was not observed until 40 cycles.[87] Also shown are typical images from Figure 4.5(c) 30 and Figure 4.5(d) 60 cycles of growth with uniformly thick, dense ZrO_2 layers. Layer thicknesses were measured to be 4.5 ± 0.8 nm for 30 cycles (averaged over 38 particles) and 7.5 ± 0.9 nm after 60 cycles (averaged over 58 particles) which correspond to growth-per-cycle (GPC) values of 0.15 ± 0.03 nm per cycle and 0.13 ± 0.01 nm per cycle. The 60-cycle GPC of 0.13 nm per cycle is less than a report of a similar process on perovskite nanoparticles (0.167 nm per cycle)[71] but higher than reported for a flat silicon substrate after many cycles (0.096 nm per cycle).[88]

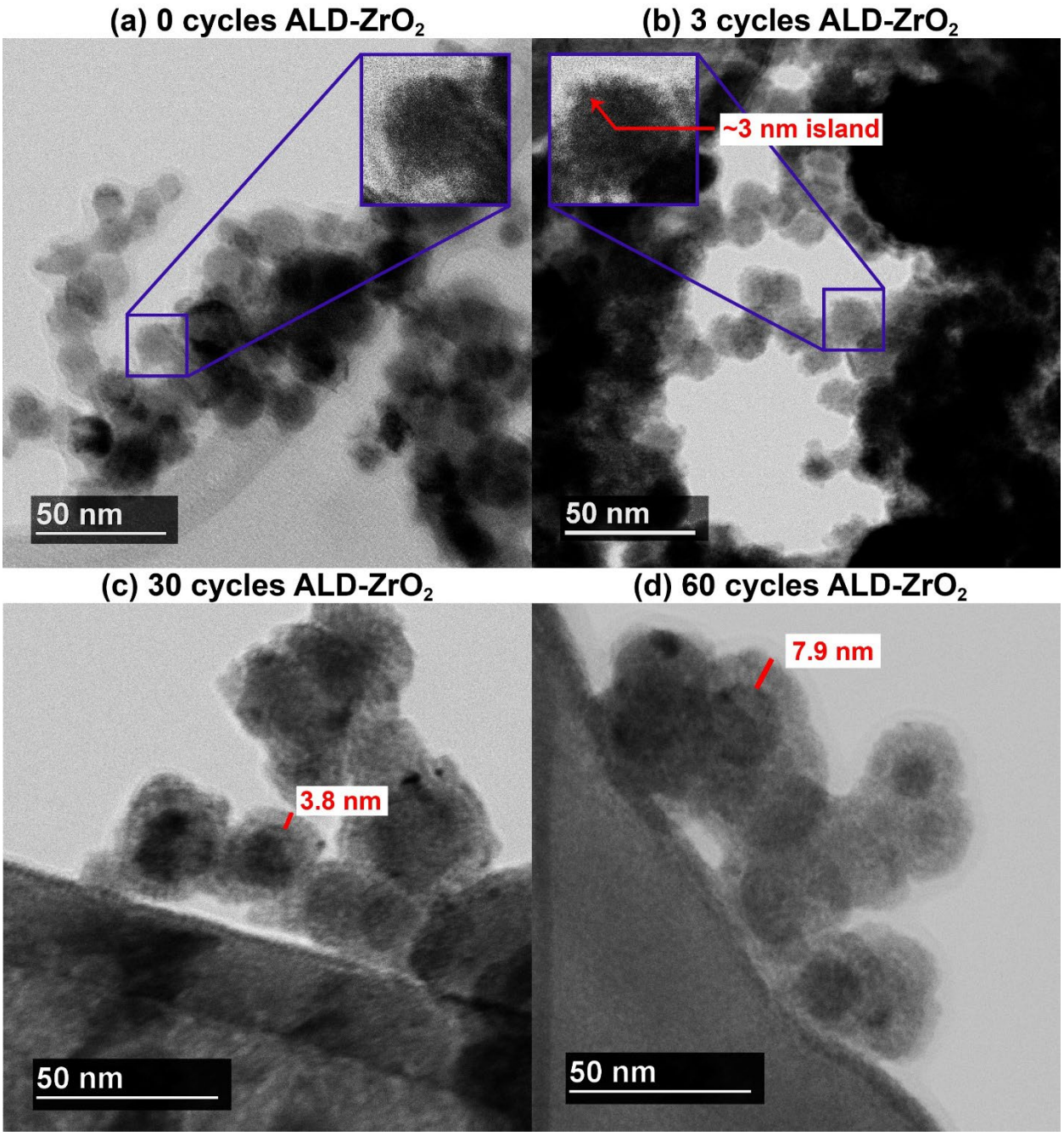

Figure 4.5 STEM images of SSC powders, with (a) 0, (b) 3, (c) 30, and (d) 60 cycles of ALD-ZrO_2 with superimposed measurements of representative coating thicknesses. Sub-monolayer growth is visible in (b) transitioning to a layer-by-layer growth-per-cycle at higher cycle numbers.

Figure 4.6 shows a fracture cross-sectional SEM image and EDS of the electrode region used for compositional mapping, including an ~20 μm porous LSM current collector, an ~40 μm

thick SSC–GDC layer, and a portion of the GDC electrolyte. The microstructure is similar to that reported previously.[18] This electrode had been coated with an unusually high number of ALD-ZrO_2 cycles, 300, to improve the Zr EDS signal. The SEM-EDS compositional depth profile (Figure 4.6(a) shows the EDS signal intensities of Zr and other key elements versus depth perpendicular to the cell layers, generated by averaging intensities across the region shown in (b). The Co, Ce, and La signals provide clear indications of where SSC, GDC, and LSM are present, respectively. The Zr signal is highest in the outer LSM layer, falling off rapidly within the first ~20 μm of the SSC–GDC layer and approaching a minimum deeper into the electrode. The rise in intensity once the GDC electrolyte is reached is attributed to the higher EDS background from dense surfaces.

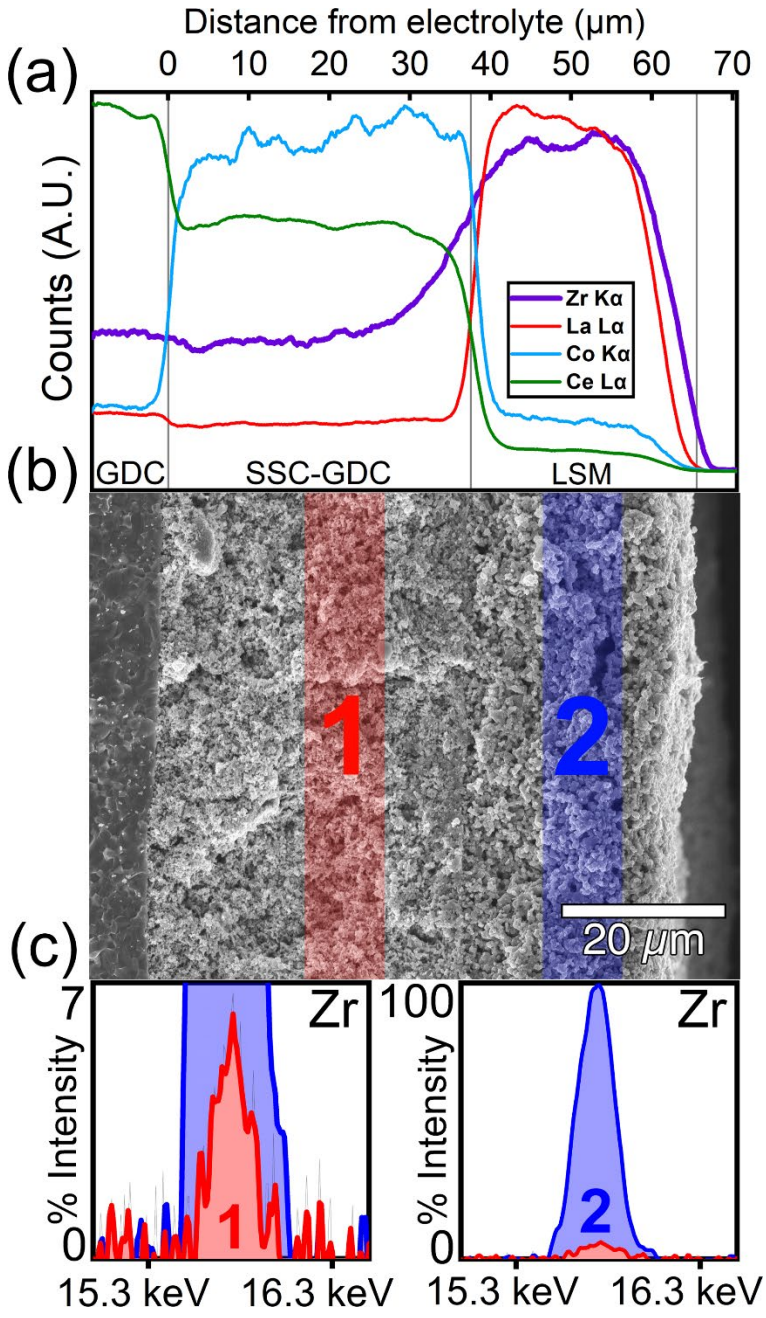

Figure 4.6 (a) EDS line-scans of an SSC–GDC cathode coated with 300 cycles of ALD-ZrO_2. The Zr Kα signal is significant near the surface, within the microstructurally less complex LSM current collector, and rapidly diminishes over a ~20 μm depth as LSM transitions into the narrower pores of SSC–GDC. (b) An SEM micrograph of the three-layer region from which the line-scans in (a) were collected. (c) A comparison of the Zr Kα peaks taken in the near-surface (LSM) region and within the active region of the tested electrode (labeled "2" and "1" in (b), respectively).

The decrease in EDS intensity with increasing depth suggests a decrease in ZrO_2 layer thickness. In order to quantify this, EDS spectra were compared in the near surface region (labeled "2" in Figure 4.6(b)) and a region within the SSC–GDC corresponding to the active region of the 20 μm thick tested electrodes (labeled "1"). To obtain accurate values, the integrated intensities of the Zr EDS peaks in Figure 4.6(c) were used, and a ratio of the intensities calculated. The thickness in region 1 was estimated to be ~7% the thickness of region 2. Thus, the average ZrO_2 thickness in the active region of the tested cells was ~0.3 nm for 30 cycles and ~0.5 nm for 60 cycles.

When a modified process in which longer precursor exposure durations were used (5s), the results again showed a steep drop-off with no discernible improvement in deposition despite the 33x longer exposure time, indicating diffusion was not the limiting step, shown in Figure 4.7. However, halving the deposition temperature seemed to modestly improve the results as shown in the following Figure 4.8.

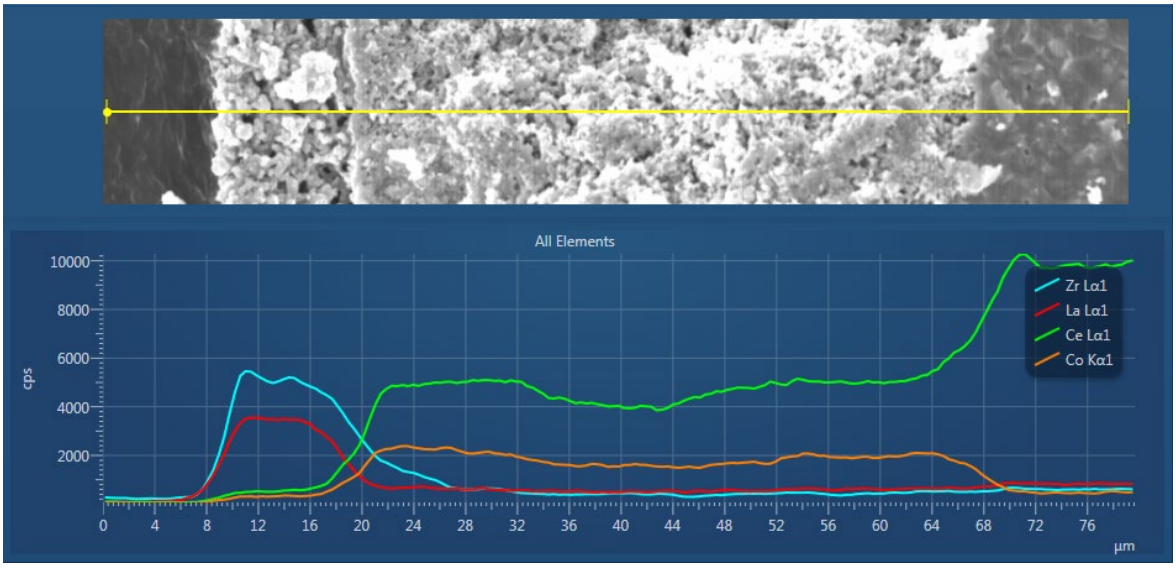

Figure 4.7 Zr counts (teal line) into an LSM-current collector then SSC-GDC system with 5 s precursor exposure times with no noticeable improvement rendered, 240°C deposition.

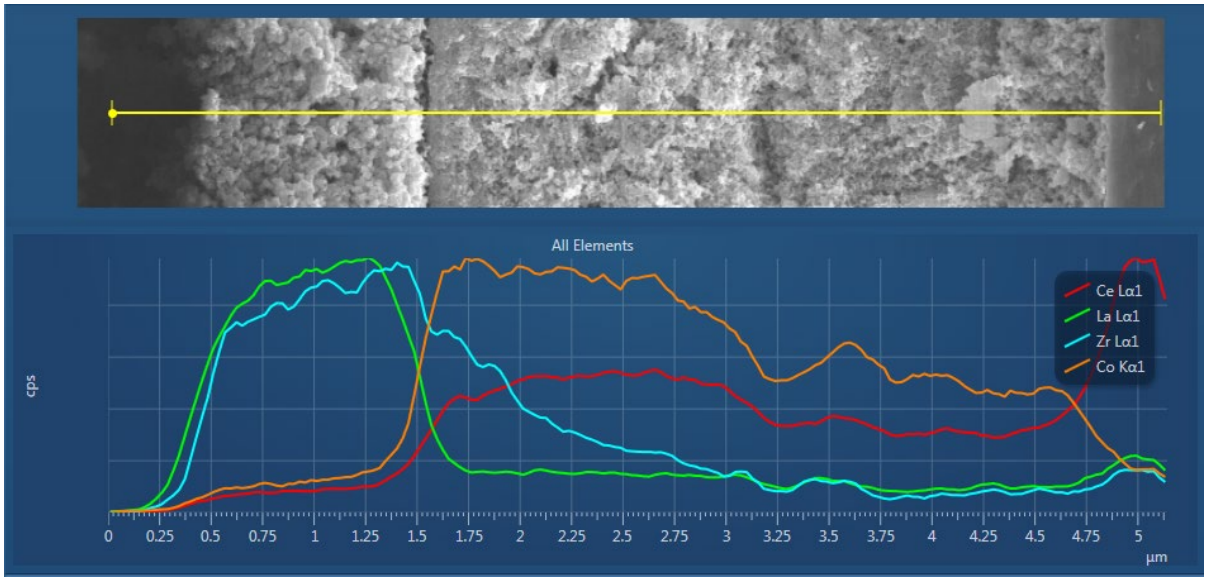

Figure 4.8 Zr counts (teal line) into an LSM-current collector then SSC-GDC system with 5 s precursor exposure time at 120°C deposition temperature.

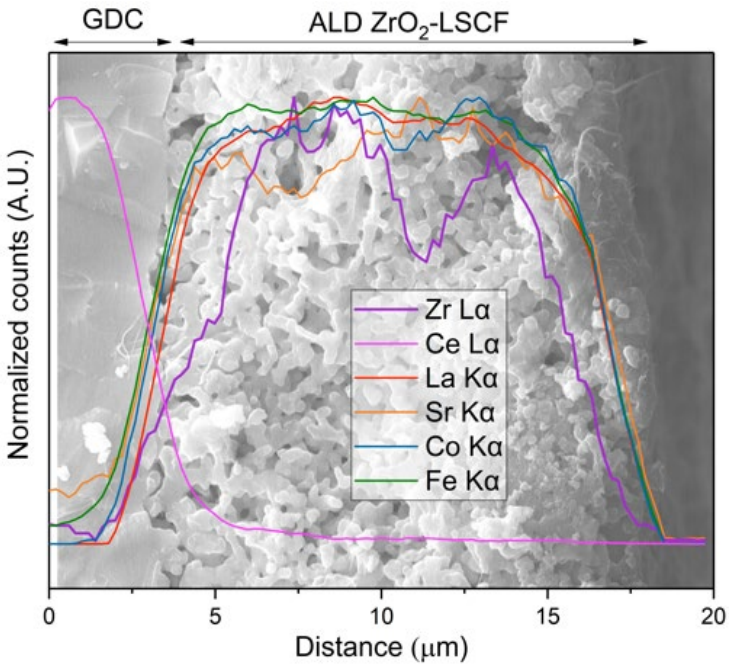

Figure 4.9 SEM and EDS line-scan for an LSCF electrode with 50 cycles of deposition and 5 s pulse lengths, showing a conformal coating achieved.

In a similar EDS map for the LSCF coated cells, the Zr signal is much more conformal with the other constituent elements (Figure 4.9). This deposition used pulses of 5 second length and 50 cycles, and the microstructure of the LSCF is comparatively much coarser, and does not include an LSM current collector.

4.3.3 SSC-ZrO_2 stability

To assess the role of Sr surface segregation in SSC, ICP measurements were carried out. Separate SSC powder samples were annealed at 750°C for varying times and the amount of surface strontium was measured. Sr-containing species including SrO, $SrCO_3$, and/or $Sr(OH)_2$ dissolve in ultrapure water that can be analyzed to determine the amount of segregated Sr.[36, 89] As shown in Figure 4.10, the Sr amount was highest in the pristine state, dropped by a factor of 2 after a 10 h anneal, and then remained approximately constant at longer times. Note that the high initial Sr content was likely associated with the $SrCO_3$ phase present in this powder (see the XRD data below), which may actually be under-estimated due to the solubility limit of 11 ppm in water.[90] In any case, there is no evidence of an increase in Sr segregation with time, as observed for other perovskite electrodes such as LSCF.[36]

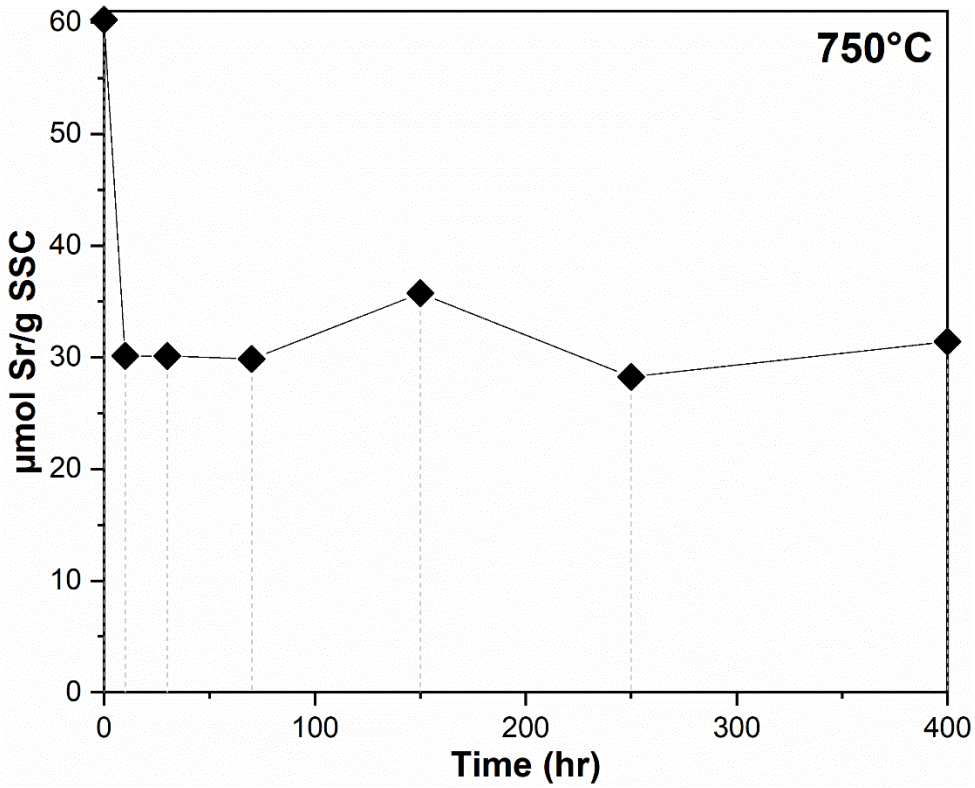

Figure 4.10 Water-soluble surface strontium in SSC powder annealed for varying times at 750°C. The ionic amount of Sr is normalized by the mass of SSC used for measurement. At annealing times 10 hours and beyond, the Sr concentration does not evolve over time, indicating a relative robustness of SSC against cation surface migration.

XRD scans of SSC powder and ALD-coated SSC powder before and after annealing are displayed in Figure 4.11. The uncoated powder Figure 4.11(a) shows a major SSC and minor $SrCO_3$ phase (the latter is eliminated upon heating to 750°C in air for 10 h, converting to surface SrO or incorporating into the SSC). Upon coating with 7 cycles of ALD-ZrO_2, Figure 4.11(b), the XRD pattern looks almost identical to the uncoated powder; the lack of ZrO_2 diffraction is likely due to low ZrO_2 crystallinity. After annealing the coated powder for 10 hours at 750°C, Figure 4.11(c), the same SSC peaks remain, the $SrCO_3$ peak is eliminated, and $SrZrO_3$, Co_3O_4, and $SmCoO_3$ peaks appear. Crystalline zirconia phases are again not detected, presumably because all zirconia has been reacted. Formation of $SrZrO_3$ due to the reaction between many common Sr-

containing perovskite electrodes and zirconia has been widely reported[91-94] with the other two species likely arising by consequence of the resulting change in perovskite stoichiometry. Thus, a portion of the SSC, determined by the amount of ZrO_2 available, is decomposed according to the reaction:

$$ZrO_2 + 2Sr_{0.5}Sm_{0.5}CoO_3 \rightarrow SrZrO_3 + \frac{1}{3}Co_3O_4 + SmCoO_3 + \frac{1}{3}O_2$$

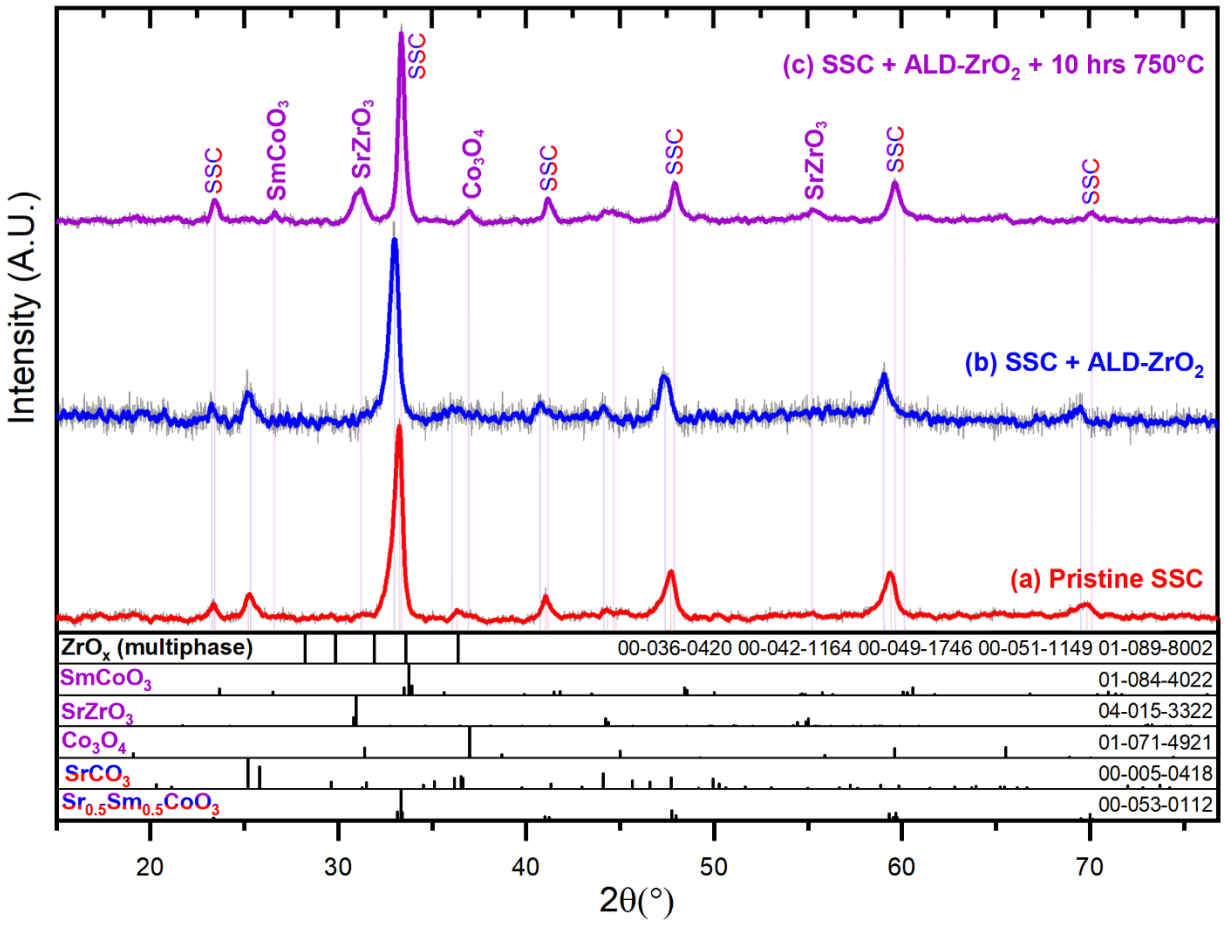

Figure 4.11 XRD spectra of (a) pristine SSC powder with an SrCO3 impurity, (b) SSC powder with ALD-ZrO_2 and without annealing, (c) ALD-ZrO_2-coated SSC after 10 hours of annealing at 750°C. Reference phase data and PDF card numbers are included in the 6 bottom panels for comparison, with zirconia being represented by the maximum intensity peaks from five major crystal systems.

In the pattern shown in Figure 4.11(c), the amount of zirconia was small relative to the amount of SSC, such that SSC remains the predominant phase and the products are minority phases. In a case where a thicker ALD-ZrO_2 coating was applied to SSC powder and annealed at a higher temperature of 800°C, a Sm-zirconate was formed instead of $SmCoO_3$ and the SSC peak was significantly reduced (Figure 4.12). The reactivity between the ALD-ZrO_2 and SSC may be heightened by the intimate contact between overlayer and substrate, and/or by the amorphous nature of the ZrO_2—in contrast, in an experiment where SSC and YSZ powders were mixed and heated, no XRD evidence of $SrZrO_3$ formation was found until 900°C and $SmZrO_3$ was not observed up to 1000°C.[95]

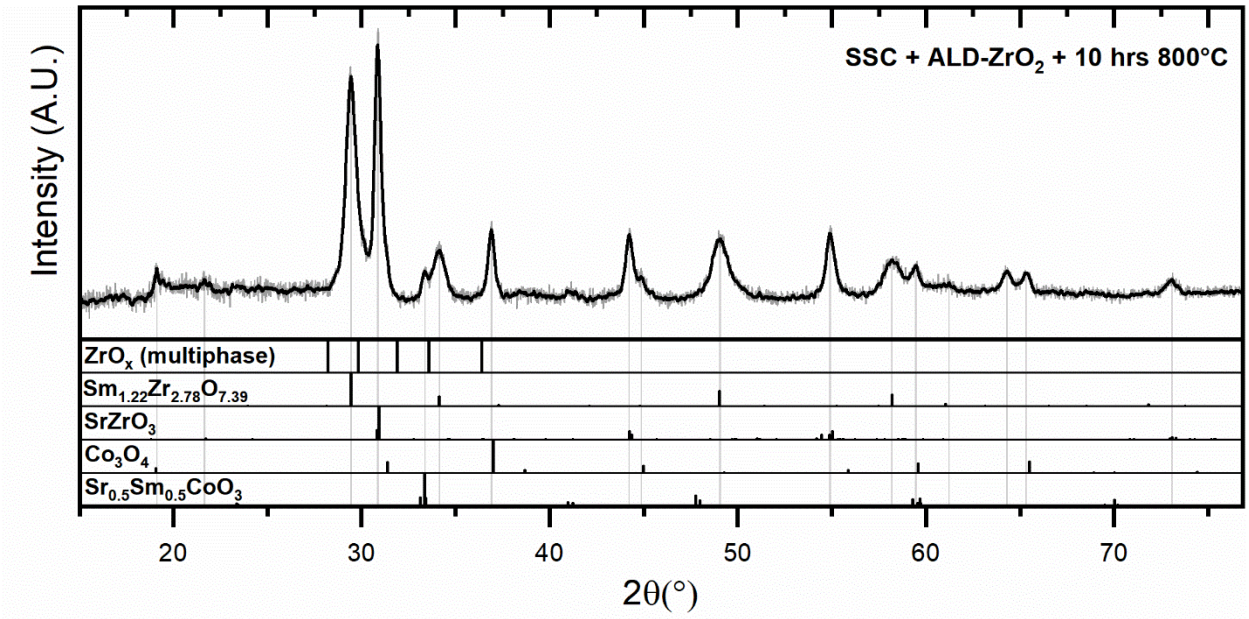

Figure 4.12 XRD result of SSC powder with ALD-ZrO_2 annealed at 800°C for 10 hours. The largest peak for SSC, ~33°, recedes into a small shoulder on a larger Sm-zirconate peak, while the other peaks of SSC greatly diminish in favor of Sr- and Sm-zirconates and Co_3O4. Evidence of crystalline zirconia phases is not found. The unbalanced reaction chemistry is: ZrO_2 + $Sr_{0.5}Sm_{0.5}CoO_3$ → $SrZrO_3$ + $Sm_{1.22}Zr_{2.78}O_{7.39}$ + Co_3O_4. The PDF card number for the Sm-zirconate is 04-021-6444; the other phases are included in main text Figure 4.11.

Similar XRD scans of pristine SSC, annealed SSC, and annealed ALD-coated SSC are superimposed for comparison in Figure 4.13. Of the three, the uncoated SSC powder shows the

broadest peaks; an ALD-coated but not annealed SSC powder yielded a nearly identical shape to the uncoated SSC and is not shown for clarity. After annealing for 10 hours at 750°C, both coated and uncoated SSC peak widths were substantially reduced, but the uncoated SSC peak was narrower. Since a smaller full-width at half-maximum indicates a larger average crystallite size, it appears that there was substantial coarsening at the annealing conditions used, and that the presence of ALD-ZrO_2 influenced the resultant crystallite size. Using the Scherrer equation,[96] the estimated initial SSC crystallite diameter of 16.3 nm increases after annealing to 35.6 nm without the coating.

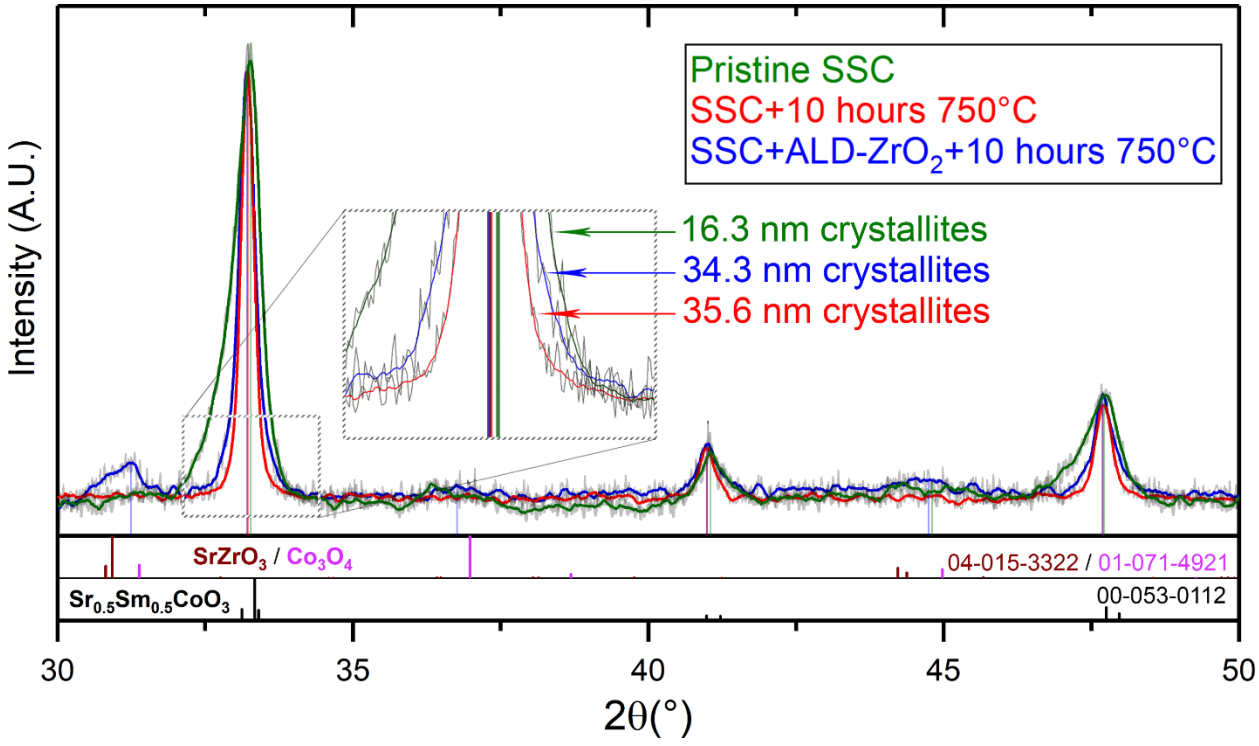

Figure 4.13 XRD peak-shape comparison from broad (pristine sample) to narrow (annealed samples) with the sample having undergone ALD treatment narrowing less than the sample without, implying a smaller average crystallite size. PDF card numbers are included.

4.4 Discussion

The polarization resistance of infiltrated SSC–GDC electrodes was observed to increase by ~30% over ~1000 h of accelerated testing at 750°C; similar degradation has been observed for

other perovskite-based electrodes with infiltrated nano-scale structure, typically explained by particle coarsening or cation surface segregation.[15, 18, 35] The present results show that ALD-ZrO_2 decreases the resistance degradation to 17–18% over 1000 h under these conditions. This result falls between prior reports on the effect of ALD-ZrO_2 – in some cases degradation is almost eliminated,[71] whereas in others there is no effect or even a negative effect.[73, 74] The present study utilizes chemical and morphological characterization of both the electrode and SSC powder to explore how ALD-ZrO_2 affects electrode characteristics. In the following, the implications of the results are discussed.

In order to understand the role of ALD-ZrO_2 on electrode performance, it is important to know the thickness of the ALD layer in the electrode active region, i.e., within ~10 μm of the electrolyte.[18, 97, 98] By scaling EDS Zr signal intensities measured versus position in the electrode (Figure 4.6), the average ZrO_2 thickness in the active region was estimated to be 0.3 nm for the tested 30-cycle electrode and 0.5 nm in the 60-cycle electrode. The substantial decrease in ZrO_2 thickness with increasing depth into the electrode can be attributed to the high aspect ratio of the porous structure, ~250 based on the pore diameter of ~100 nm and length of ~25 μm. The presence of the LSM current collector presumably also increases the effective aspect ratio. The comparatively more uniform Zr content in the un-infiltrated LSM layer may have occurred because of its higher porosity and larger pore size than the SSC–GDC functional layer. Given that the present ALD recipe was not designed to provide significant penetration, such a thickness gradient in the SSC–GDC is expected.[57, 99] For example, in a study of TiO_2 nanotubes with aspect ratios of ~180, a precursor exposure time of 0.5 s, comparable to our 0.4 s, led to a decrease in coating thickness down the length of a tube, dropping off by ~35% compared to exposure times of >5 seconds.[99] However, a study of an ~250 aspect ratio Ni/YSZ electrode coated with a similar Zr

precursor to the present case showed the deposition thickness quickly drop to 20% of the surface thickness at a depth of 25 μm, even with pulse times of 10 s; at depths >30 μm, the ZrO_2 was not detected.[57]

The active region ZrO_2 thickness is similar to the theoretical monolayer ZrO_2 thickness (0.327 nm thick).[88] Such thin ALD layers tend to show a discontinuous island structure, e.g., that of the 3-cycle ALD coating in Figure 4.5(b), rather than layer growth.[85-87] This may partially explain the good electrochemical performance of ALD-coated electrodes, *i.e.*, the coating did not substantially cover active sites on the SSC surface. The relatively low ZrO_2 layer thickness is also important because the present results show that ZrO_2 readily reacts with SSC, forming $SrZrO_3$ after 10 hours at 750°C (Figure 4.11) and $SmZrO_3$ at 800°C. Given the present active-region ZrO_2 thicknesses of ∼0.3 nm (30 cycles) or ∼0.5 nm (60 cycles), only ∼6% (or ∼10% for 60 cycles) of the SSC would be reacted. Larger thicknesses would presumably consume and/or block a large enough fraction of the SSC to significantly degrade performance (e.g., a thickness of 2.7 nm would be enough to entirely react all SSC present).

These results suggest the following interpretation of the life test data in Figure 4.1. The initial decrease in R_P may result from the zirconate-forming reaction uncovering more active SSC sites. Once all ZrO_2 is reacted, the stable zirconate particles covering SSC surfaces may provide a barrier to SSC coarsening, as suggested by the more stable R_P (Figure 4.2) and reduced SSC particle coarsening (Figure 4.13). In contrast, on the LSCF electrode which is absent any infiltrated, nanoscale features, the coating is both much more uniform (Figure 4.9) and deleterious to overall performance (Figure 4.4).

While $SrZrO_3$ is known to have a low conductivity and therefore is not expected to promote electrochemical activity, the other observed reaction products, $SmCoO_3$ and Co_3O_4, may

contribute to performance and stability; for example, there is evidence that infiltrated Co_3O_4 improves the initial polarization resistance in similar cathodes.[76, 100] It could also be suggested that the stability improvement results from ZrO_2 scavenging excess surface Sr on SSC; however, Sr segregation does not appear to be an important effect in SSC (Figure 4.10). It is however a very important degradation mode in LSCF, but here improvement is not seen (Figure 4.4).[36]

Finally, note that the degradation rates quoted here are relatively large because the life tests were designed to accelerate degradation by using a temperature higher than that expected for cell operation, ~600°C. In a prior study of the infiltrated SSC–GDC electrode system, accelerated test data was extrapolated to lower temperatures using a combined electrochemical and coarsening model, whereby 1000 h at 750°C corresponded to approximately 50 000 h at 600°C.[18] The results suggest that the R_P of the present SSC–GDC electrodes with 50 nm SSC and Zr-overlayers would increase by ~20% over 50,000 hat a temperature of 600°C, relative to ~30% for the uncoated electrode. Thus the ALD-induced stability improvement demonstrated here could provide a useful reduction in degradation.

4.5 Conclusions

The present results show that ALD–ZrO_2 improves the stability of infiltrated $Sr_{0.5}Sm_{0.5}CoO_{3-\delta}$–GDC electrodes but not bulk $La_{0.6}Sr_{0.4}Co_{0.2}Fe_{0.8}O_{3-\delta}$ electrodes. The tentative explanation for the ALD effect is that coarsening of the nano-scale infiltrated SSC is suppressed. We propose that a non-continuous $SrZrO_3$ layer forms atop a network of nanostructured SSC shortly after initial heating of the ZrO_2-coated electrode to operating temperature. Our results also indicate that the benefit of the $SrZrO_3$ was in the suppression of microstructural coarsening. Another likely degradation mechanism characteristic of this class of electrode, Sr segregation, was

not found to be significant for SSC particles, given the lack of evolving Sr concentration detected in samples via ICP-OES.

The results suggest that the ALD-ZrO_2 thickness in the electrode's active region needs to be chosen correctly; if the ZrO_2 amount is too large, a significant portion of the SSC will be consumed in the reaction and/or the SSC surface may be mostly covered. Since the resulting $SrZrO_3$ phase has poor conductivity and electrochemical activity, electrode performance will be severely compromised. On the other hand, too thin of a layer would presumably lack sufficient ability to suppress coarsening. The present case of 30- and 60-cycle ZrO_2 deposition, with average ZrO_2 thickness of ∼0.3 nm and ∼0.5 nm in the electrochemically active region, appears to be a reasonable amount because only ∼6–10% of the SSC is consumed. Similar results are expected for other MIEC materials, most of which react with ZrO_2.

The importance of ALD thickness and the difficulty of controlling and measuring the thickness may help explain the wide variations in reported results for ALD-ZrO_2 in MIEC electrodes. Obtaining the desired thickness is especially challenging because of the tendency for the ALD thickness to decrease with increasing depth into porous electrodes. In future work, a more uniform and well-controlled ZrO_2 thickness distribution with the TDMAZ precursor can presumably be achieved by increasing the exposure cycle time and lowering the reactor temperature, e.g., to 200°C.[88] It could also be helpful to reduce the thickness of the electrode and current collector to the extent possible without compromising electrode performance.

5 Atomic Layer Deposition of Alumina for Surface Area Determination of Solid Oxide Electrodes

5.1 Abstract

Conventional surface area determination techniques are inadequate for calculating the surface areas of porous solids with total measurable surface areas less than ~1 m^2 but with nanometer scale feature sizes. Current state-of-the-art solid oxide fuel cell electrodes are one example whereby accurate contextualization of electrochemical performance requires knowing system surface area, and which the two predominant classes of techniques, tomography and gas adsorption theory, neglect, either by lacking resolution or by requiring prohibitive amounts of total absolute surface area. Presented here is a method for the accurate determination of surface areas on the order of 1-1000 cm^2 with precision ±0.3 cm^2 utilizing atomic layer deposition (ALD) of commonly available trimethylaluminum (TMA) and water vapor to conformally deposit alumina over microstructurally complex internal features. The volume of alumina can then be quantified using plasma spectroscopy methods and converted to an area after dividing by the several nm-thickness of the ALD layer. As a model system, $(La_{0.8}Sr_{0.2})_{0.98}MnO_{3-\delta}$ / $Ce_{0.9}Gd_{0.1}O_{1.95}$ (LSM/GDC) scaffolds of ~2.6 m^2/g were measured under the new technique and compared against the BET method, and remarkably comparable results were obtained but with ~1000 times less material needed for the experiment. Under the modest ALD reactor soak times used (~10 s), the precursor penetration depth was found to be ~50 μm, exceeding the requirement for SOFC functional layers. To demonstrate the technique's capabilities further, two small studies were undertaken. For the first, the LSM/GDC scaffolds were infiltrated with PrO_x nanoparticles of ~50 nm and the increase in surface area (+ ~25%). After annealing for 1000 hours at 700°C the surface area was found to have reverted to non-infiltrated levels. For the second, exsolvable system

$Sr(Ti,Fe,Ni)O_{3-\delta}$ was measured before and after forming (Ni,Fe) surface decorations, and the increase in surface area was calculated versus three different compositions. The technique, due to its ease versus other surface area determination methods and its pairing with an established analytical chemistry method, enables a useful combined chemical/morphological approach to characterization of next-generation solid oxide electrode performance, and may find other uses in the broad field of heterogeneous catalysis.

5.2 Introduction

Surface area determination is a characterization goal broadly sought in the field of heterogeneous catalysis to quantify activity and performance on a normalized basis. For high specific surface area materials (>100 m^2/g) like zeolites and metal-organic frameworks, this need is largely met by the ISO-standard Brunauer, Emmett and Teller (BET) methodology in which surface area is calculated from a linear portion of a gas isotherm physisorption experiment. However, for solid oxide fuel cell (SOFC) materials, which are sintered ceramic oxides, typical specific surface areas are on the order of 1-10 m^2/g with typical weights on the order of 10 mg per sample, resulting in absolute surface areas below 1 m^2, which is the practical lower limit for conventional BET applicability with lower vapor pressure krypton isotherms (for example, in the Micromeritics 3Flex analyzer with 12mm tubes, >1.55 m^2 is needed for <1% uncertainty and >0.3 m^2 is needed for <5% uncertainty).[101] And although BET can work with non-powder samples (e.g., sintered electrodes), the dimensions of the tube usually constrain the sample to be no larger than ~1 cm in width.

For SOCs, electrochemical performance is normalized by the easily obtained projected surface area of the catalyst, for example via power density (W/cm^2) for full cells or area specific resistance ($\Omega\ cm^2$) for individual electrode processes. This is much more practical for systems-

level comparisons of electrodes, given thickness is much smaller than length and width of a cell stack component. However, from a materials discovery perspective, the projected-area-normalized performance of a material is obfuscated by the microstructural details arising from the specific processing route. This is not insignificant as the same material processed by different research groups can have vastly different performance. Performance that is instead normalized by internal surface area can give rise to data more aligned with fundamental materials properties, such as surface exchange and diffusion coefficients.

Full explorations of the structure-property-performance relationship have been conducted for a wide variety of SOC materials but usually involves resource-intensive tomographical methods, such as focused ion beam (FIB)-assisted scanning electron microscopy (SEM) or synchrotron X-ray computed nanotomography (nano-CT). The result of either is a 3D-reconstruction stitched from interpolated 2D images with extensive microstructural information, but both cannot resolve the smallest feature sizes characteristic of next-generation solid oxide cells incorporating infiltrations or exsolved nanoparticles in their microstructural measurements. FIB-SEM offers the better voxel size of ~30 nm, which requires particle sizes to be ~450 nm for error to be <5%. This poses a problem for nanostructured hierarchical systems; for example particles infiltrated on a scaffold can be <50 nm and some metal exsolution systems give rise to particles as small as 5 nm.[102] Another technique, mercury porosimetry, can allow approximate surface area from a distribution of cylindrical pore sizes based on the pressure needed to infiltrate such pores; this morphology, however, is not reflective of the nanoparticle-decorated surfaces of the solid oxide electrodes under consideration.

A conceptually similar idea to using monolayer formation via nitrogen physisorption to extract surface area, as in BET, is using self-limiting chemisorption of the chemical precursors

used in ALD. With a known deposition rate (growth-per-cycle or GPC), *n* number of cycles results in a known thickness. Further, the volume of species can be ascertained either gravimetrically (via the known density of the ALD layer) or, more sensitively, from digesting the alumina overcoat and measuring concentration via inductively coupled plasma emission spectroscopy (ICP-OES). The known volume can be divided by the known thickness to result in an absolute surface area. Finally, the result can be normalized to a specific surface area by dividing by the known total mass or volume. The advantages and limitations of such a technique are explored in this paper.

Previously, ALD combined with plasma spectroscopy has been used on materials of known surface area to estimate the effectiveness of the ALD process in comprehensively covering the sample—our methodology sees this process in reverse with the prototypical ALD precursor, trimethylaluminum (TMA). The TMA-water process is nearly ideal in that both precursors are stable enough to avoid random thermal decomposition but reactive enough with each other, they are of high vapor pressure, and their reaction product, methane, is inert with either of them at deposition conditions.[55] ALD TMA has been used to coat high aspect ratio anodic TiO_2 nanotubes with aspect ratios of ~180 with precursor exposure times of 4-5 seconds to ensure enough diffusion time is available. This aspect ratio is similar to SOFC electrodes of pore diameters >100 nm and <20 μm thick, resulting in aspect ratios <200.[65] Due to the robustness of TMA, exposure times even in excess of 10 s still result in stable growth rates. Therefore, the TMA/water process is ideal enough that results should be reproducible with many kinds of reactors and slight process variations.[99]

Similar to the protocol outlined here, ALD TiO_2 has been used in conjunction with dye adsorption and UV-vis to estimate surface areas as is common in the dye-sensitized solar cell community, but the measurement is less direct on account of the dye intermediary and involves a

prohibitive 500°C annealing step (enough to cause a reaction with many substrates) to favor a particular TiO_2 crystallographic plane.[103] In our methodology, a fast, direct 200°C process is demonstrated with no further processing except for acid digestion before measurement. The result is a broadly applicable and accessible means for determining low absolute surface areas (~1 cm^2) of mesoporous structures (pore radius > 6 nm), including those with nanoscale features which are becoming increasingly popular in advanced catalysis.

5.3 Description of the Methodology

An overview of the steps involved in the full determination appears in Figure 5.1. First, samples are prepared for atomic layer deposition. The samples used in the mass-based determination method were weighed prior to the deposition. To coat both sides of the samples, samples were either placed in a metallic mesh bag or suspended via clip. After pumping down to low vacuum (~30 mTorr) via roughing pump, the samples were allowed to equilibrate and dry at 200°C for 10 minutes. (Note that excess water will react with organometallic precursor upon the first deposition cycle.) The ALD process used an exposure mode in which the chamber filled for 1.5 seconds via an 11 ms pulse of precursor four times (for a combined 6 seconds of exposure), then was allowed to purge for 20 seconds, then the same for the oxidant, for a total of 50 precursor/oxidant cycles. Operating in this mode, with the egress actuator of the chamber closed, allows for greater diffusion time for the precursor through porous structures.[55]

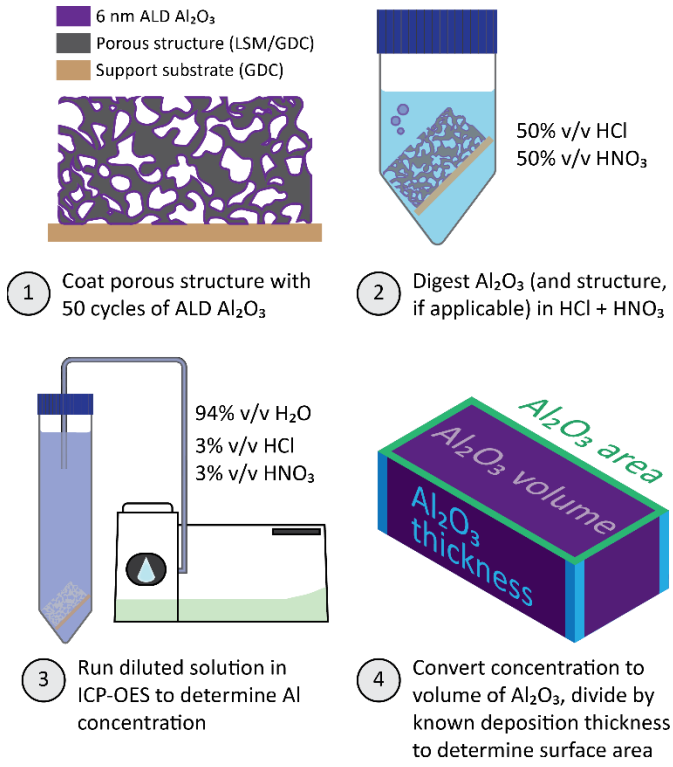

Figure 5.1 Process overview for the surface area determination technique using ALD and ICP-OES.

Next, samples were removed from the ALD chamber (and weighed if using mass-based determination). In some cases, if the contribution to the surface area from the electrolyte supports was thought to be significant, photographs were taken of the cells (adjacent a ruler) so that those areas can be later subtracted out of the total area determined for the electrodes. In the LSM/GDC samples, this contribution was ~1% and determined to be negligible, but for the lower absolute surface area STF(N) samples later, contributions were ~10% and were therefore subtracted. Samples were placed in 1:1 HCl:HNO_3 solution of 0.72 mL and left for 24 h without agitation or heat. Hydrochloric acid has been shown to be able to dissolve perovskite SOFC electrodes.[36, 65] Nitric acid is a well-known solvent for nickel and other metals, and together as aqua regia they are capable of dissolving noble metals. After 24 h, the solution was diluted to be 3%/3% HCl/HNO_3

in ultrapure water. The ceria components of the cells do not dissolve and were left in the tubes in order to prevent contamination from retrieving them.

Standards were then prepared for ICP-OES using serial dilution of a combined elemental standard from 100ppm to 0.01 ppm. The samples were run through ICP-OES in radial mode, analyzing for constituent elements as well as aluminum. Several emissions lines for each element were chosen, selecting for ones without interference from other known elements, and the instrument took measurements in triplicate; the ultimate emission line chosen was the one with the lowest standard deviation.

Data was analyzed by converting from PPM (mass basis) to mass by multiplying by the total mass of the solution in the tube (1.0207 g/mL * 12 mL = 12.2484 g), and then onto moles by dividing by the atomic weight per mole of the element. For aluminum, the volume can be obtained by dividing the mass by the density of Al_2O_3 – for an ALD process at a similar 177°C, this was found to be 3.0 g/cm^3.[59] The surface area can then be obtained by dividing the volume by the known deposition thickness. For 50 cycles, at 1.25Å/cycle,[59] this is 6.25 nm. [Note: the exact growth-per-cycle is non-uniform for the first ~20 cycles,[85] so this value is expected to overestimate the height of the ALD layer and thus underestimate the surface area. Later, an analogous BET measurement allows for a more precise tuning of 1.19 Å/cycle.] Finally, surface area can be normalized simply to a per-mass of sample basis using the weight of the other elements analyzed.

5.4 Validation

To determine that the measurement technique is sound, several outstanding questions need to be answered, concerning whether the Al_2O_3 coating fully dissolves in the modified aqua regia, whether the coating is uniform and if it is subject to diffusional limitations, and whether the data is comparable using results from BET

Because ALD processes can deviate from ideal behavior especially with high aspect ratio structures, the penetration depth of the protocol was measured.[55, 65] However, in previous studies with TMA precursor The Al signal can be tracked into the cell via cross-sectioning and SEM-EDS analysis for chemical mapping. These results are shown in Figure 5.2 for two cells—an infiltrated LSM/GDC sample with higher specific surface area and of ~15 µm thickness, and a Ni/yttria-stabilized zirconia (Ni/YSZ) composite electrode of ~300 µm thickness.

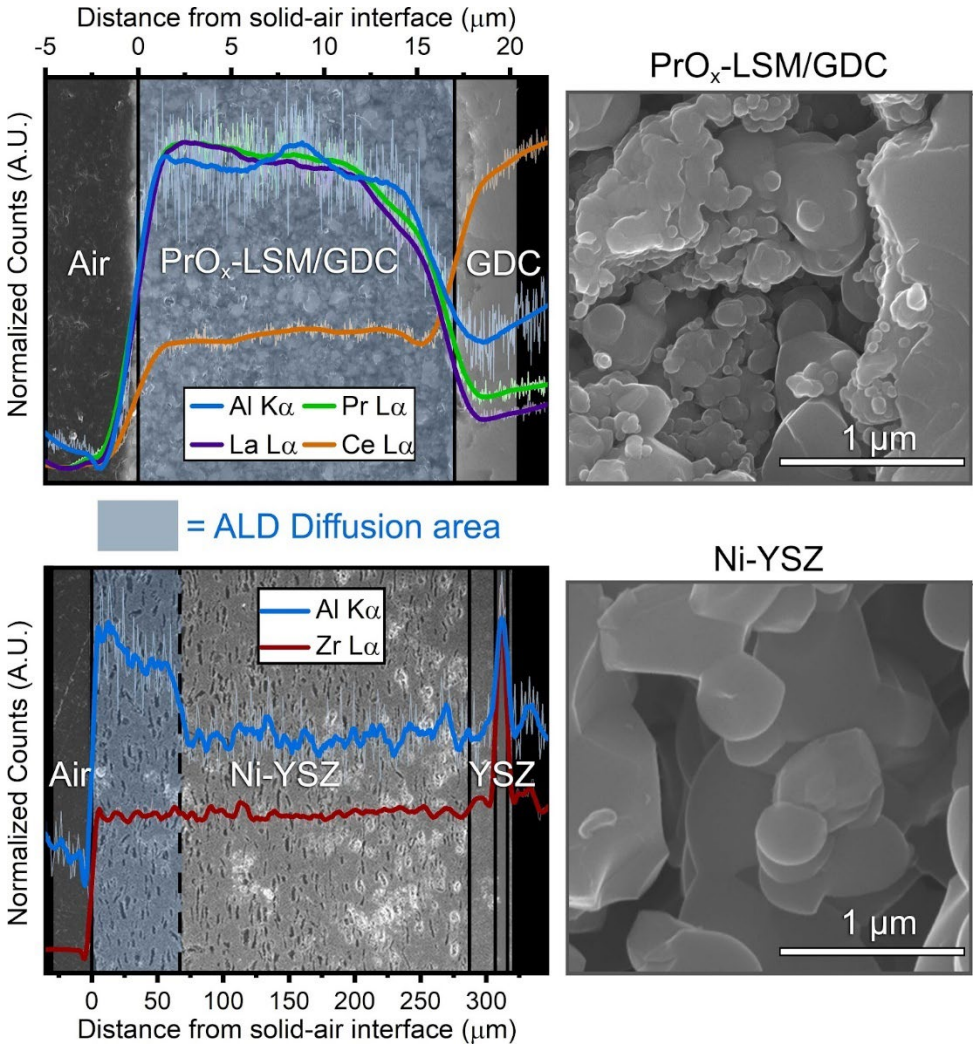

Figure 5.2 Tracking the signal of Al diffused into porous electrode scaffolds by SEM/EDS line-scan, with the top depicting an infiltrated oxygen electrode, PrOx-LSM/GDC, and the bottom a Ni/YSZ support. Fracture cross-sections are also shown.

In Figure 5.2(a), the Al signal can be seen tracking with representative elements of the scaffold, namely Pr representing the infiltrated species, La representing the LSM, and Ce representing the GDC. Here, the microstructure has 50-100 nm features, similar to advanced solid oxide cell electrodes. This system was chosen because infiltrations decrease the free volume of the electrode, therefore increasing the aspect ratio of the pores.

In Figure 5.2(c), a Ni/YSZ tape-casted support layer was selected in order to create very long aspect ratio pores. The aluminum signal falls off after about 50 μm into the scaffold. This indicates a diffusion limit was reached. A conservative estimate is that the ~10 s pulses used are sufficient for up to 50 μm depths. Given Knudsen diffusion depth is related to $t^{1/2}$, the thinner LSM/GDC scaffold should have only required 1.2 s of precursor exposure, and the much thicker Ni/YSZ would require 360 s or 6 minutes of exposure.

Next, we can benchmark the protocol against BET and via weight gain. First, the difference in sample weight before and after alumina deposition can be used to generate the mass of deposited species. The mass generated from this method and the mass from the concentration measured from ICP-OES are compared and fall very close together, except with a larger standard deviation arising from the mass-based method.

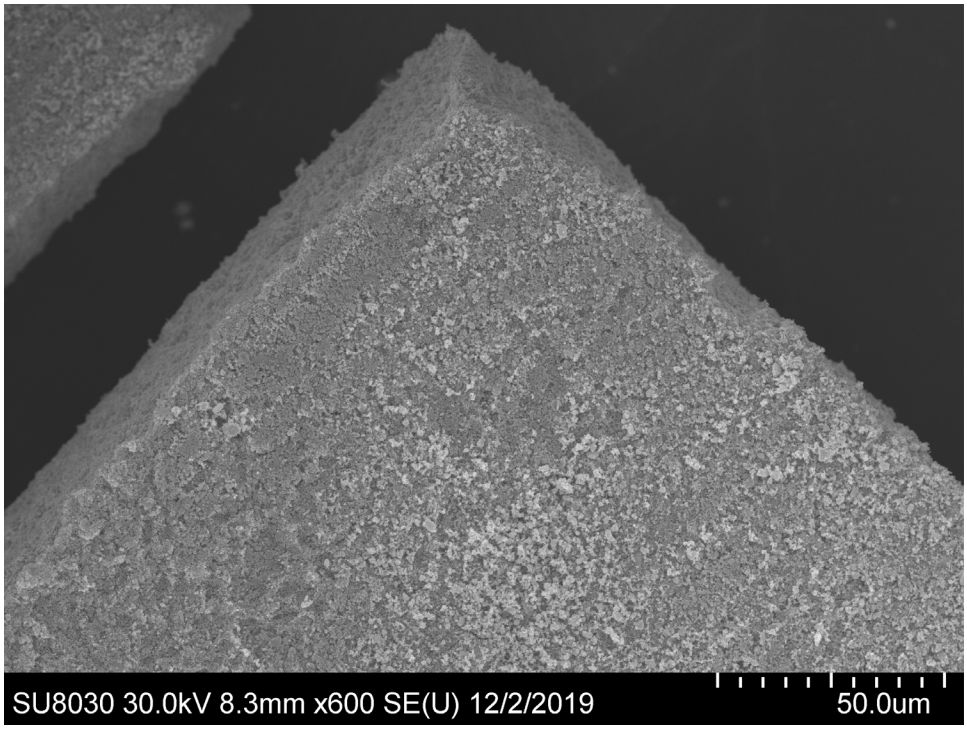

Figure 5.3 Micrograph of self-supported bulk LSM/GDC fired to create quantities large enough for BET measurement (~1 g material per measurement). The microstructure is equivalent so electrodes fired atop GDC substrates.

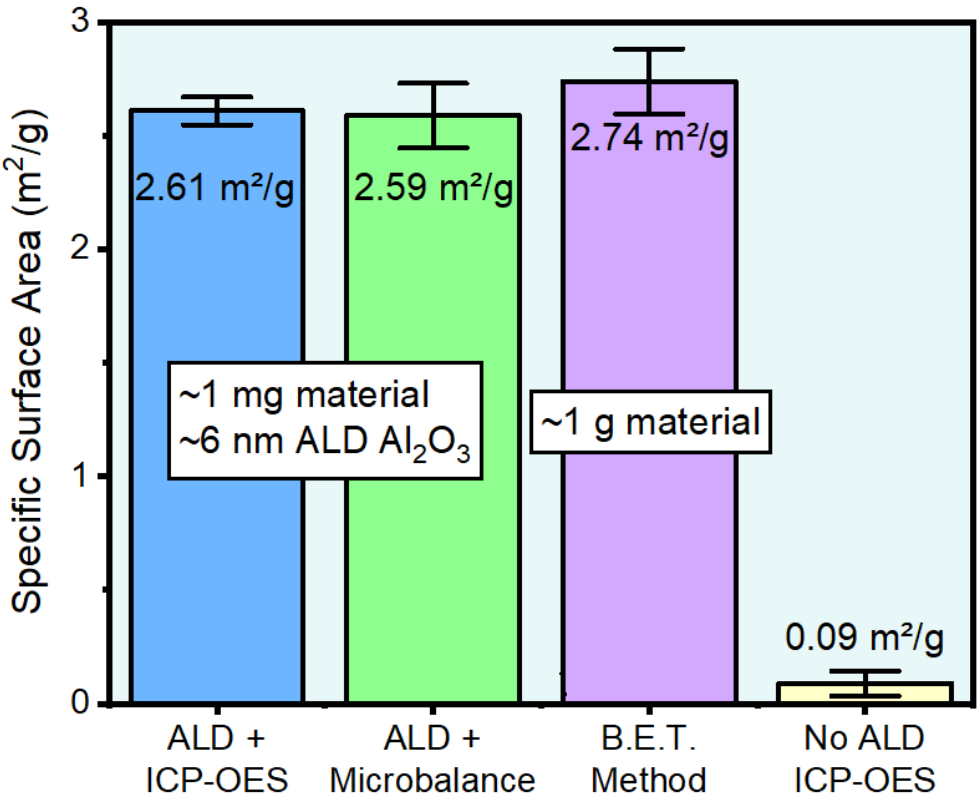

Figure 5.4 Comparison between methodologies of surface area determination, two using the ALD method (one deriving Al_2O_3 volume by ICP-OES, the other by its mass) and the last using BET theory. Also shown is the signal and error from ICP-OES on samples that were not coated with ALD-Al_2O_3.

The ALD method using ICP-OES to determine volume (and density and GPC from literature) is compared against values when using mass to derive volume. The microbalance used was a Mettler Toledo UMX2 with a sensitivity of 0.1 µg. The mass-derived volumes provide very similar values when compared to the ICP-OES-derived volumes. This is a strong indication that all the alumina is in fact dissolving in the acid matrix.

To compare against ALD, an adequately large amount of LSM/GDC ink was fired and formed a self-supported scaffold, with comparable microstructure, shown at large scale in Figure 5.3. Two samples, one 1.06 g, the other 1.03 g, were used, with expected errors of <0.77% given their absolute surface areas.[101] The resulting BET results were very comparable to those estimated

by ALD and is on average slightly lower. Assuming total veracity of the BET results, this indicates that the density and/or GPC values suggested from the ALD process are artificially high. In fact, this should be true, given the GPC from literature is at a steady-state for deposition, when in fact it's known that the first ~20 cycles of ALD Al_2O_3 produces an impeded growth rate with Volmer-Weber islands, arising from the higher interfacial energy between the deposited oxide and the substrate. This results in a GPC that is overestimated. When dividing a known volume by a thickness that is therefore too large, the surface area will be too small to compensate.

The result from BET can therefore be used to calibrate the real GPC, assuming the same density of 3.0 g/cm^3. This is 1.19 Å/cycle, or 95.2% of the 1.25 Å/cycle from the literature.

5.5 Vignettes demonstrating usage

The surface area technique, now validated and calibrated, was used on two small studies to demonstrates its usefulness in solid oxide cell development.

5.5.1 Coarsening of PrO_x Infiltrations

The initial inspiration for the technique was a lack of a facile way to determine the surface area for infiltrated electrodes. Infiltration results in nanoparticulate decorations using the modified Pechini method. The morphologies seen in Figure 5.5, are not immediately discernibly different. In fact, the morphology in (b) has 20-30% more surface area than (a), but the shape of the infiltrated particles is similar microstructurally to the low end of the microstructure for LSM-GDC. An SEM based study of coarsening would not be able to track these effects.

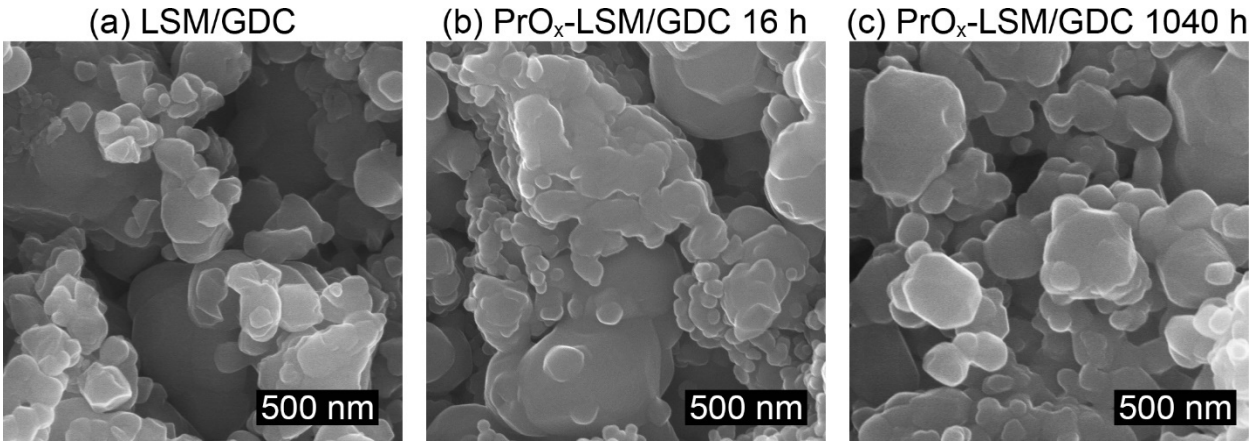

Figure 5.5 Comparison between the (a) as-fired LSM/GDC, (b) PrO_x-infiltrated LSM/GDC after 16 h at 700°C, and (c) PrO_x-infiltrated LSM/GDC after 1040 h at 700°C. Morphological differences are subtle and would be difficult to identify by sight.

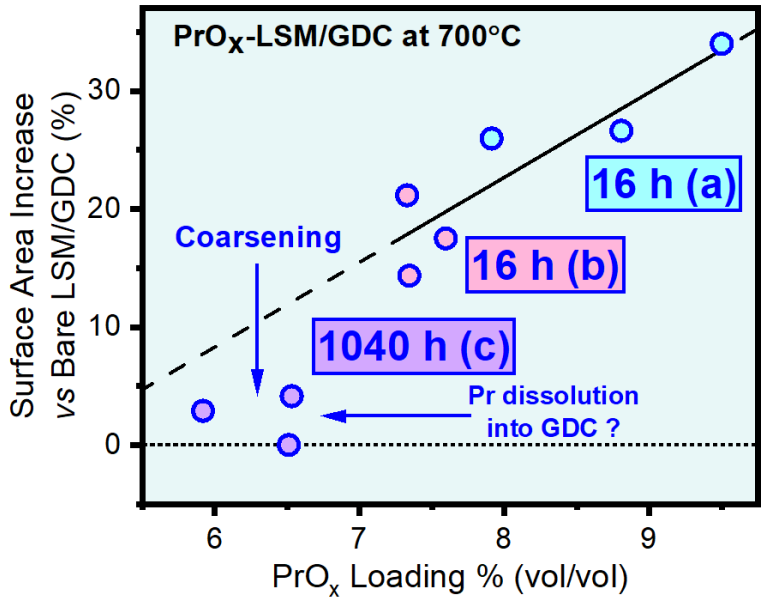

Figure 5.6 Increase in surface area relative to bare LSM-GDC as measured by the ALD surface area technique. Two samples with low ageing show a wide disparity in PrO_x loading which is linearly related to the surface area increase. After 1 kh, the surface area increase has been highly reduced by coarsening and possibly Pr-dissolution into GDC.

First, it was apparent by measuring the samples annealed for 16 h that the amount of PrO_x loaded into the cells was highly variable. Samples mark (a) and (b) showed a wide variety of Pr loaded (measured by ICP-OES). Each data point came from a different fractured piece. Only one

infiltration round was used, so stochastic processes heavily influenced where infiltration solution ended up. A third cell

5.5.2 Exsolution of Metal Particle Decorations

For the exsolution-capable systems STF and STFN, the difference in the microstructure upon exposing the electrodes to reducing atmosphere is more apparent (the following chapter goes into more depth concerning these systems and exsolution).

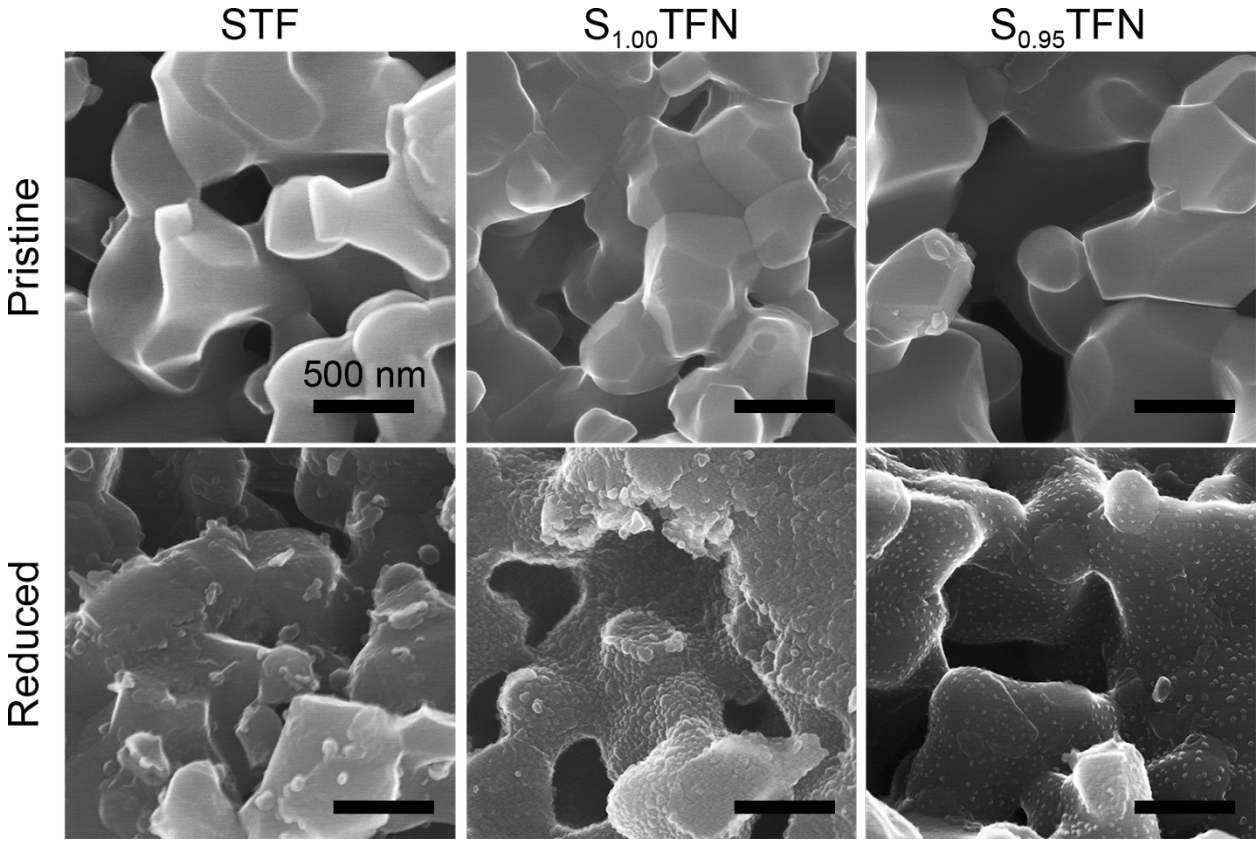

Figure 5.7 SEM-acquired microstructures of (a) STF and (b) reduced STF, (c) $S_{1.00}$TFN and (d) reduced $S_{1.00}$TFN, and (e) $S_{0.95}$TFN and (f) reduced $S_{0.95}$TFN. All scale bars 500 nm.

The largest gain in surface area comes from the stoichiometric $S_{1.00}$TFN system which seems to nucleate a crowded, packed array of particles. STF seems to nucleate larger Fe particles and has the largest absolute surface area. The exsolution in A-site deficient $S_{0.95}$TFN is the least extensive and a lower areal density of (Ni,Fe) particles is apparent.

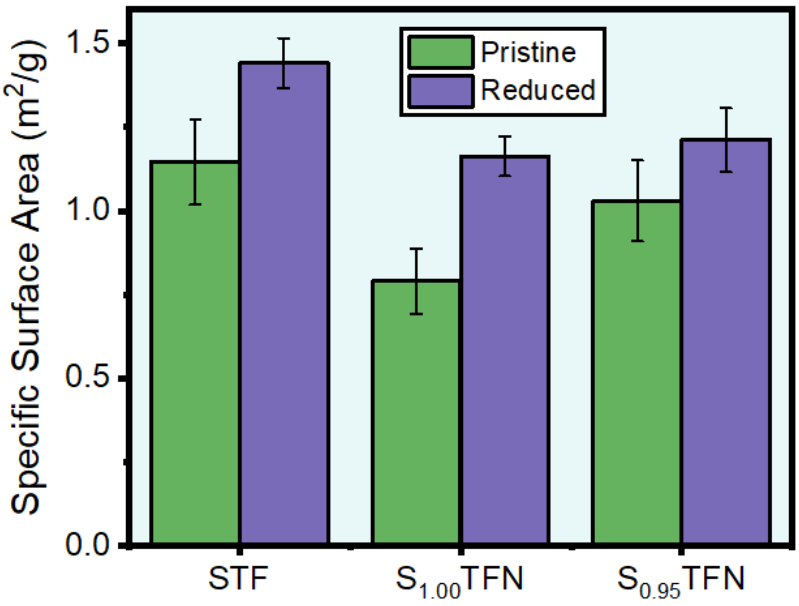

Figure 5.8 ALD-derived surface areas for STF, stoichiometric $S_{1.00}$TFN, and A-site deficient STFN ($S_{0.95}$TFN).

5.6 Conclusions

The ALD surface area method is validated and demonstrated to be able to handle the particular characterization requirements for solid oxide cell electrode development. It provides comparable results to the gold standard measurement technique, BET, but with milligram quantities of electrode material needed, rather than gram quantities. It therefore pairs well with the quantities used in standard button-cell testing of ceramic electrochemical materials. ICP-OES can be used to quantify other features of the electrodes, such as the volume loaded of an infiltrant, and comparison to un-infiltrated electrodes allows for a greater understanding of the morphological changes upon infiltration. Two vignettes were undertaken in which the technique demonstrates its usefulness in acquiring quantitative surface area information, one for next-generation oxygen electrodes utilizing infiltrated nanoscale particles, and for next-generation perovskite fuel electrodes that undergo exsolution to produce socketed nano-scale particles.

6 In-situ Exsolution and Redox Reactivation of Ni- and Ru-based Metal Alloys from Strontium Iron Titanate Perovskite Solid Oxide Fuel Electrodes

6.1 Abstract

Cermet fuel electrodes with structural and/or percolated metallic nickel are susceptible to performance degradation after oxidation, carbon deposition, and sulfur poisoning events. Redox tolerance, the ability for an electrode to maintain its electrochemical activity after a swing from a reducing fuel environment to an oxidizing air environment, and back again, is a quality that can potentially address all three of these degradation modes. Compared to cermets, perovskite anodes with in-situ generated metal particles are highly promising, redox-tolerant electrodes currently under development. They can maintain stability in both oxidizing and reducing atmospheres and have been shown to be less susceptible to coking and to be able to reactivate after poisoning via intentional redox cycling. This chapter will focus on the reduction and redox process in Ni,Fe- and Ru,Fe-doped Strontium Titanate perovskite-based systems, capable of exsolving (Ni,Fe) and (Ru,Fe) alloys, respectively. A-site deficient and stoichiometric $Sr_{0.95}(Ti_{0.3}Fe_{0.63}Ni_{0.07})O_{3-\delta}$ ($S_{0.95}$TFN) and $Sr(Ti_{0.3}Fe_{0.63}Ni_{0.07})O_{3-\delta}$ ($S_{1.00}$TFN), as well as stoichiometric $Sr(Ti_{0.3}Fe_{0.7})O_{3-\delta}$ (STF) are degraded in humidified hydrogen and redox cycled 4 times over the course of a 1,000 hour life-test. In-situ XRD reveals Ruddlesden-Popper phase formation concomitant with continuous Fe reduction, and redox cycles lead to an amount of regenerable performance. Ultimately, however, significant amounts of Ni are unable to be re-dissolved into the perovskite phase and subsequent exsolution rounds lead to lower areal density of particles owing to shifted perovskite composition and nucleation/growth kinetics. In addendum, A-site deficient $Sr_{0.935}(Ti_{0.28}Fe_{0.655}Ru_{0.065})O_{3-\delta}$ (STFR) is redox-cycled after exposure to ethanol fuel and is compared against Ni/YSZ which cokes and degrades after oxidation.

6.2 Introduction

Exsolution of reducible cations from perovskite materials has been a major step forward in the realization of perovskite-based anodes for solid oxide fuel cells. Perovskite fuel electrodes have been studied from the early 2000s as alternatives to conventional Ni/YSZ systems due to their redox stability and coking resistance. While even then the exsolution phenomenon was known to occur, it was looked on with "suspicion" as merely a harbinger of decomposition.[104] While perovskite anodes continue to suffer from <10 S/cm conductivities, their relatively high polarization resistances vs. Ni cermets have come down considerably upon introduction of exsolved catalysts, in some cases also even leading to an increase in bulk conductivity.[27, 105]

Although single metal exsolved systems are more commonly studied, binary and even ternary exsolved systems have also received considerable attention.[105] Some of this is likely by happenstance; the most common metal to alloy is Fe, and Fe happens to be a very common aliovalent B-site dopant in perovskite systems already. However, reasons to deliberately study alloy systems are that they allow for a greater design space for catalyst activity towards fuel oxidation. While Ni is widely accepted as the best catalyst for the hydrogen oxidation reaction in SOFCs, and has been shown to be the peak of volcano-type plots relating its anodic conductivity and its oxidation energy,[106] alloys could be more desirable in the case of CO_2 and steam electrolysis as well as for CO and CH_4 conversion.[107] Bimetallic Ni-Fe has been shown to be superior to pure Ni at ~10% Fe in dry methane,[108] and Ni-Fe compositions have demonstrated coking resistance versus pure Ni.[109] (Coking resistance, however, is expected to be formidable across all perovskite anodes due to the abundance of nearby oxygen vacancies for the stable conversion of CO to CO_2).

As mentioned, the electronic conductivity of perovskite anodes remains low. Although metal particles may act as brief n-type short-circuits for already n-type conducting perovskites, as

many are in low pO_2s,[26] the percolation threshold is inherently not met so conductivity resembles that of non-exsolved perovskites. While some literature has reported >10 S/cm conductivity, all such cases have been in dry hydrogen environments; upon operation, water formation would be expected to increase the pO_2 considerably, so more studies with fuel cell performance in mind should introduce at least 3% steam by use of a simple room-temperature bubbler. Additionally, bulk transformation with exsolution systems has been known to occur (such as perovskite to Ruddlesden-Popper), and it is relatively unknown what effect the perovskite to layered perovskite transformation has on conductivity. For example, the system $La_{0.6}Sr_{0.4}Co_{0.2}Fe_{0.8}O_3$ transforms to R-P phase $La_{1.2}Sr_{0.8}Co_{0.12}Fe_{0.88}O_4$ upon exsolution of (Co,Fe) nanoparticles in 10% H_2/N_2 gas mixture at 800°C,[110] the system $(Pr_{0.5}Sr_{0.5})_{0.9}Fe_{0.9}Ru_{0.1}O_{3-\delta}$ transforms to R-P $PrSrFe_{1-x}Ru_xO_{4+\delta}$ upon exsolution of (Fe, Ru) in 800°C H_2,[111] and the system $Pr_{0.32}Sr_{0.48}Ni_{0.2}Fe_{0.8}O_{3-\delta}$ transforms to $Pr_{0.8}Sr_{1.2}(Ni,Fe)O_{4-\delta}$ upon exsolution of (Ni,Fe) in H_2 at 800°C.[112]

In the above examples, the electrodes were subjected to "pre-reduction" conditions in pure hydrogen or hydrogen/inert mixtures and at elevated temperature to intentionally drive the formation of exsolution and R-P phase formation. However, many examples of very similar systems, sometimes with or without pre-reduction, report exsolution without perovskite phase transformation, often based on ex-situ characterization.[22, 113, 114] It should be noted that, given pO_2 is used as a lever for in-situ synthesis, the characterization of the post-reduced alloys may be sensitive to ramp-down conditions. Highly reducible elements like Ni and Ru may withstand the decrease in temperature and increase in pO_2, remaining metallic, but less reducible elements like Co and Fe may oxidize, either as their own native oxides or potentially back into the perovskite matrix. Alloy composition is a desirable parameter to characterize, and because quenching is not an option, ex-situ characterization is blind to what reorganization may occur in the transit down to

room temperature and up to 0.21 pO_2. Therefore, a greater emphasis should be placed on results collected at relevant temperature and atmosphere, such as in-situ XRD, NAP-XAS and XPS, TGA, and of course electrochemical methods such as EIS and linear sweep voltammetry.

In this study, we focus on the exsolution and redox behavior of STFN, formerly identified to be a promising exsolvable anode material. Here, stoichiometric starting perovskite $Sr(Ti_{0.3}Fe_{0.63}Ni_{0.07})O_{3-\delta}$ ($S_{1.00}$TFN), A-site deficient $Sr_{0.95}(Ti_{0.3}Fe_{0.63}Ni_{0.07})O_{3-\delta}$ ($S_{0.95}$TFN), as well as stoichiometric $Sr(Ti_{0.3}Fe_{0.7})O_{3-\delta}$ (STF) are studied to compare the effects of A-site deficiency and Ni-doping. Previous studies utilized pre-reduction, which resulted in greater stability, but at the cost of its higher initial performance without pre-reduction.[22, 29] Here, reduction is done at the operating temperature of 700°C to study the cause of the initial marked drop-off in performance seen without pre-reduction. Electrochemical characterization is performed in the symmetric fuel electrode configuration to better deconvolute electrochemical processes, and redox cycles are done in-situ at elevated temperature. Reduction and redox cycling is also performed with in-situ XRD to measure the resulting phase transformations.

6.3 Results and Discussion

STF and STFN systems were characterized by electrochemical impedance spectroscopy, in-situ powder XRD, and ex-situ electron microscopy; each will be discussed in its respective section.

6.3.1 Electrochemical Measurement

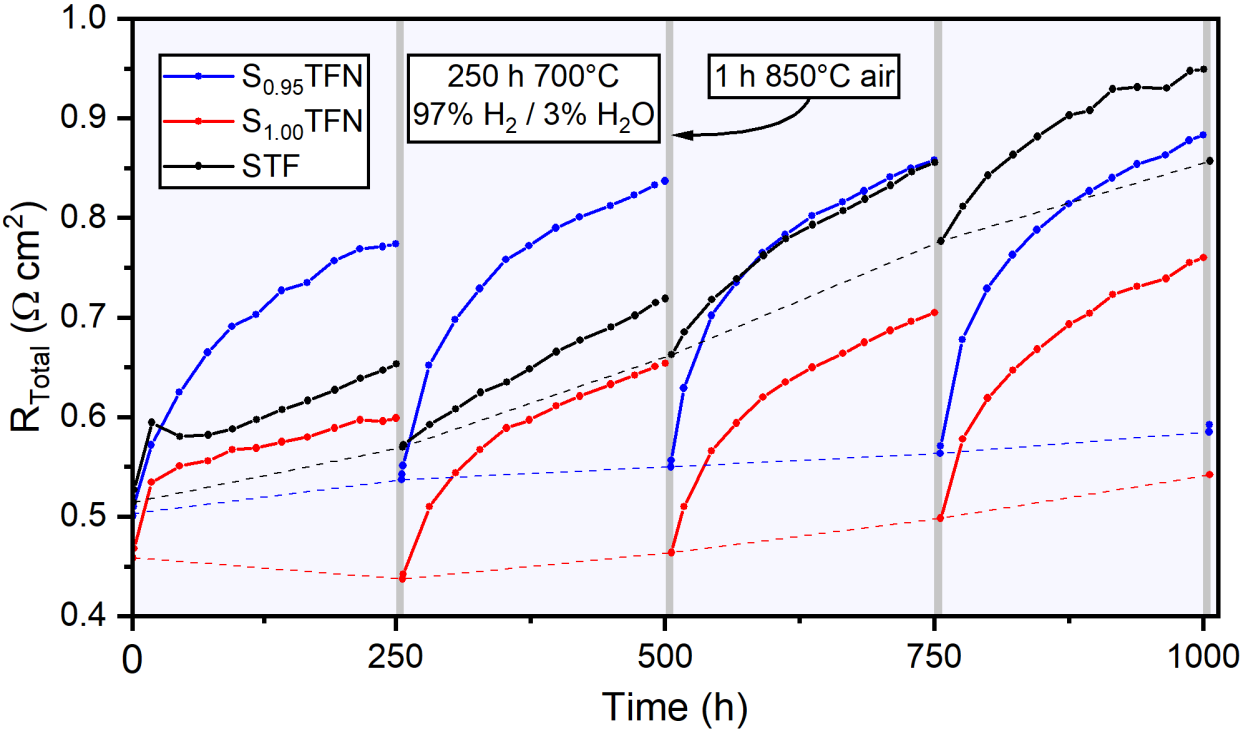

Figure 6.1 Total polarization resistance of STF, stoichiometric STFN, and A-site deficient STFN in H_2 (3% H_2O) at 700°C, with elevated temperature oxidation every 250 hours at 850°C.

The profile of the total resistance (ohmic plus polarization) is presented first for a broad overview of the degradation behavior of the three cells under study. Although it is common to subtract ohmic resistance in symmetric electrode experiments, it is found that degradation occurs both in polarization and in ohmic resistance, and redox cycling affects both. Later, the individual contributions to resistance will be delineated via equivalent circuit modeling and distribution of relaxation times analysis.

The initial 0 to 250 h degradation of A-site deficient $S_{0.95}$TFN resembles a 2nd-order curve which slows to a steady-state degradation rate sometime after the first 150 h. This behavior resembles the drop off in peak power density reported in an earlier study of the material when pre-reduction was not used.[22] The stoichiometric $S_{1.00}$TFN has a much more rapid first ascent followed

by steady-state degradation after just 24 h. Finally, non-Ni doped STF exhibits a similar sharp increase in the first 24 h, but comes down after 24 h. Note that this does not appear to be an errant data point, as the subsequent two points also deviate from the straight-line trend that ensues (also see later Figure 6.4).

After 250 h, the samples are exposed to air, first by purging the gas lines with Ar for 0.5 h, then switching to air, then ramping to 850°C for 1 h, holding for 1 h, ramping down to 700°C again for 1 h, and finally purging again with Ar before re-introducing hydrogen (the schedule can be found in Figure 3.1). The higher temperature of 850°C was chosen after preliminary testing revealed better performance recovery than when oxidizing at the testing temperature of 700°C. The entropic effect of re-dissolving Ni into the lattice should be increased upon increasing the reoxidation temperature, although 850°C is still comparatively lower than the 1200°C firing temperature during solid state synthesis.

Each reoxidation cycle resets the material to a lower R_{Total} than after the 250 h in hydrogen. A line connecting the first measurement taken is plotted alongside the data. The slope of this line has two stages: the first segment (between 0 and 250 h) has a largely different slope than the remaining 3 segments, which are all of similar slope. This indicates that the rate of degradation changes after the first redox cycle, and reduction has a partially permanent effect.

Unexpectedly, the stoichiometric $S_{1.00}$TFN outperforms A-site deficient STFN across the 1 kh experiment. This differs from the previously reported better performance of the A-site deficient $S_{0.95}$TFN, but one notable difference in the methodology was the lack of a pre-reduction period prior to testing.[22] In the event of pre-reduction, significantly different composition of exsolved particle was predicted (greater % Fe), and other phase transformations may be

exacerbated. By analyzing the 0 h slope across redox cycles, indeed the stoichiometric $S_{1.00}$TFN appears to be degrading more rapidly. These results are quantified in Table 6.1 below.

Table 6.1 Degradation rates for STF and STFN life-tests broken into two steady-state segments, the degradation within one reduction period (after 150 h) and the degradation between redox-reset periods (starting with the first reset at t=250 h)

Sample	Intra-Reduction Cycle Degradation Rate (t>150 h)	Redox-Reset Degradation Rate (t>250 h)
STF	81%/kh	81%/kh
$S_{1.00}$TFN	70%/kh	34%/kh
$S_{0.95}$TFN	70%/kh	12%/lh

The "Intra-Reduction Cycle Degradation Rate", i.e., the steady-state degradation present during reduction averaged across all four reduction segments, and "Redox-Reset Degradation Rate," i.e., the points connecting the 0 h R_{Total} values taken immediately after reoxidation, are calculated and presented in Table 6.1. The lowest observed degradation rate is for the A-site deficient STFN across its redox cycles, versus the highest, for STF both degrading across redox cycles and within pure reduction periods. From this it is evident that the redox-resetting procedure does not help nor hinder the perovskite anode absent Ni-metal particle exsolution. An STFN-based anode, in contrast, could possibly degrade at a lesser rate if redox cycling were a part of its duty cycle, more so if initial A-site deficiency is utilized.

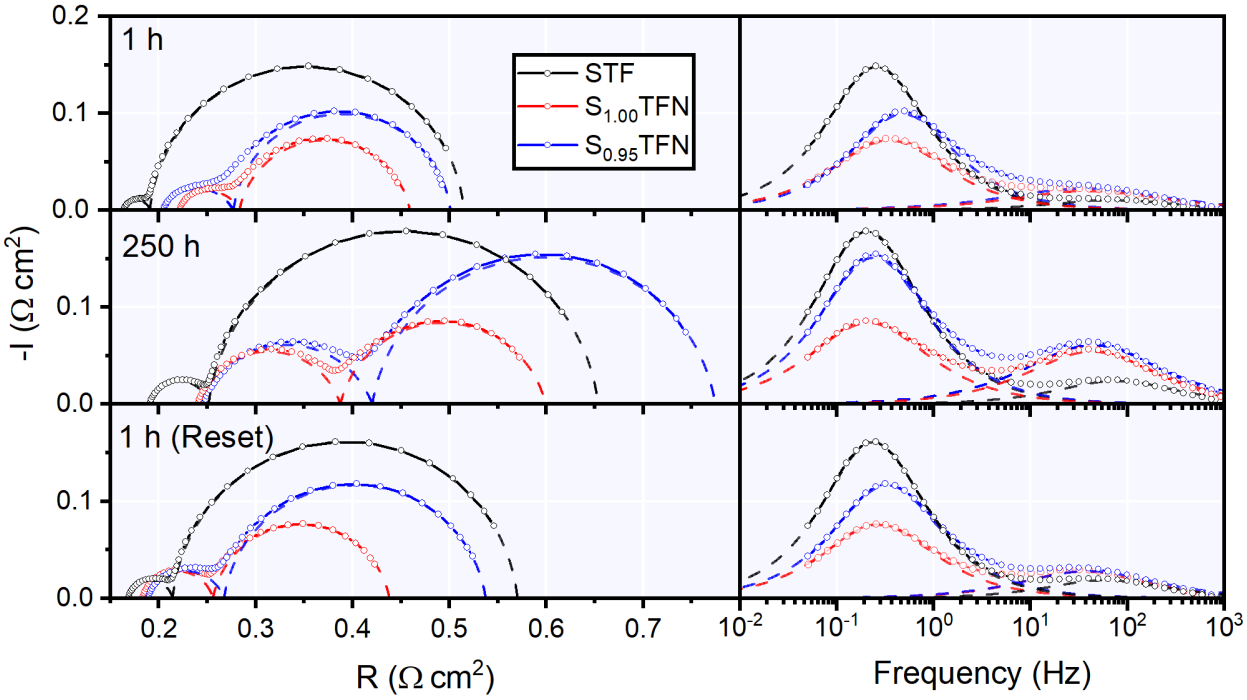

Figure 6.2 Nyquist and bode plots of initial, 250 h, and reset electrochemical performance for STF, stoichiometric STFN, and A-site deficient STFN. The data is modeling with an inductor, resistor, and two RQ elements at ~0.5 Hz and 50 Hz.

The impedance arcs in Nyquist and Bode form of the first reset are shown in Figure 6.2. An impedance model consisting of an inductor, resistor, and two RQ elements fits the data. Later, distribution of relaxation times supports there being the same two major processes occurring across all samples throughout the 1 kh experiment. Ohmic resistance is not normalized to zero for the samples because they were uniformly prepared on commercial electrolytes, and ohmic resistance changes throughout the experiment because of the relatively low conductivity of the samples. Therefore, ohmic resistance is an important additional point of comparison for these electrodes.

Previous literature on perovskite anode symmetric cells supports that an arc of ~0.1 Hz is associated with hydrogen adsorption/disassociation, and 10-100 Hz is associated with electron transfer either in the hydrogen oxidation reaction or at the electrode/electrolyte interface.[115-117]

Figure 6.3 displays R_{Total} broken into ohmic resistance (R_O), the high frequency RQ contribution to polarization resistance associated with charge transfer (R_{CT}), and the low frequency RQ contribution associated with adsorption/dissociation (R_{AD}) across each of the four reduction rounds between redox cycles, for STF, stoichiometric $S_{1.00}$TFN, and A-site deficient $S_{0.95}$TFN. Several remarkable features will be described that help elucidate the degradation process and what processes are resettable by redox cycling.

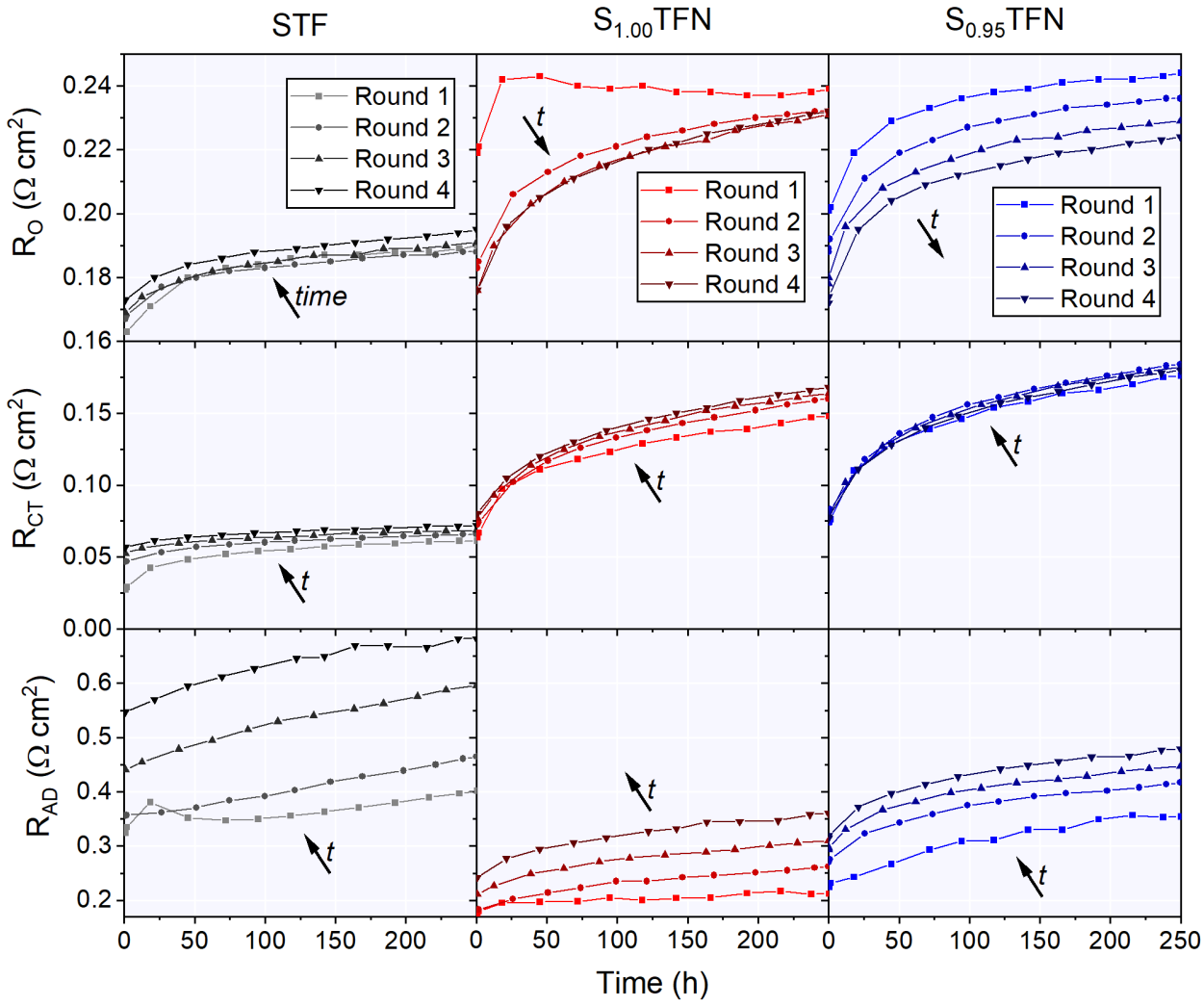

Figure 6.3 Polarization broken into ohmic resistance, the first high frequency RQ element associated with charge transfer (R_{CT}), and the second low frequency RQ element associated with adsorption/dissociation (R_{AD}) for STF, stoichiometric STFN, and A-site deficient STFN.

Starting with ohmic resistance, STF and $S_{0.95}$TFN show sloping rises towards a steady-state degradation across the latter 200 hours of reduction. All three stoichiometries show that ohmic resistance deteriorates over time, but upon redox cycling, ohmic resistance improves for the Ni-containing $S_{1.00}$TFN and $S_{0.95}$TFN. This phenomenon is most pronounced in $S_{1.00}$TFN between its first and second reduction rounds, in which ohmic resistance decreases nearly 20% its absolute value, which is remarkable given the majority of ohmic resistance should be through its ~150 μm ScSZ electrolyte.

The high frequency RQ element associated with charge transfer, R_{CT}, which comprises the least contributed resistance to R_{Total}, shows similar behavior across the three cells, in which resistance increases both over the course of reduction and as the redox rounds progress. However, the starting value is nearly uniform for $S_{0.95}$TFN, while it increases marginally for $S_{1.00}$TFN, and somewhat less marginally for STF. As mentioned, this arc has been previously ascribed to bulk charge transfer processes, and the results imply that these resistances more than double for the Ni-containing cells. The meaning for this will be presented in context with phase and microstructure data, to follow.

The least resettable element, then, and the largest contribution to R_{Total}, is the low frequency RQ arc associated with adsorption/dissociation, R_{AD}. For STF, this value increases across redox cycles with only marginal decreases in magnitude after redox cycling, 10% improvement. These values are displayed in Table 6.2. $S_{1.00}$TFN and $S_{0.95}$TFN reset more emphatically with 20% and 30% each, although they also both increase in R_{LF} more over time, with ~50% increase over the course of the reduction round.

Table 6.2 Percent increases in R_{AD} throughout the experiment and after redox cycling.

STF			$S_{1.00}$TFN			$S_{0.95}$TFN		
Increase over Previous R_{AD}			Increase over Previous R_{AD}			Increase over Previous R_{AD}		
Round	0 h	250 h	Round	0 h	250 h	Round	0 h	250 h
1	0%	24%	1	0%	20%	1	0%	55%
2	-11%	31%	2	-14%	44%	2	-24%	54%
3	-5%	35%	3	-19%	47%	3	-29%	52%
4	-8%	25%	4	-22%	49%	4	-30%	52%
5	-9%		5	-22%		5	-29%	

The presence of nickel-containing nanoparticles, then, is most useful for decreasing R_{AD}. The decrease in R_{AD} (Figure 6.4) after 24 h for STF also implies it is associated with the nanoparticle decorations, as initial nucleation of Fe has been seen to be slow via XRD (next section). This arc has been previously associated strongly with pH_2, further confirming it is related to adsorption/dissociation of hydrogen.[118]

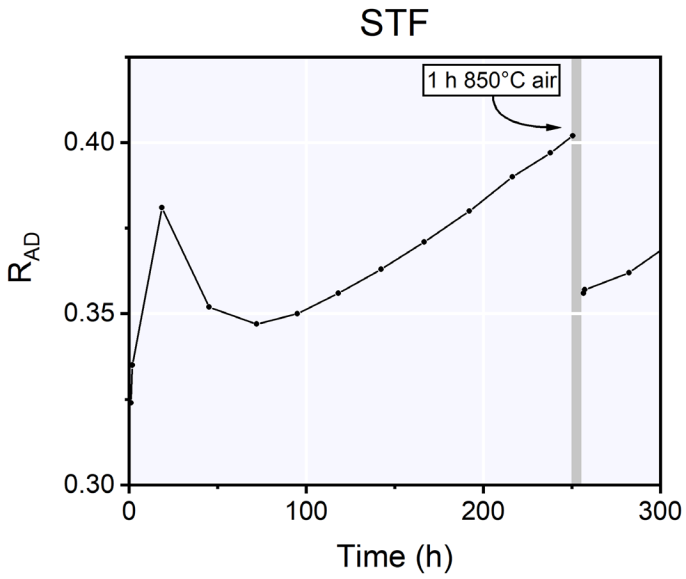

Figure 6.4 The behavior of STF in its first 250 hour reduction. The behavior, associated with H_2 adsorption/dissociation, suggests that the exsolved Fe catalyst phase nucleates after 24 h.

The higher frequency and lower resistance R_{CT} would seem to be most associated with the parent (perovskite) structure. The lowest recorded value is the initial value for STF. This response

increases only weakly for STF and strongly for the two STFN samples within one reduction cycle. This is consistent with previous literature on perovskite anodes supports that an arc of 10-100 Hz is associated with electron transfer either in the hydrogen oxidation reaction or at the electrode/electrolyte interface.[115-117]

That STF does not fully reset its low frequency arc, and that the initial reduction shows an increase then a decrease that is not reproduced anywhere else, suggests that exsolved BCC iron may be difficult to return to the perovskite phase. From the XRD data, we know Fe does not form within the first 4 hours of reduction but is present by 24 h. Additionally, it is evident that both R_O and R_{CT} increase immediately into the reduction. Therefore, the initial steep rise in R_{Total} should be from the perovskite itself developing surface enrichment prior to exsolution and the formation of an R-P phase (to be discussed subsequently).

A model-independent approach to analyzing the data is presented via the Distribution of Relaxation Times (DRT) in Figure 6.5. Across each column are the three samples, and each row represents, respectively: (a)-(c) the first 250 hours of data collected in the reducing environment, (d)-(f) the impedance at the beginning of each redox cycle, and (g)-(i), the impedance at the end of each redox cycle, 250 hours each. DRT was fit with a regularization parameter of 10^{-3} and a Full-Width-Half-Max value of 0.5 (twice the spacing of 10 measurements per decade of EIS).

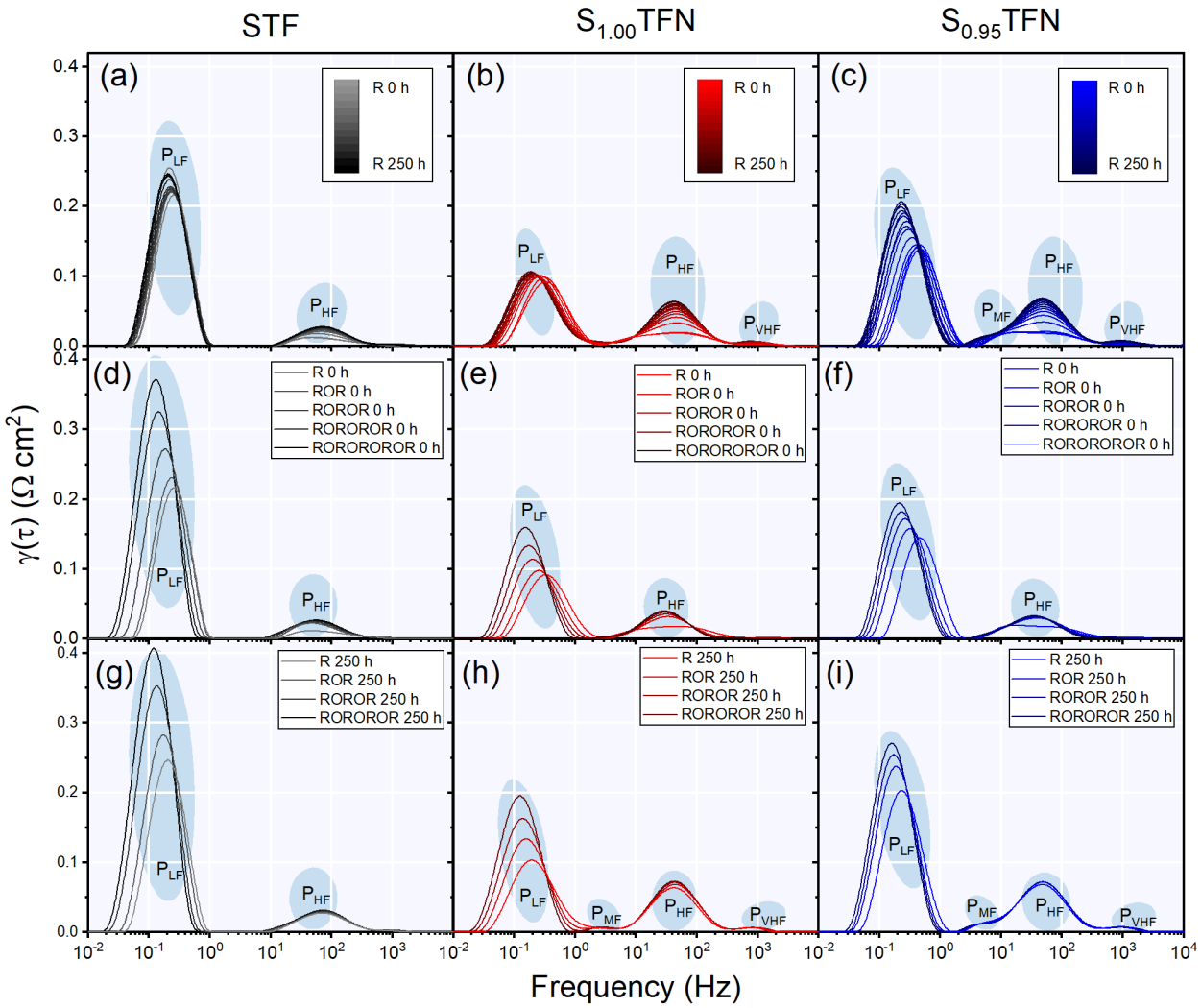

Figure 6.5 Distribution of Relaxation Time (DRT) analysis of the 5-times redox life-test of STF, stoichiometric STFN ($S_{1.00}$TFN), and A-site deficient STFN ($S_{0.95}$TFN). Panels (a)-(c) depict the impedance of the first 250 hours of ageing, (d)-(f) the impedance at each reset point before ageing, and (g)-(i) the impedance after 250 hours of ageing of each reset cycle.

The DRT shows two major peaks and is similar to the Nyquist/Bode and equivalent circuit modeling approach: one centered at ~0.5 Hz, and the other at ~50 Hz, labeled P_{LF} (low frequency) and P_{HF} (high frequency), respectively. However, after ageing, it is possible to resolve two new processes, labeled P_{MF} (medium frequency) and P_{VHF} (very high frequency), in the Ni-containing samples. Compared to the Nyquist and Bode plots of Figure 6.2, these processes are obfuscated by the comparatively larger high frequency arc, R_{CT} in the equivalent circuit. That they only appear

in the Ni-containing samples suggest they are additional processes to do with increased total exsolution (noting that STF still produces exsolved iron). These additional processes also affect A-site deficient STFN worse, which could imply that they are exacerbated by the increased Ruddlesden-Popper presence (X-ray results to follow). Together they imply that the processes have to do with charge conduction from (Ni,Fe) to the R-P phase and R-P to the perovskite. This is in line with the understanding that oxygen diffuses through interstitial sites in R-P and through oxygen vacancies in perovskites.

Similar to the equivalent circuit modeling of Figure 6.3, the DRT of Figure 6.5 shows that the redox resetting procedure is effective in resetting the high frequency process P_{HF}, but now also in resetting P_{MF} and P_{VHF}. It is more discernible from the DRT that the first round of reduction starts with a lower P_{HF} that never fully recovers after the first cycle, for all 3 samples. This may indicate a permanent reorganization of the lattice upon the first extensive formation of R-P. The resetting temperature, 850°C, then, even if it ultimately can transform the R-P phase to the perovskite phase, is not enough to fully re-homogenize it.

6.4 STFN Performance as an Oxygen Electrode

Although this study concerns STFN as a fuel electrode, other STF-based perovskites have been designed specifically for oxygen electrode use. Other groups have reported increased oxygen electrode performance with STFN after redox cycling.[119-121] Since redox protocols for this study have the electrodes in air for a brief period of time, it was possible to acquire electrode performance in air for the $S_{0.95}$TFN sample, presented here for completeness.

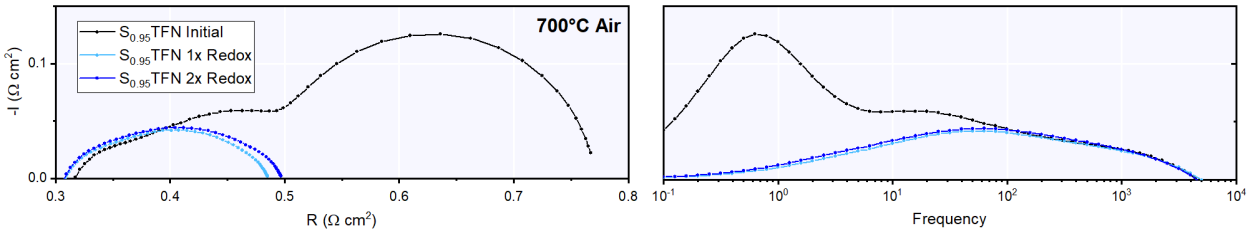

Figure 6.6 Performance of STFN in air initially and after one and two redox cycles.

Initial performance by STFN is low, with an approximate polarization resistance of 0.45 Ω cm^2, compared to documented polarization resistances of $SrTi_{0.3}Fe_{0.7}O_{3-\delta}$ of 0.1 Ω cm^2 at 700°C in air.[122, 123] However, after 250 h reduction (and 30 minutes of argon gas), and then switching back to air, polarization resistance drops to 0.18 Ω cm^2. By analyzing the Bode plot in Figure 6.6, some basic observations can be made, although rigorous analysis is not provided here given the scope of the study. It is evident that the response centered at 1 Hz is eliminated upon exsolution of Ni from the perovskite lattice. A medium frequency arc at around 50 Hz is also minimized, and the high frequency arc remains largely the same. Upon a second 250 h round of reduction, followed by brief oxidation, the polarization resistance increases marginally. This also indicates that there is minimal microstructural evolution over the course of the experiment.

The shape of the redox-cycled STFN impedance more closely resembles Nyquist plots of STF reported elsewhere[122, 123] as well as similar A-site deficient and stoichiometric STFN that were not subject to redox cycles.[119] Although the stoichiometry and processing differed slightly, these STFN cells have a similar low frequency arc centered at 1 Hz, but their polarization resistance is only ~0.22 Ω cm^2 at 700°C. Given that in our results the response around 1 Hz was eliminated upon redox-cycling, the presence of Ni in the perovskite lattice seems deleterious to ORR kinetics.

6.5 X-ray Diffraction

Initial attempts to use ex-situ X-ray diffraction were mired by the formation of a strontium iron hydrate, either formed during cooling to room temperature in humidified Ar or during sample preparation with an aqueous solvent used for fixing the powder to its glass holder The hydrate is displayed in Figure 6.7 and was identified to be the hydro-garnet $Sr_3Fe_2(OH)_{12}$ which is only stable up to 225°C, indicating it was an artifact of ex-situ analysis.[124]

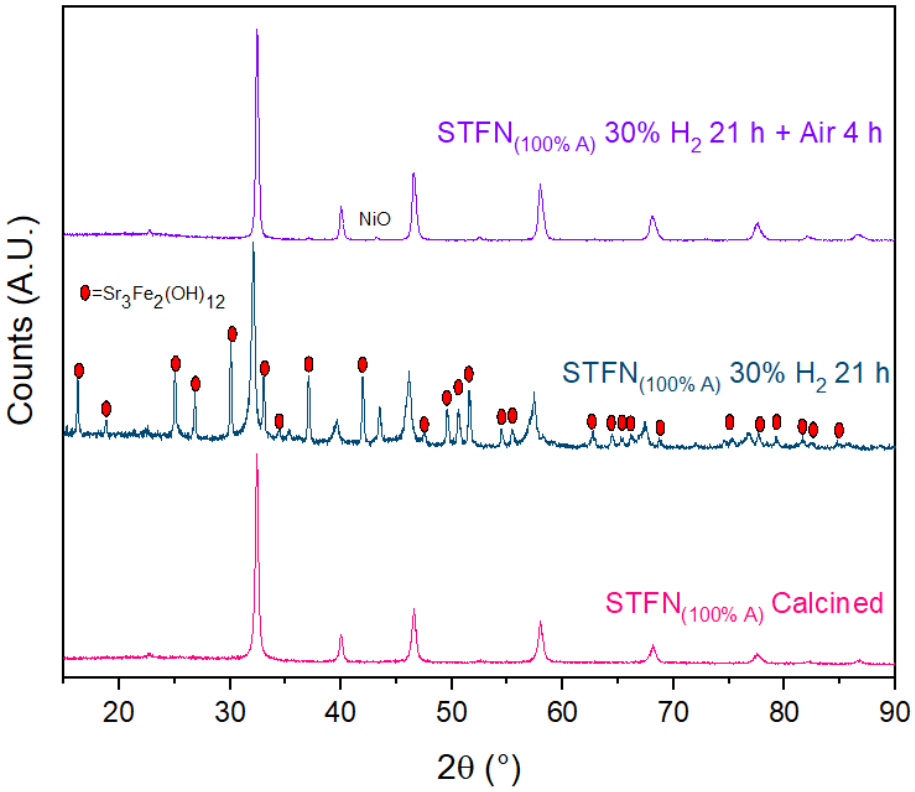

Figure 6.7 Early attempts to measure the reduced state of STFN yielded hydrated phases only stable at low temperatures as a result of ex-situ sample preparation. Here stoichiometric STFN was reduced in 30% H_2 at 850°C, driving more extreme exsolution and phase transformation than the main 700°C condition of the study.

The artifacts were found to be avoided if cooling took place instead in hydrogen, rather than Ar, and importantly, with water bubbling shut off below 150°C to avoid any chance of water condensation on the samples. Subsequent samples were also reduced at 700°C rather than 850°C, potentially mitigating the extent of iron exsolution. In any case, ex-situ data is still prone to lattice

reorganization in the event of any exsolved iron. The environment of 97% H_2 and 3% H_2O has an effective pO_2 equal to the equilibrium pO_2 of Fe with Fe_3O_4 at 275°C; below this temperature, iron oxide is expected to form.[44, 45] Nickel, however, is expected to remain in the metal phase in 97% H_2 + 3% H_2O across all temperatures. It is unknown if nickel-iron alloys, however, may be subject to iron oxidation and thus deplete in Fe-content over time. Other researchers have found iron oxidation to have occurred in a similar exsolution system, $La_{0.6}Sr_{0.4}FeO_3$, during ex-situ STEM studies, prompting in-situ STEM to instead be used.[125] The Ruddlesden-Popper phases that form are of unknown stability as well, and metallic iron could redissolve back onto the B-site. This is indeed what appears to be the case when comparing the ex-situ and in-situ results, the in-situ XRD being after 4 hours of reduction, and the ex-situ after 24 hours of reduction, in Figure 6.8.

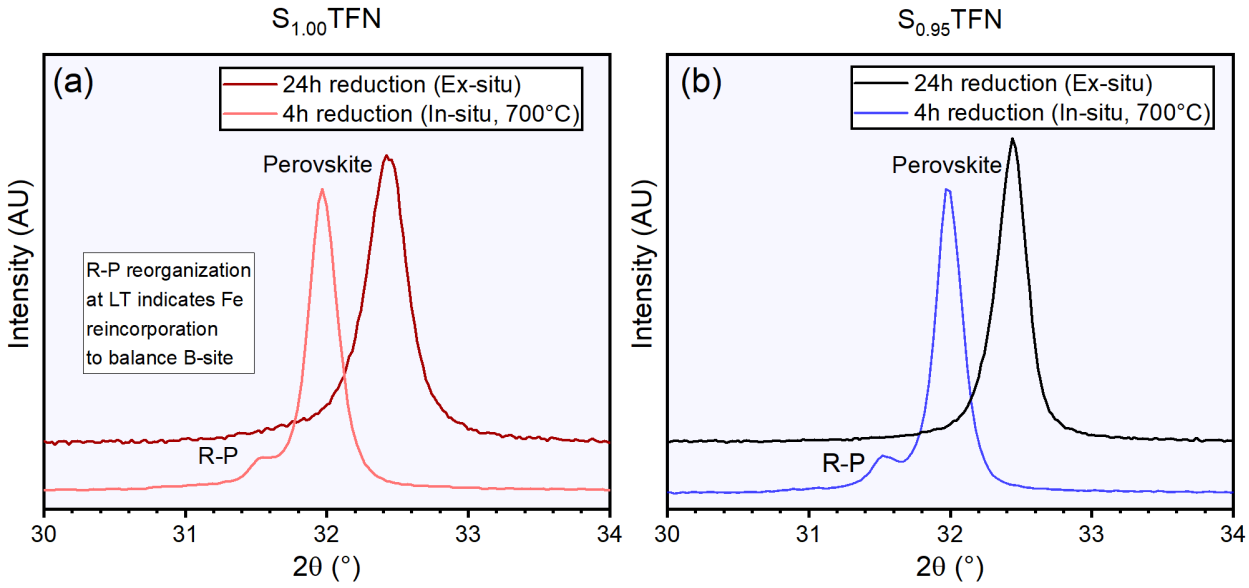

Figure 6.8 Ex-situ and in-situ XRD demonstrate that the cooling procedure used to test ex-situ results in the loss of the Ruddlesden-Popper phase due to low temperature instability of either Fe metal or the R-P phase itself, for (a) stoichiometric $S_{1.00}$TFN and (b) A-site deficient $S_{0.95}$TFN.

The $S_{0.95}$TFN and $S_{1.00}$TFN material have been studied by ex-situ XRD before, and Ruddlesden-Popper phases were not reported, possibly due to lattice reorganization of iron at low temperature.[29, 119] Therefore, in this study, in-situ XRD was used in order to track phase formation

in the STF, stoichiometric $S_{1.00}$TFN, and A-site deficient $S_{0.95}$TFN over 4 hours of reduction time, followed by a similar redox cycle in 850°C air. The initial powder held at 700°C in air is presented in Figure 6.9.

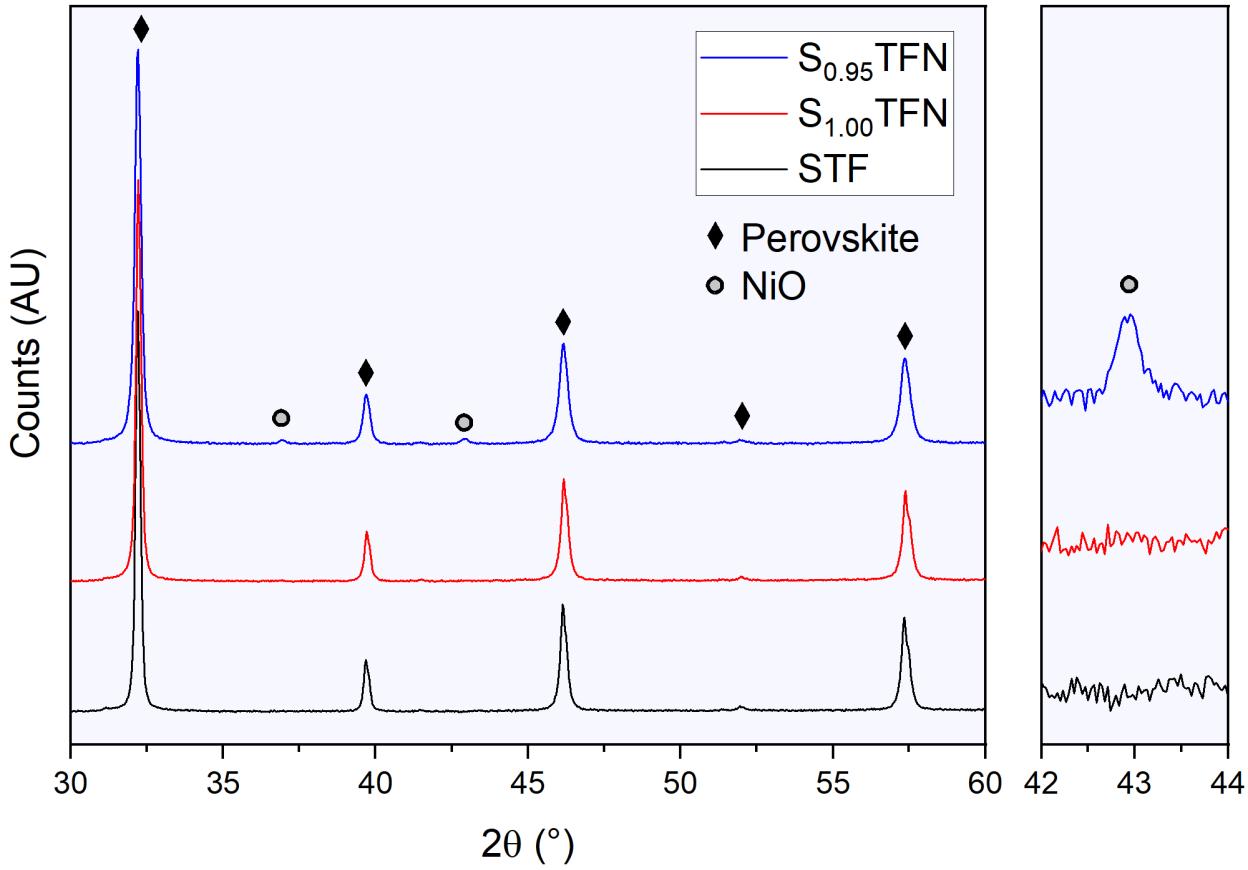

Figure 6.9 Initial structure of STF, stoichiometric $S_{1.00}$TFN, and A-site deficient $S_{0.95}$TFN in air at 700°C. The $S_{0.95}$TFN sample includes a proportion of excess bulk NiO after synthesis.

Good phase purity is achieved for STF and the stoichiometric $S_{1.00}$TFN, with its 7% Ni substituted onto the B-site with -7% Fe to compensate. However, the A-site deficient $S_{0.95}$TFN shows a clear NiO phase, indicating that 5% A-site deficiency in the perovskite structure leads to being unable to accommodate 7% Ni^{2+}. This stoichiometry of $S_{0.95}$TFN was initially reported with full substitution of Ni on the B-site,[22] but in a subsequent publication it was acknowledged that some NiO can be detected at ~1 wt%.[29]

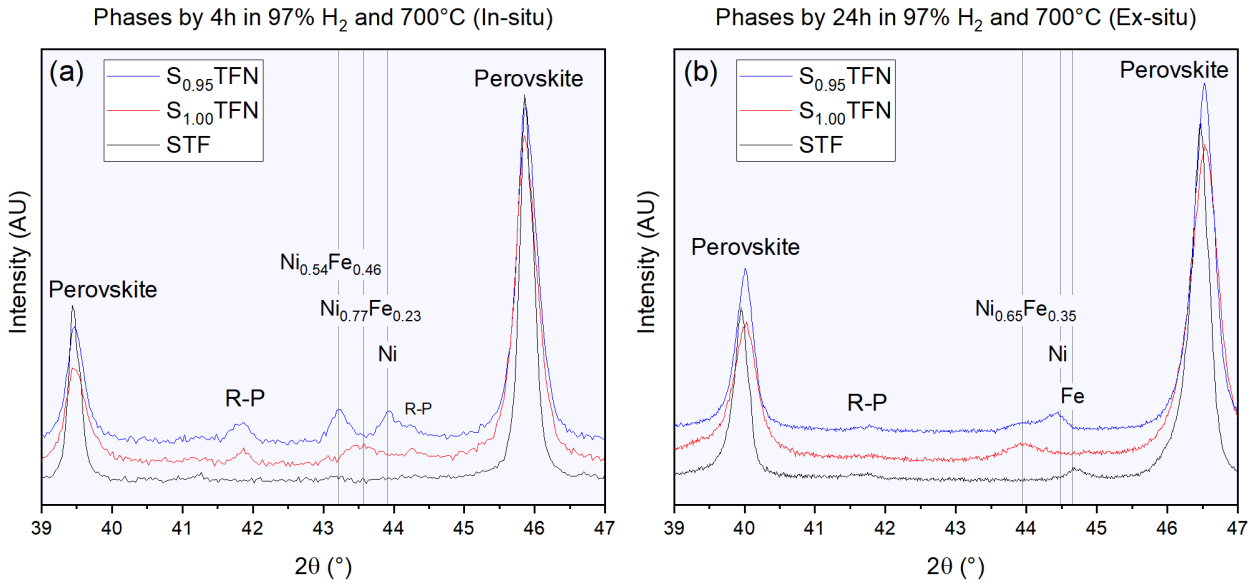

Figure 6.10 X-ray diffraction data for STF, stoichiometric $S_{1.00}$TFN, and A-site deficient $S_{0.95}$TFN after reduction. (a) In-situ data after 4 h in 97% H_2 + 3% H_2O. (b) Ex-situ data after 24 h in 97% H_2 + 3% H_2O.

The results for the materials after periods of time reducing are shown in a region of the scan to highlight metal formation, in Figure 6.10.The in-situ data in Figure 6.10(a) shows the formation of Ni, Fe, and (Ni,Fe) alloy after 4 h in hydrogen (3% steam). No metal phases appear for STF. The two Ni-doped phases also show a small peak associated with the Ruddlesden-Popper phase, although its maximum intensity peak is at ~31.5° (Figure 6.8). For $S_{1.00}$TFN, the metal alloy is approximated to be composition $Ni_{0.77}Fe_{0.23}$ by this stage. The $S_{0.95}$TFN displays two peaks: one that is pure Ni, due to bulk NiO in the starting powder, and a less Ni-rich $Ni_{0.54}Fe_{0.46}$ alloy.

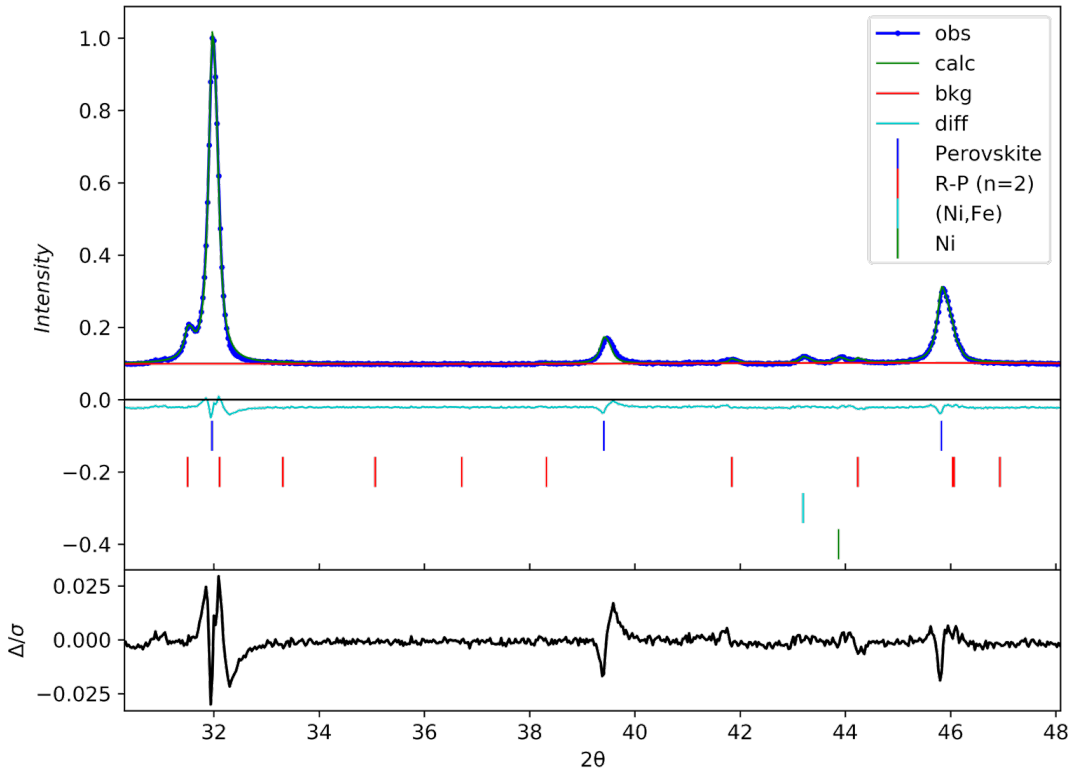

Figure 6.11 Rietveld refinement for $S_{0.95}$TFN after 4 h exposure to 97% H_2 (3% H_2O), in-situ at 700°C.

Indexing of the phases was performed by Rietveld refinement.[64] Figure 6.11 shows the result of fitting $S_{0.95}$TFN with phases for the perovskite (COD ID 1525550), the n=2 Ruddlesden Popper phase (PDF# 04-014-6010) , FCC Ni-Fe alloy (PDF# 01-088-1715), and pure FCC Ni (PDF# 00-004-0850). Here the n=2 R-P phase ($Sr_3(Ti,Fe)_2O_7$) is supported by the SrO-TiO_2 phase diagram, albeit at 1400°C, which has excess SrO forming $Sr_3Ti_2O_7$ at ~1400°C.[126] $S_{1.00}$TFN was indexed with the same phases except for pure Ni. Indexing of the metals was performed by accounting for thermal expansion, using a coefficient of thermal expansion value of 1.827×10^{-5} K^{-1} for FCC Ni as well as its FCC binary alloys with Fe.[127] Vegard's law is valid until <40% Ni, the Invar region, in which the lattice constant stops increasing with further Fe substitution.[128] BCC iron was indexed directly via a measurement of pure Fe at 700°C.[129]

Previously the atomic percent content of Ni in FCC (Ni,Fe) was acquired using ex-situ XRD, STEM-EDS, and in-situ TGA. It was found that A-site deficient $S_{0.95}$TFN yielded exsolved particles of $Ni_{0.45\text{-}0.49}Fe_{0.51\text{-}0.55}$ and stoichiometric $S_{1.00}$TFN yielded compositions of $Ni_{0.36\text{-}0.42}Fe_{0.58\text{-}0.64}$ after 4 h at 850°C in 30% H_2 3% steam, balance Ar. The stoichiometry via XRD was interpreted via a study that reported (Ni,Fe) lattice constant as a function of composition but data was limited. Here, instead, a semi-empirical approach was taken whereby ambient condition data for 24 alloy compositions up to $Ni_{0.4}Fe_{0.6}$ and 54 values for pure Ni were plotted vs. lattice constant, all acquired from the crystallographic registry of the ICDD PDF4+ software.[130] This approach minimizes the systematic error of any one experiment, and the calculated linear regression is shown in Figure 6.12. It should be noted that at elevated temperature (1000 K), Vegard's law deviates starting at around the 50% Fe-rich mark rather than 40% at room temperature; in our case, Vegard's law is valid because the compositions stay below 50% Fe.

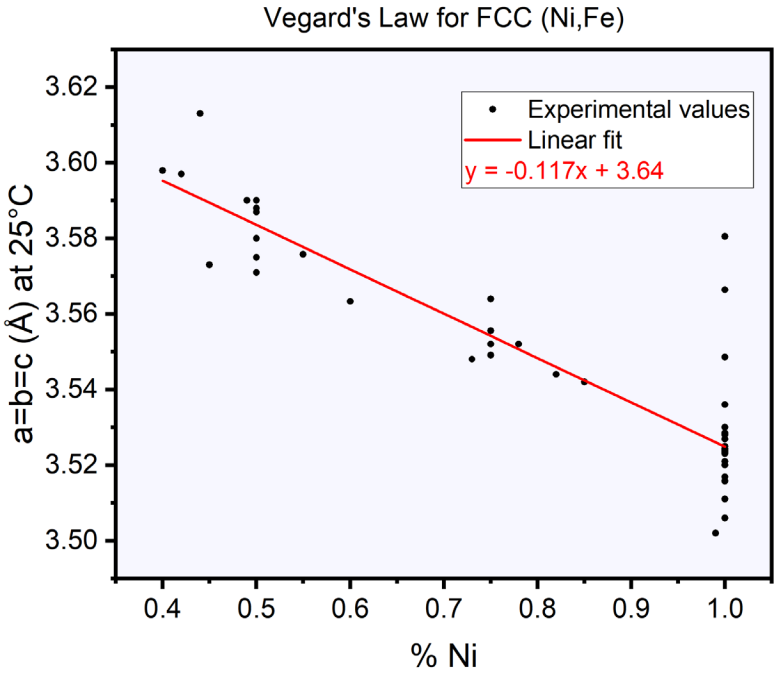

Figure 6.12 Vegard's law applied to 24 (Ni,Fe) alloy compositions and 54 for pure Ni. Data from the PDF4+ crystallographic database.[130]

Also shown in Figure 6.10(b) is ex-situ data collected after 24 h. Longer reduction times were collected ex-situ due to safety limitations in leaving the in-situ diffractometer unattended. As mentioned, this data should be interpreted with the caveat that it could be artificially underestimating the concentration of Fe in the particles; as shown in Figure 6.8, the Ruddlesden-Popper phase disappears, and by thermodynamic equilibrium, Fe should convert to Fe_3O_4 below 225°C.

Here, the exsolved particles associated with $S_{1.00}$TFN have become more Fe-rich with time, so even if some Fe left the particles during cooling, the result is still that continuous Fe-enrichment occurs from 4 h to 24 h. The same Vegard's law calculation was applied to calculate composition, but without thermal expansion. For $S_{0.95}$TFN, it is more difficult to place the peak for the binary alloy, but significant volume fraction of pure Ni is apparent. However, the binary alloy peak does appear to have shifted towards greater Ni-richness versus its 4 h in-situ equivalent, possibly from Ni diffusion from bulk Ni to the nanoparticles.

Remarkably, the STF sample now shows a clear peak for BCC Fe, whereas it was absent in the 4 h in-situ trial. This behavior is consistent with the EIS data highlighted in Figure 6.4, in which polarization arc R_{AD} decreases after 24 h. Fe phase fraction is evident in the XRD despite the propensity for R-P to reform into the perovskite and Fe to re-oxidize, which may have led to the loss of some Fe phase fraction. The fact that Fe appears in the 24 h reduction but not in the 4 h reduction points to a large activation barrier in nucleating pure BCC Fe. This is due to the higher segregation energy due to strong Fe-O bonds within the lattice, as noted by other researchers.[105] On the other hand, diffusing Fe into extant Ni particles benefits from a strong entropy of mixing term, and the process occurs readily.

The n=2 Ruddlseden-Popper phase ($Sr_3(Ti,Fe,Ni)_2O_{7-\delta}$) implies the loss of 33% of the original perovskite B-site, which with 7% Ni, means $Ni_{0.27}Fe_{0.73}$; however, that Ni-rich particles are found indicates that R-P phase formation is highly localized with Ni cations from the bulk transporting to the surface. Small reductions in B-site are analogous to increases in SrO content in the SrO-TiO_2 phase diagram, which produces a mixture of $SrTiO_3$ and Sr_3Ti2O_7 left of the $SrTiO_3$ line compound.[126]

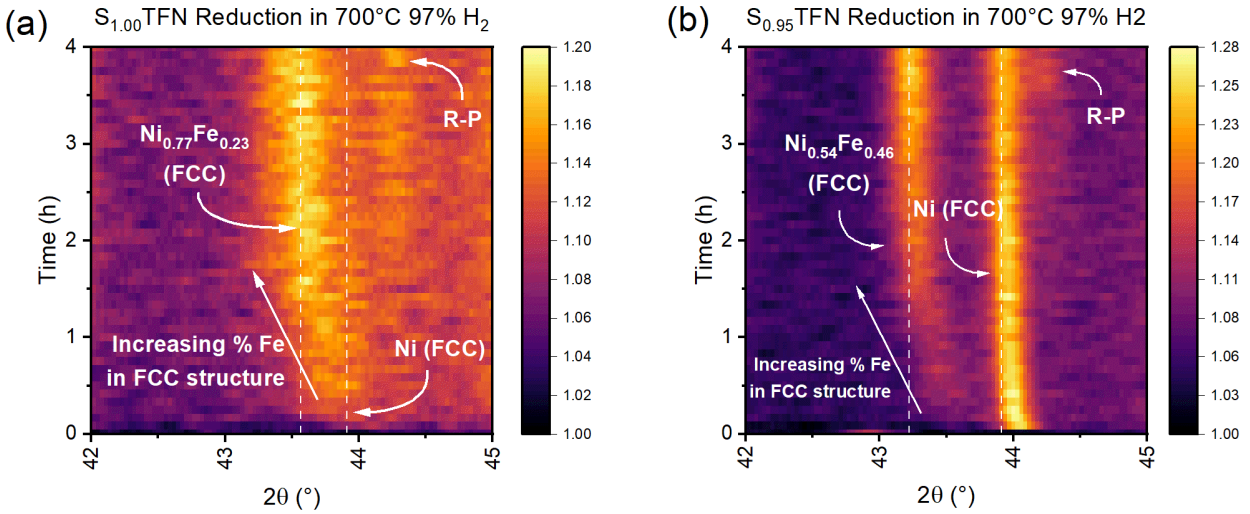

Figure 6.13 In-situ XRD during the reduction process for (a) stoichiometric $S_{1.00}$TFN and (b) A-site deficient $S_{0.95}$TFN.

The time-resolved XRD is shown in Figure 6.13. Each scan takes approximately 5 minutes to complete. These figures reveal similar phenomena, by which initially a very Ni-rich phase is nucleated, which then shifts to lower angles as Fe enters the FCC phase. Near the end of the reduction phase, a separate, additional phase consistent with the n=2 R-P phase appears. This indicates that initial nucleation is indeed driven by Ni, as the segregation energy is lower, and this is the first report the authors are aware of in which it is confirmed that the alloy exsolves and changes composition, rather than growing in size as a fixed alloy. Concomitant with this exsolution process is the formation of Ruddlesden-Popper phase consistent with an unstable excess of A-site

strontium. $S_{0.95}$TFN has a much more prominent peak at pure Ni because of excess NiO in the starting powder.

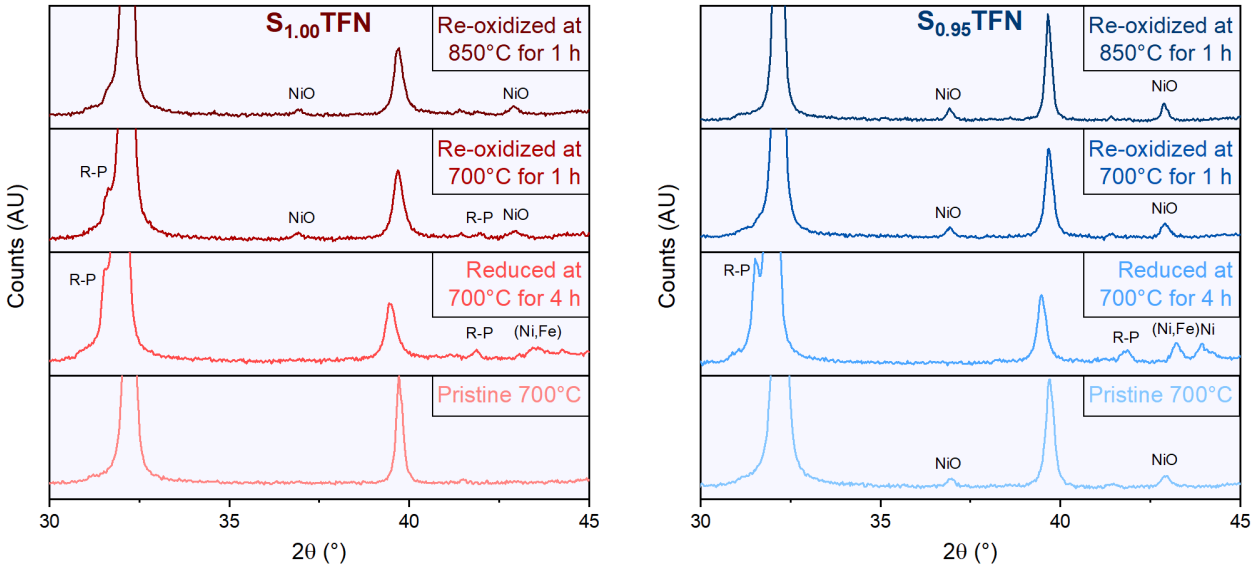

Figure 6.14 Re-oxidation behavior in-situ showing, from bottom to top, the initial oxidized state, the reduced state (4 h), the oxide formation upon re-oxidizing for 1 h at 700°C, and after 1 additional h at 850°C. All spectra recorded at 700°C for (a) stoichiometric $S_{1.00}$TFN and (b) A-site deficient $S_{0.95}$TFN.

The in-situ XRD experiment also included an oxidation cycle modeled after the one used during electrochemical testing, and the results at two different stages of it are shown in Figure 6.14 for $S_{1.00}$TFN and $S_{0.95}$TFN. Note that STF is not plotted here because no significant phase transformation occurred in the entirety of the in-situ experiment under the same conditions. After 4 h reduction, N_2 was used to purge the fuel for 1 h before introducing air for 1 h, at which point the middle panel of Figure 6.14 was taken. Upon exposure to air, the (Ni,Fe) alloy reverts back to NiO, and the R-P phase recedes for $S_{1.00}$TFN and completely returns for $S_{0.95}$TFN. The phase Fe_2O_3 is not seen, likely due to the comparatively small amount of iron as well as the greater formation energy with the perovskite phase. After this hour in 700°C air, the sample was ramped to 850°C over the course of 1 hour in air, held for 1 hour, ramped down for 1 h, and finally held again at

700°C, at which time the top panel of Figure 6.14 was collected. After the higher temperature treatment, the R-P phase is converted for $S_{1.00}$TFN as well.

6.6 Electron Microscopy

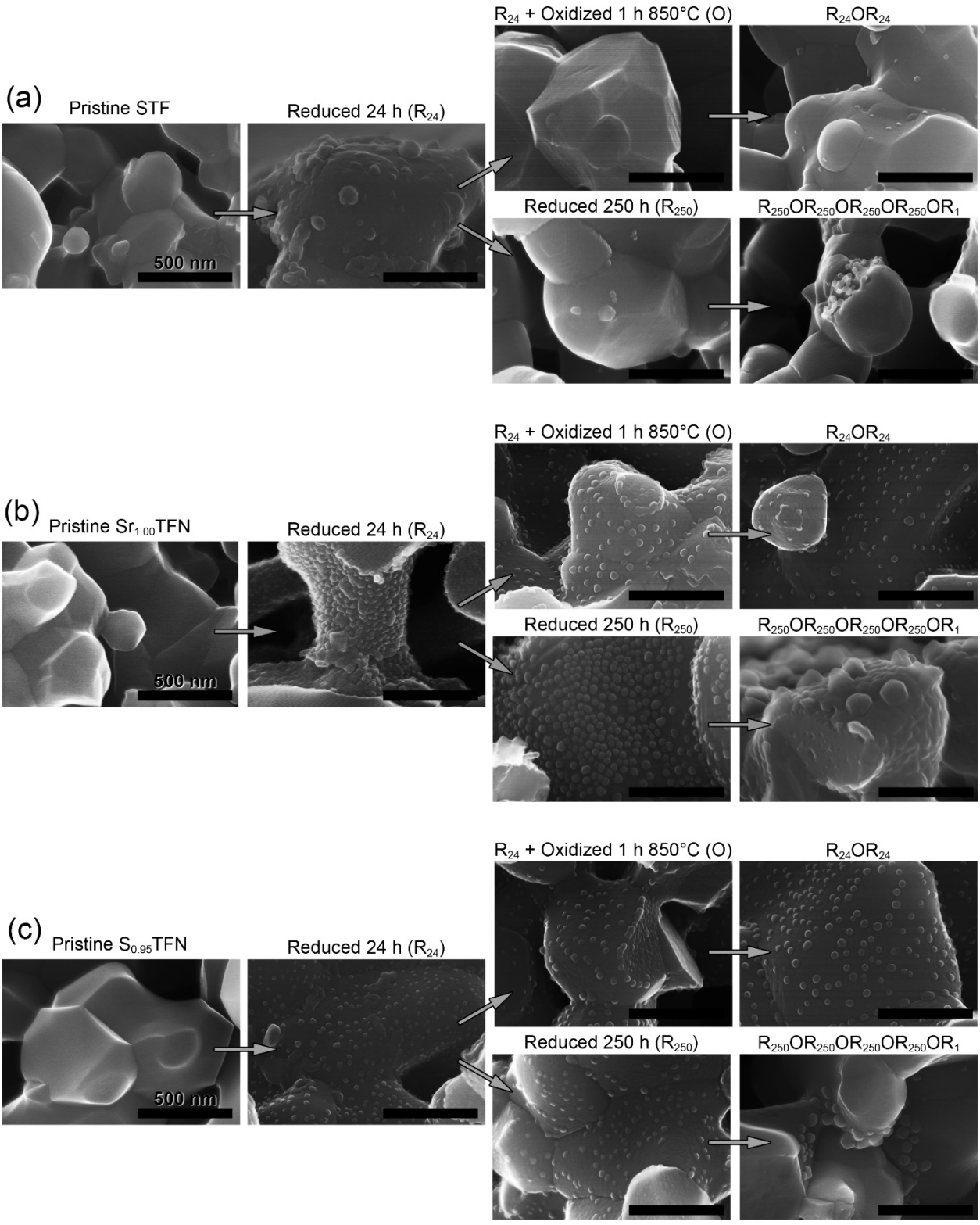

Figure 6.15 Scanning electron microscopy for over various stages of reduction and oxidation for (a) STF, (b) stoichiometric $S_{1.00}TFN$, and (c) A-site deficient $S_{0.95}TFN$

The above figure (Figure 6.15) composites SEM images of the samples in six different redox stages. The first stage is the as-oxidized, pristine perovskite phase, or in the case of $S_{0.95}$TFN, perovskite plus minority excess NiO phase, although the latter is not seen in the microstructure.

Next is the exsolved state after 24 h reduction. Note, as mentioned, that ex-situ analysis has the caveat that some Fe metal may have re-oxidized. Nonetheless, at this stage, STF shows significant phase formation corresponding to the Fe observed with XRD under the same conditions (Figure 6.10(b)). The two Ni-doped samples show divergent behavior at this stage: $S_{1.00}$TFN shows a much higher areal density of exsolved particles than does $S_{0.95}$TFN. This can be explained by the fact that, for $S_{1.00}$TFN, all the Ni is initially present in the perovskite phase and is available for exsolution; for $S_{0.95}$TFN, however, a percentage of the Ni is initially in a bulk NiO phase and would not appear as exsolved for particles. Indeed, preliminary STEM (not shown) reveals micron-scale Ni inclusions in the exsolved powder, rather than the ~50 nm morphologies typical of exsolution and seen in the micrographs. That $S_{1.00}$TFN produces much more exsolved particles at this stage corresponds to its lower R_{AD} RQ element in the impedance data. It also corresponds to its relatively rapid rise in R_O, as the phase fraction of metal is higher at an earlier stage than for the other two samples.

After this, the figure diverges into two paths: at the top is the state of the material after an 1 h 850°C oxidation event, at the bottom is the reduction period extended to 250 h, as was the length of exposure during electrochemical testing. The oxidized state clearly shows NiO particles remaining on the surface for both Ni-doped samples; STF does not show evidence of Fe oxides. The areal density of the NiO particles for $S_{1.00}$TFN and $S_{0.95}$TFN is overall very similar, implying that for $S_{1.00}$TFN, a portion of the exsolved Ni was able to return to the perovskite phase. This is

consistent with the XRD showing a smaller NiO peak for $S_{1.00}$TFN after oxidation than for $S_{0.95}$TFN (although after a shorter, 4 h reduction).

The bottom path at this juncture shows the state of the exsolved particles after 250 h. Here the density remains very high for $S_{1.00}$TFN, although the particles have taken on a more spherical shape. The particles of $S_{0.95}$TFN remain largely the same; both results attest to the stability of the socketed particles. It would also seem to imply that particles do not significantly enlarge via the taking on of more percentage Fe. However, the caveat again remains about ex-situ testing and Fe reoxidation, so Fe-enrichment causing larger particles in-situ cannot be ruled out. Given that the electrochemical results show a continued increase in R_{Total} as both polarization and ohmic resistance increase significantly from 24 to 250 h, and that this phenomenon can be reset with oxidation, it is deduced that there is continuous Fe reduction, either into the exsolved particles, or as a separate BCC phase, as seen in the in-situ XRD results.

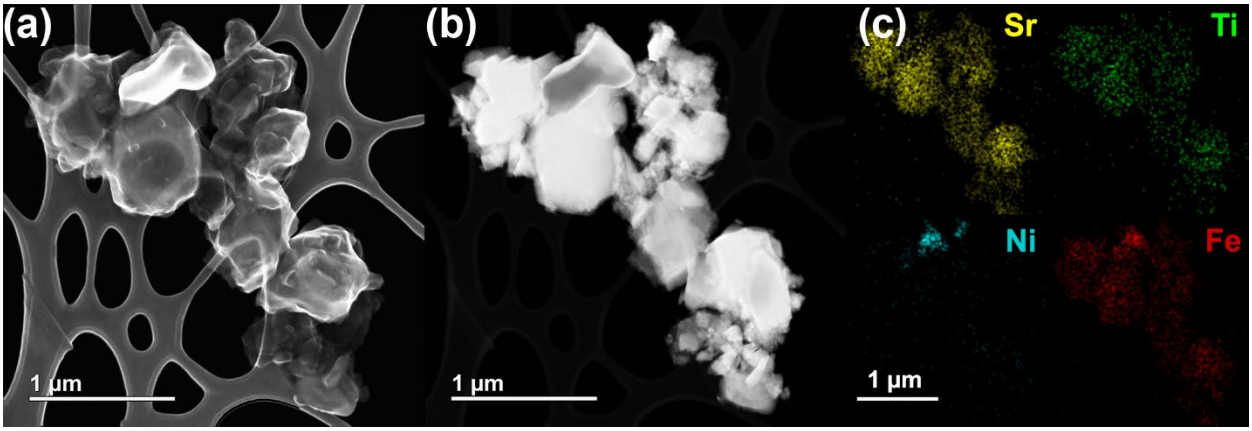

Figure 6.16 (a) Secondary electron STEM of the 1 kh redox-cycled S1.00TFN sample, (b) high angle annular dark-field, and (c) EDS elemental maps (note the reduced scale-bar, each element is tiled to be seen separately.)

Next and final on the top and bottom paths of Figure 6.15 are the result of re-reducing after (top) an oxidation cycle and (bottom) after 4 oxidation cycles. For the top path, the most significant result is that $S_{1.00}$TFN does not recover its initial high particle density. Some particles have also

grown significantly past their <50 nm starting size. These results make sense given the FCC metal phase was not required to re-nucleate from the perovskite phase, only from the extant NiO phase. Therefore, subsequent Ni and Fe can grow into a limited number of previous particles, rather than simultaneously exsolving and causing a greater areal particle density. Figure 6.16 verifies that (Ni,Fe) particles as large as 400 nm can be seen, as verified by STEM-EDS. This phenomenon helps to explain the only partial recovery of R_{AD} with redox cycles: re-reduction only results in enriching existing metal oxide particles. Indeed, on the bottom path, the results after the life-test in which four 250 h reduction cycles with four re-oxidation events, shows significantly enlarged particles that would seem to explain the decreased electrochemical performance. For STF after 1 kh and 4 redox cycles, a microporous structure is highlighted which can be found throughout the sample, of significantly different microstructure versus the bulk oxide phase. This structure is possibly FeO_x with microporosity arising from Kirkendall porosity. Such porosity has been seen with Fe redox cycled at 800°C with hydrogen and hydrogen/steam.[131] This would necessarily arise if Fe eventually were unable to re-oxidize back into the perovskite phase, building significantly larger diameter Fe particles over time which then redox cycle between iron oxide and metallic iron, again pointing to a limit in reversibility after long durations in reducing atmosphere. Notably, however, pure Fe is not seen in the STEM-EDS of $S_{1.00}$TFN in Figure 6.16, indicating continued Fe exsolution here is into the FCC phase with Ni. Indeed the solubility limit at 700°C for Fe in BCC Ni is high, at ~89%.[132]

6.7 Conclusion

The major degradation mode observed during operation of the exsolved systems STF, stoichiometric $S_{1.00}$TFN, and A-site deficient $S_{0.95}$TFN, is from previously unreported decomposition—Ruddlesden-Popper phase formation concomitant with Fe reduction, either into

the exsolved particles by way of further Fe-enrichment of the binary FCC (Ni,Fe) particles for STFN, or by the BCC Fe phase for STF. Whether there is a limiting strain energy to the continuous lattice expansion caused by increased Fe content remains an unsolved question due to the difficulty in acquiring in-situ data at significant timescales. In-situ data is shown to be paramount in characterizing both the Fe reduction and Ruddlesden-Popper phase formation; Fe oxidizes at low temperatures even in 97% hydrogen (3% steam), and the R-P phase does not appear in ex-situ measurements.

In this set of experiments, absent pre-reduction, $S_{1.00}$TFN is shown to nucleate the highest areal density of catalyst particles and performs best. However, A-site deficient $S_{0.95}$TFN shows greater stability, possibly reconciling the difference between this study and previous which used pre-reduction to accelerate to a stage of greater stability. This same pre-reduction would have led to extensive R-P formation, and indeed the results here show how initial performance can be high but fleeting as R-P and Fe-enrichment slowly take hold.

Redox cycling is partially successful at redissolving Ni and is completely successful in redissolving Fe into the perovskite lattice under the hours-long cycling conditions of the in-situ experiment. However, upon subsequent re-reduction, nucleation and growth kinetics are altered such that surface NiO acts as existing nucleation sites, and particle areal density decreases and average particle size increases, as seen in SEM results. This explains why redox cycling appears to have a limited ability to reset polarization resistance, especially the arc associated with hydrogen adsorption/dissociation.

These results identify a major degradation mode in STF-based oxides, systems previously thought to be stable under these conditions. STF does not nucleate Fe after 4 h, but does after 24 h, leading to a latent decrease in polarization resistance via the hydrogen adsorption/dissociation

impedance response. It is reasonable that, if STF were to be stabilized, either by changing its stoichiometry or by operating in higher pO_2 conditions, this decomposition-based degradation mode could be abated leading to more stable performance in STF and Ni-containing STFN.

6.8 Addendum: STFR and Ni/YSZ operated in ethanol with redox cycling

The following is an experiment in which a derivative of the STFN structure seen above, one with Ru doped instead of Ni, is exposed to ethanol vapors in a kind of accelerated coking experiment, together with a Ni/YSZ cell. The perovskite system is $Sr(Ti_{0.3}Fe_{0.7}Ru_{0.07})O_{3-\delta}$, (STFR) which can also be written to highlight its A-site deficiency as $Sr_{0.935}(Ti_{0.28}Fe_{0.655}Ru_{0.065})O_{3-\delta}$.[102] In Glaser et al. it is notable that, despite the 6.5% A-site deficiency, greater than the 5% used in the STFN study above, complete substitution is achieved without noticeable excess RuO_2. This could be due to the preferred oxidation state of Ru^{4+} being more compatible with the B-site position than for the case of Ni^{2+}.

Ruthenium metal has been previously shown to be a stable catalyst in carbon-based fuel environments.[133, 134] Ni/YSZ, in contrast, facilitates the formation of solid carbon. Even in the event of some coking, another benefit of the perovskite anode system is that it can withstand redox cycling, an event which should oxidize and thus burn out any deposited carbon into CO_2.

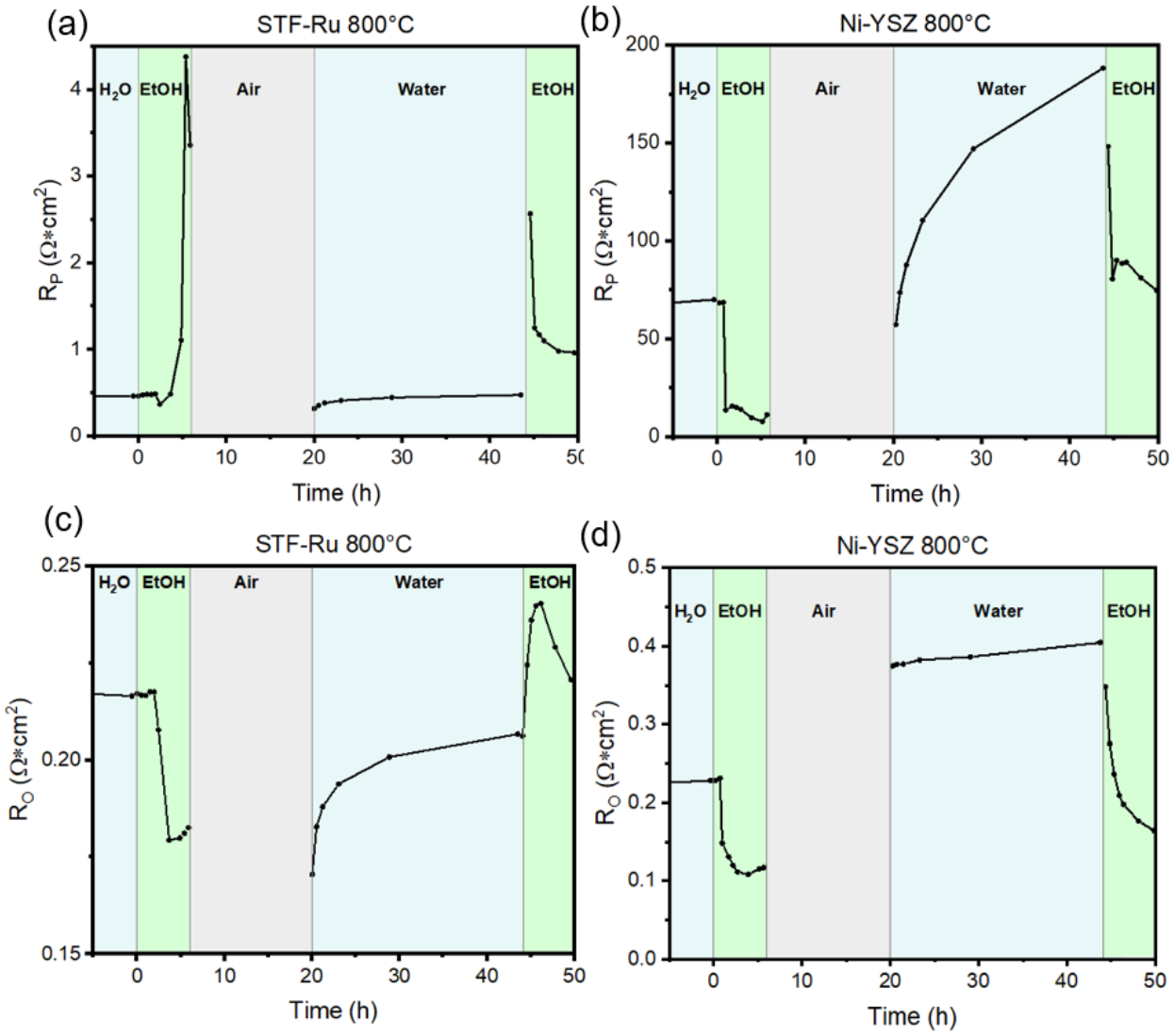

Figure 6.17 Impedance results of an accelerated coking experiment in which STFR and Ni/YSZ are subjected to hydrogen bubbled first through water, and then through anhydrous ethanol.

The above experiment utilized the dual-bubbler system described in Chapter 3 Section 3.3.3. This design allowed for the seamless transition from 3%-content steam to 6%-content ethanol vapor. The panels in Figure 6.17 above in blue show the measured resistances in the water configuration, and green in the ethanol configuration. The gray region represents the 24 h time period spent in air. The experiment was maintained at 800°C throughout. Prior to the cycling seen

above, the cells were maintained in the hydrogen/steam configuration for 100 h in order for their resistances to stabilize.

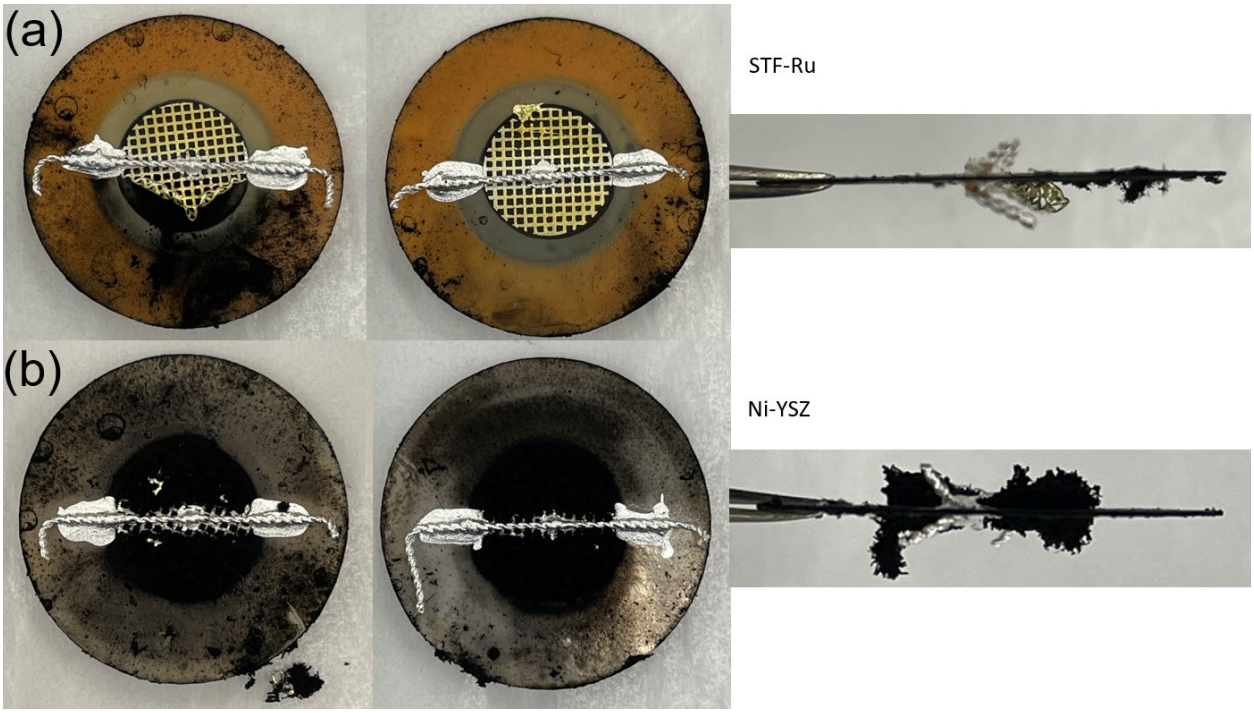

Figure 6.18 Post-mortem of (a) STFR and (b) Ni/YSZ after ramping down in a hydrogen 6% ethanol environment.

The cells were ramped down within the ethanol environment in order to observe the effect of carbon on the surfaces of the electrodes. Ni/YSZ developed significant carbon at just 6 h exposure to ethanol vapor. STFR notably only developed carbon in a single location, the point at which the fuel inlet was nearest the cell. The cells were setup in series with the fuel delivery tube terminating at where the gold is seen to have delaminated from the STFR in Figure 6.18(a).

Notable features of the experiment are as follows. Upon first exposure to ethanol, the polarization resistance of STFR increases sharply (fit in series with a resistor, inductor, and two RQ elements, as in the above STFN study). In contrast, R_P for Ni/YSZ, which was notable much larger to begin with due to the unoptimized processing of the cell, decreases. This can be explained

by the sharp decrease in pO_2 that would ensue with the loss of steam in the fuel mixture. Removing any source of water had the benefit of removing any chance of steam reforming of the solid carbon, ensuring rapid coking. However, such low pO_2 could only exacerbate the decomposition of STFR into Ruddlesden-Popper phase and Fe metal, again either in a BCC phase of its own, or alloyed with hexagonal Ru. Ni/YSZ, on the other hand, will not decompose in steam-less hydrogen. The improvement seen may even be due to the synergistic effect of solid carbon on the unoptimized microstructure if it allowed for increased electronic conduction in non-percolated segments. Ohmic resistance decreases for both cells; for Ni/YSZ this could again be due to the synergistic electronically-conductive carbon. For STFR, however, it can be explained by the increased n-type conductivity of the perovskite, assuming the effect extends to the Ruddlesden-Popper variant.[26]

After the oxidation cycle, STFR returns to a stable R_P and R_O that increase gradually over time, reminiscent of the above STFN experiments. The Ni/YSZ cell, however, immediately displays higher R_O consistent with disconnected Ni. The polarization resistance of the cell surprisingly begins at the last left-off value from the previous round in hydrogen/water, but soon takes off, eventually tripling in value; the reason is unknown.

The second exposure to ethanol is perhaps where the delamination of the gold current collector, seen in the post-mortem photographs, takes place, as it is otherwise difficult to explain why in this round, R_O increases for STFR when formerly in decreased. Delamination of the current collector is not seen like this under standard hydrogen operation. One possibility is that, upon switching from water to ethanol, enough water vapor was initially present in this area of the cell test setup that the highly endothermic steam reformation of carbon process occurred, dropping the temperature near the cell, and causing rapid interfacial strain.

The R_P of STFR behaves similarly, but a caveat is that with very little water present in the system to complete the reverse electrochemical reaction, the reported value of R_P is difficult to assert as an indicator of real performance. The behavior of the Ni/YSZ cell is largely the same as in its first ethanol exposure.

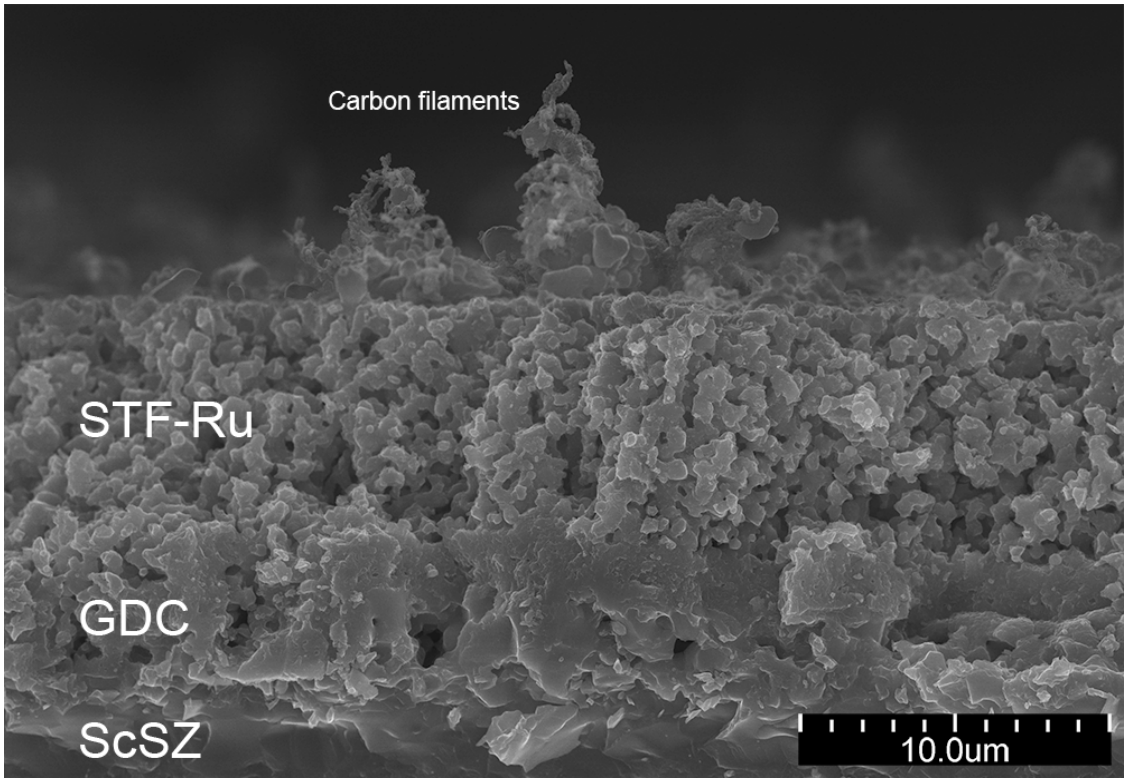

Figure 6.19 Carbon formation on the free surface of the post-mortem STFR cell. Image formed by two images of different focus to highlight in-plane both the cell and coke.

This set of experiments highlights the potential for perovskite electrodes in even extremely coking-prone conditions. Where carbon did form on STFR, as can be seen in the SEM micrograph in Figure 6.19 above, it consistently formed on the free surface, as opposed to within the pores where it would have hampered gas diffusion. No SEM micrographs were necessary with the extent of carbon formation with Ni/YSZ, as the photographs in Figure 6.18 capture the extent of the coke

formation. The redox-cyclability of STFR allows for nonzero coke formation given it can be effectively burned out without damaging the microstructure of the cell.

7 Viability of Vehicles with Solid Oxide Fuel Cells and Onboard Carbon Capture

This chapter has been adapted and expounded upon from the publication, "Viability of Vehicles Utilizing On-board CO_2 Capture" by T.A. Schmauss and S.A. Barnett.[135]

7.1 Abstract

Although battery electric and hydrogen fuel cell vehicles hold great promise for mitigating CO_2 emissions, there are still unaddressed sectors for electrified transport, e.g., the heavy-duty and long-range global shipping industry. In this Viewpoint, we examine the viability of CO_2-neutral transportation using hydrocarbon or alcohol fuels, in which the CO_2 product is captured on-board the vehicle. This approach takes advantage of the unparalleled energy density of carbon-based fuels as needed for these energy-intensive applications. A concept is developed considering the power technologies, infrastructure, and fuels required. Storage volume and mass requirements are calculated for a wide range of vehicle types and compared with those for other CO_2-neutral options, namely hydrogen fuel cell vehicles (H2FCVs) and battery electric vehicles (BEVs), and research and development needs to implement this technology are discussed.

7.2 Introduction

Significant inroads have been made in efforts to decarbonize transportation (globally, responsible for 22% of yearly anthropogenic CO_2), but commercialization has been mainly limited to light-duty, short-range vehicles, responsible for approximately half of the emissions from the sector.[4, 136] For this subsector, a recent Princeton report, *Net-Zero America* (NZA), which details a range of pathways to reach CO_2 neutrality by 2050, envisions rapid growth in the use of battery electric vehicles (BEVs) alongside major expansion in renewable electricity production.[136] The

majority of the remaining emissions in the sector arise from vehicles considered difficult to decarbonize, e.g., those for freight transport and aviation (4% and 2% of global CO_2, respectively). Here, sufficient battery capacity is problematic, and the NZA report instead proposes comparatively more scalable hydrogen to be utilized via fuel cell vehicles (H2FCVs).

Where practical, BEVs provide by far the best efficiency utilizing renewable electricity, ~77% delivered to wheels. For the remaining applications, H2FCVs with hydrogen derived from biomass gasification or electrolysis, the main production pathways as slated by the NZA report, are relatively inefficient, ~26% and 33% delivered to wheels, respectively.[136, 137] Such low efficiencies will be problematic because they require the production of much greater amounts of renewable energy upstream. Major hydrogen production and distribution infrastructure must already be in place before such vehicles are serviceable, with carbon-neutral processes eventually needing to take over market share. And while hydrogen offers impressive gravimetric specific energy, its low volumetric energy density is still a challenge, requiring energy-intensive compression to be feasible for most applications.

Here we assess a different approach, in which C-based fuels are used but with direct on-board CO_2 capture during operation. Shown schematically in Figure 7.1, efficiency is considerably improved over H2FCVs by avoiding the need to first convert such fuels to hydrogen. C-based fuels have the well-known advantage of markedly higher energy density than either compressed H_2 or Li-ion batteries; they also have an existing, well-developed distribution infrastructure. As shown in Figure 7.1, the CO_2 captured on vehicles could be returned to a CO_2 distribution network where, after sequestration, the cycle is CO_2-neutral for fossil fuels and CO_2-negative for biofuels. Another route, recycling the CO_2 back into fuel via electrolytic processes, is also possible.

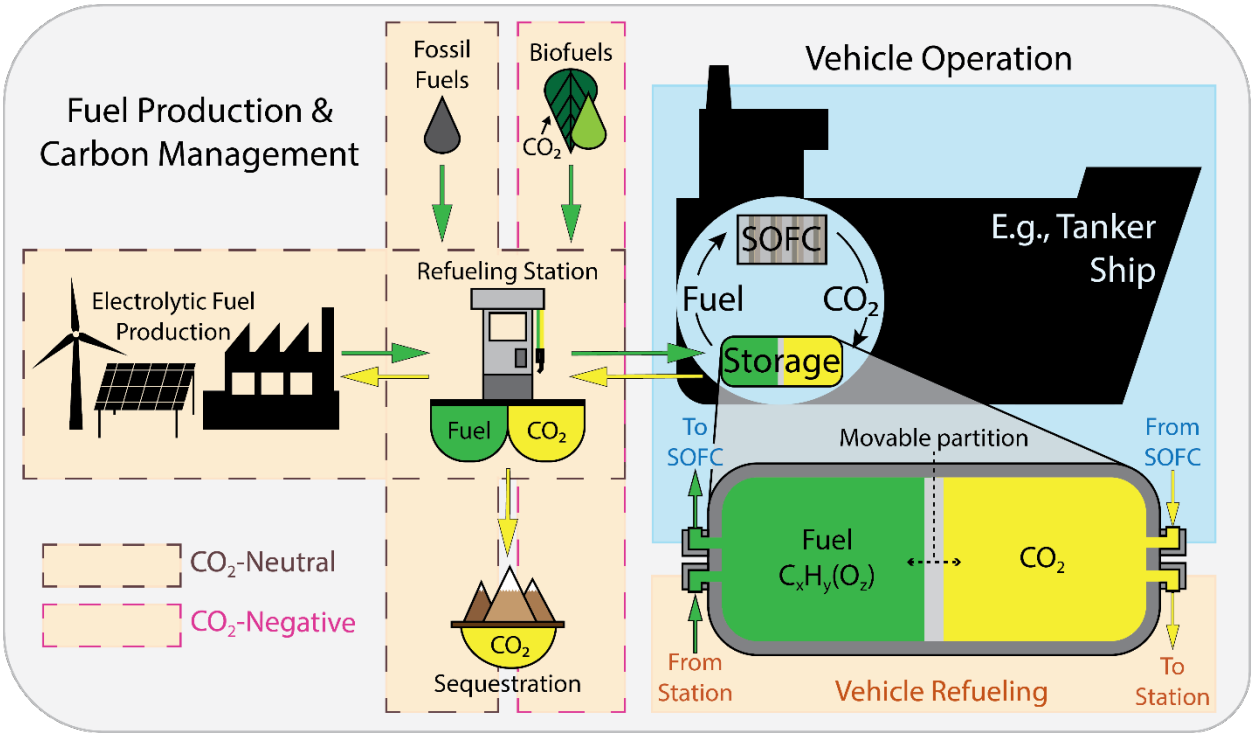

Figure 7.1 Schematic illustration of a Carbon Capture Fuel Cell Vehicle (CCFCV) and associated infrastructure. The vehicle includes a solid oxide fuel cell (SOFC) for efficient electrical generation from hydrocarbon or alcohol fuels. Fueling is with any of biofuels, fossil fuels, or electrolytic fuels produced using renewable electricity. The captured CO_2 can be stored in a separate tank or in a unified tank with a movable partition, as shown, to minimize net storage volume. After offloading, the CO2 can either be used in electrolytic fuel production or sequestered. Different infrastructure designs and fuel choices can yield an overall CO2 impact ranging from mitigatory to net negative.

The vehicle illustrated in Figure 7.1 is referred to here as a Carbon Capture Fuel Cell Vehicle (CCFCV). The solid oxide fuel cell (SOFC), shown in the vehicle inlay, is the most desirable choice for vehicle power generation with C-based fuels because it acts as a membrane air separator that combusts fuels with pure oxygen. This is necessary to maintain reasonable tank volumes – combustion with air would dilute the CO_2 with large amounts of nitrogen, and thus require prohibitively large tank volumes, which, due to differing gas densities, would be around 20 times that for CO_2 alone.[138] Although separate fuel and CO_2 tanks could be used, net volume requirements can be further reduced by storing the concentrated CO_2 product stream in the volume

made available by spent fuel, e.g., using a tank with a movable partition as illustrated in Figure 7.1. Note that the use of SOFCs as auxiliary power units, range extenders, or the primary power source in vehicles is already seeing rapidly growing interest.[139-142]

SOFCs are able to work with minimally-reformed hydrocarbon and alcohol fuels, while providing fuel-to-electricity conversion efficiency of 50–60%;[143] given a typical electric motor efficiency of 95%, the net fuel-to-wheels efficiency (47-57%) is substantially higher than for typical transportation heat engines (10–40%).[136] Assuming bioenergy-intensive pathways, the fuel flexibility of the SOFC allows it to operate on higher production efficiency biofuels (e.g., up to 85% for bioethanol)[144] versus biohydrogen (up to 60%)[137] resulting in net renewables-to-wheels efficiencies of ~44% for the CCFCV versus ~26% for H2FCVs. On the other hand, assuming high electrofuel pathways, the net renewables-to-wheels efficiency of the CCFCV and H2FCV are similar, but are substantially lower than for BEVs.[136]

One could argue that a similar carbon impact could be achieved with C-based fuels by simply releasing the CO_2 from internal combustion vehicles (ICEVs) and then using atmospheric CO_2 capture, but this process requires considerable resources – operating costs may eventually be as low as $200 per ton of CO_2, but cheap and abundant heat is needed, with prices approaching $1000/ton without.[145] Here, instead of release into the atmosphere, concentrated CO_2 will be captured; as discussed below, on-board compression of CO_2 introduces little energy efficiency or cost penalty.

It will be shown that this approach is viable for a variety of C-based fuels (7.3 C-Based Fuel and CO2 Storage Requirements), and has significant advantages for longer-range maritime and terrestrial applications for which H2FCVs are currently under consideration (7.4 Technology Comparisons across Vehicle Classes). Given existing C-based fuel infrastructure, rapid adoption

of such vehicles should be possible, and CO_2 emissions can be continuously decreased as new infrastructure for CO_2 conversion, collection, and/or distribution is built (7.5 Infrastructure, Phased Adoption, and CO2 Footprint). Specific technological challenges that will need to be engineered to address are discussed (7.6 Technological Challenges).

7.3 C-Based Fuel and CO_2 Storage Requirements

The volume required for the fuel and CO_2 can be assessed based on the known thermophysical properties of the fluids at elevated pressure. First, we consider the properties of compressed CO_2, shown in Figure 7.2(a). Note that the ambient-temperature density increases rapidly with increasing pressure up to 74 bar and reaches a value of 21 mol/L at 250 bar. This pressure, which is commonly used in compressed natural gas vehicles, is assumed in the analyses below, along with a higher value of 700 bar currently being used for hydrogen in H2FCVs. Also note that 250 bar is routinely reached with standard compressors and that the energy requirement is small, <2% of the energy released upon producing the CO_2. While higher pressure increases the gas density, it is likely not worth the required increases in pump size, compression energy, and tank reinforcement for most applications.

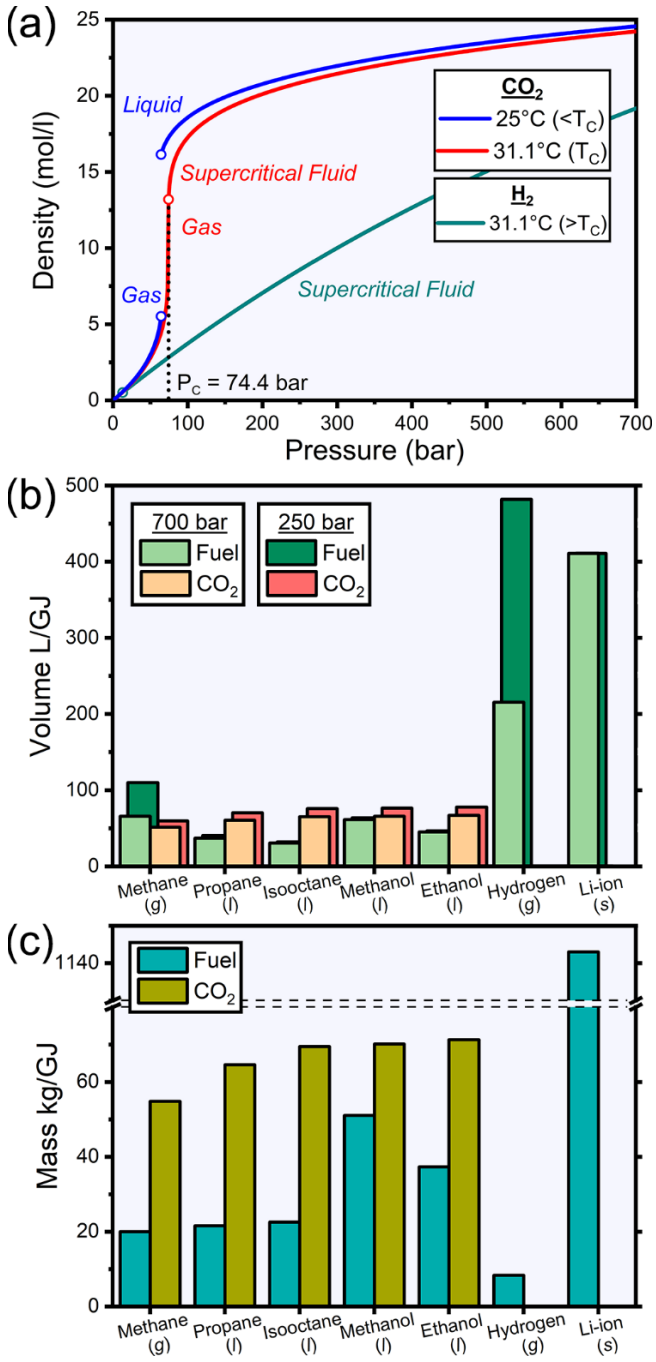

Figure 7.2 (a) Density of CO_2 versus pressure, at and below its critical temperature (T_C). A similar density is achieved past its critical pressure (P_C). H_2 is also shown for comparison, highlighting the relative ease of compressing CO_2. Comparison of the volumes (b) and masses (c) of different fuels corresponding to 1 GJ (lower heating value) of stored energy, and of the CO_2 produced by oxidation of the fuels. [Note: GJ is used as a convenient measure; 1 GJ corresponds to the energy in 31 L of gasoline, approximately the size of a small automobile's fuel tank.] Values are given for tank pressures of either 250 or 700 bar at 31.1 °C. Also shown are values for hydrogen and a representative Li-ion battery.

The CCFCV can function on a variety of fuels including hydrocarbons and alcohols. Figure 7.2(b) summarizes the requisite storage volumes yielding 1 GJ energy for several candidate fuels, and for the CO_2 produced by combusting the fuel, at both 250 and 700 bar. (Note that the water also produced by combustion would be easily separated from the CO_2 upon cooling the product.) The total volume for a given fuel and pressure can be reduced by utilizing a single adjustable tank versus separate fuel and CO_2 tanks (Table S1), from 30 to 48% depending on fuel and pressure. Considering ethanol, for example, a unified tank reduces storage volume by 38% at 250 bar. Even with separate tanks, a key advantage shown in Figure 7.2(b) is that storage volume can be substantially lower compared to hydrogen or batteries.

Figure 7.2(c) shows the fuel masses, 20–51 kg/GJ, and product CO_2 masses, 55–71 kg/GJ, with the latter being in some cases more than double that of the fuel. All are shown to be much lower than Li-ion battery mass, 1000–3000 kg/GJ,[146] but higher than for hydrogen, 8.3 kg/GJ. The increase in mass as fuel is converted is likely not an issue for most terrestrial applications; for example, the mass of a GJ worth of petroleum is ~23 kg and, in the example of a passenger vehicle, a typical GJ-sized tank would increase from ~1% to 2% of total vehicle mass. However, it may be problematic for large aircraft that are designed for low fuel mass upon touch-down.[147]

Table 7.1 Input parameters for Figure 7.2(b), a volumetric comparison between various hydrocarbon and alcohol fuels, as well as a representative Li-ion battery and hydrogen, at 31.1°C. (Note that for the most volume-sensitive applications, tank volume can be further decreased by employing a mixture of fuels that balance to be 1:1 volumetrically with their product CO_2. For example, at 250 bar, a mixture of 51% methane to 49% propane results in 65.0 l/GJ, versus the best single fuel, propane at 70.4 l/GJ. At 700 bar, 55%/45% methane/propane results in 55.6 l/GJ versus propane at 60.6 l/GJ. It may be beneficial to add a percentage of water to the higher C-number fuels in order to run on-board partial steam reformation. To this end, the fact that most of these fuels have volumes lower than their resulting CO_2 allows for penalty-free inclusion of a few percent H_2O content. One could also tailor a mixture if considering a specific utilization efficiency, as mentioned in the previous section.

Fuel[138, 148]	**Volume (l/GJ) 700 bar / 250 bar**				
	Fuel	**CO_2**	**Total (2 tanks)**	**Total (1 tank)**	**1 tank vs 2 (%)**
Methane (*g*)	65.8 / 109.8	51.4 / 59.7	117.2 / 169.5	65.8 / 109.8	-44 / -35
Propane (*l*)	37.2 / 40.4	60.6 / 70.4	97.8 / 110.8	60.6 / 70.4	-38 / -36
Isooctane (*l*)	30.7 / 31.9	65.2 / 75.7	95.9 / 107.6	65.2 / 75.7	-32 / -30
Methanol (*l*)	61.3 / 63.6	65.8 / 76.5	127.1 / 140.1	65.8 / 76.5	-48 / -45
Ethanol (*l*)	45.0 / 46.6	66.9 / 77.7	111.9 / 124.3	66.9 / 77.7	-40 / -37
Hydrogen (*g*)	215.4 / 482.0	*n/a*	*n/a*	215.4 / 482.0	*n/a*
Li-Ion Battery[149] (*s*)	410.9	*n/a*	*n/a*	410.9	*n/a*

Table 7.2 Input parameters for Figure 7.2(c), a gravimetric comparison between various hydrocarbon and alcohol fuels, as well as for a representative Li-ion battery and hydrogen.

Fuel[148]	**Mass (kg/GJ)**	
	Fuel	**CO_2**
Methane (*g*)	20.0	54.8
Propane (*l*)	21.6	64.6
Isooctane (*l*)	22.7	69.9
Methanol (*l*)	51.1	70.2
Ethanol (*l*)	37.3	71.3
Hydrogen (*g*)	8.3	*n/a*
Li-Ion Battery[149] (*s*)	1143	*n/a*

7.4 Technology Comparisons across Vehicle Classes

To meaningfully assess how CCFCV volume and weight compare with those of other power systems, they must be considered within the context of specific vehicle types. Figure 3

summarizes CCFCV characteristics versus those of ICEVs, H2FCVs and BEVs, using as examples tanker ships and passenger vehicles to represent heavy-duty and light-duty cases, respectively.

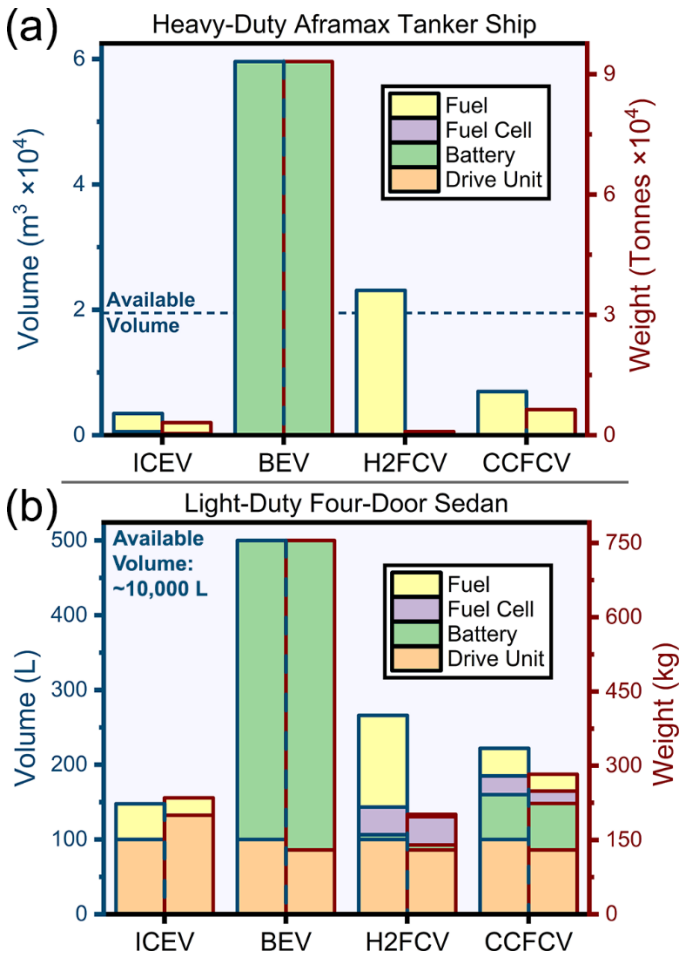

Figure 7.3 Volume (bars outlined in blue) and weight (bars outlined in red) of the vehicle power system for ICEVs, BEVs, H2FCVs, and CCFCVs with ethanol and 250 bar storage. (a) shows the case of a medium-sized tanker ship (e.g., Wärtsilä WSD42 111K). (b) shows a light-duty sedan of ~500 km range (e.g., Toyota Mirai and Tesla Model S); For (a), the stored energy is by far the predominant portion of total power system weight and volume.

Figure 7.3(a) shows the power system volume and weight of a tanker ship, a case where the long vehicle range requires a large amount of stored energy. The figure clearly illustrates the challenge for both BEVs and H2FCVs – because of their relatively low energy storage densities, the battery or fuel volume exceeds the available volume, i.e., that which is not dedicated to the cargo. The CCFCV, on the other hand, is clearly a viable path to decarbonized long-range shipping,

although the storage volume is ~2x larger versus the incumbent ICEV. SOFC-powered tankers are already under development,[140, 141] and their conversion to CCFCVs could therefore be more direct than other vehicle classes.

Figure 7.3(b) represents the other end of the vehicle spectrum, a light-duty sedan. CCFCV and H2FCV energy systems require reasonably low percentages of total vehicle volume and weight, comparable to ICEVs. Although BEVs have substantially larger requirements, they are still acceptable considering their other advantages, especially their high efficiency when utilizing renewable electricity. All three electrified cases see a substantial fraction of power system volume going to the drive unit (motor, inverter, and differential), and all three contain a battery of differing size for, at minimum, start-up and regenerative braking. A key benefit of the CCFCV, its ability to use high energy density fuel, is not as impactful for this class of vehicle with its lower energy storage requirement. [Note: However, there are other advantages of the CCFCV configuration here, essentially one in which an SOFC serves as a range extender for a BEV.[139] This design features a substantial reduction in battery pack size compared to full BEVs that could be important for reducing the materials resources required to electrify all light-duty vehicles by 2050.[150] The smaller battery makes optimal high-efficiency use of renewable electricity for most travel—short-range trips—whereas for longer-range trips the fuel cell is arguably the highest-efficiency means to utilize C-based fuels.]

The above examples broadly represent the array of light- and heavy-duty transportation vehicles; one can expect medium and heavy-duty land vehicles including trains, semitrucks, and buses to have characteristics somewhere between those shown in Figures 3a and 3b. The larger the energy requirement, the more favorable the CCFCV should be compared to BEVs and H2FCVs.

Table 7.3 Input parameters for volumetric and gravimetric calculations of four simplified power systems in an Aframax-class tanker ship, shown in Figure 3a, based on the Wärtsilä WSD 42 111K.[151] Heavy fuel oil is used as the fuel for the ICEV. The H2FCV is taken to run on 700 bar hydrogen, and the CCFCV on 250 bar ethanol. For the fuel cell vehicles, fuel cell and drive unit volume and weight are taken as the automotive examples in subsequent Table 7.4 scaled by the increased power of the ship. Unlike for the sedan, weight and volume of a supplementary battery to the fuel cell systems are not considered here given the more constant duty cycle of a tanker, i.e., in the absence of instantaneous changes in power like for regenerative braking.

Aframax Tanker Ship (Wärtsilä WSD 42 111K)				
Vehicle Details	**ICEV Details**	**BEV Details**	**H2FCV Details**	**CCFCV Details**
Total Volume	**Efficiency**	**E.chem Efficiency**	**E.chem Efficiency**	**E.chem Efficiency**
136,000 m^3	46 %[152]	~100 %[153]	50 %[154]	60 %[154]
Non-Cargo Volume	**Heavy Fuel Oil**	**Motor Efficiency**	**Motor Efficiency**	**Motor Efficiency**
~1/7 Total	38.2 MJ/l[155]	95 %[156]	95 %[156]	95 %[156]
19,500 m^3	40.0 MJ/kg[155]	**LIB**	**PEMFC**	**SOFC**
Weight	110,800 GJ	0.90 $GJ/m^{3(157)}$	3.1 $MW/m^{3(158)}$	~1 MW/m^3
100,970 t	2,900 m^3	0.576 GJ/t[157]	2 MW/t[158]	~1 MW/t
Range	2,770 t	53,600 GJ	10.4 MW	10.4 MW
27,800 NM	**Engine**	59,600 m^3	3.4 m^3	10.4 m^3
	10.4 MW	93,100 t	5.2 t	10.4 t
	570 $m^{3(159)}$	**Drive Unit**	**Hydrogen**	**Ethanol/CO_2**
	377 t[159]	~2.6 $m^{3(160)}$	4.64 GJ/m^3	12.9 GJ/m^3
		~3.4 t[160]	120 GJ/t	15.5 GJ/t
			107,000 GJ	89,400 GJ
			23,100 m^3	6,950 m^3
			894 t	6,380 t
			Drive Unit	**Drive Unit**
			~2.6 $m^{3(160)}$	~2.6 $m^{3(160)}$
			~3.4 t[160]	~3.4 t[160]

Table 7.4 Input parameters for volumetric and gravimetric calculations of four simplified power systems in a four-door sedan, shown in Figure 3b. The miles-per-gallon-equivalent (MPGe) of the CCFCV is estimated as the 2020 Toyota Mirai H2FCV MPGe multiplied by a factor representing the increase in fuel-to-electrical energy efficiency of SOFCs/PEMFCs (60%/50%).[154] For the CCFCV, the fuel cell maximum power output is taken to be 25 kW as needed for highway driving, whereas the hybrid battery pack is taken to be 15 kWh, sufficient to provide an ~60 km electric-only range. The packaged BEV battery (i.e., including active and inactive material) is taken to be 100 kWh (e.g., 2019 Tesla Model S P100D). Batteries for the H2FCV and CCFCV borrow the energy density and specific energy of the packaged Tesla battery for ease of comparison (despite, for example, that year's model of the Mirai using a nickel-metal hydride battery). The H2FCV is taken to run on 700 bar hydrogen, and the CCFCV on 250 bar ethanol (the tank volume and weight set by the product CO_2).

Four Dour Sedan (Based on the Tesla Model S P100D and Toyota Mirai)				
Vehicle Details	**ICEV Details**	**BEV Details**	**H2FCV Details**	**CCFCV Details**
Total Volume	**Fuel Economy**	**Fuel Economy**	**Fuel Economy**	**Fuel Economy**
~10,000 l	~25 MPG[161]	98 MPGe[162]	67 MPGe[158]	~80 MPGe
Total Weight	**Gasoline**	**LIB**	**PEMFC**	**SOFC**
~1,700 kg	8.9 kWh/l[162]	250 Wh/l[157]	3.1 kW/l[158]	~1 kW/l
Range	0.7 kg/l[163]	160 Wh/kg[157]	2 kW/kg[158]	~1 kW/kg
315 miles[158, 164]	47.7 l	100 kWh[157]	114 kW[165]	25 kW[166]
507 km	35.2 kg	400 l	36.8 l	~25 l
	Engine	625 kg	57 kg	~25 kg
	~100 l	**Drive Unit**	**LIB**	**LIB**
	~200 kg	~100 l[160]	1.6 kWh[165]	~15 kWh
		~130 kg[160]	6.4 l	~60 l
			10 kg	~93.8 kg
			Hydrogen	**Ethanol/CO_2**
			1.3 kWh/l	3.6 kWh/l
			33.3 kWh/kg	3.9 kWh/kg
			123 l	36.9 l
			4.8 kg	33.9 kg
			Drive Unit	**Drive Unit**
			~100 l[160]	~100 l[160]
			~130 kg[160]	~130 kg[160]

7.5 Infrastructure, Phased Adoption, and CO_2 Footprint

Early-stage infrastructure requirements for adoption of CCFCVs can be much less obtrusive than for BEVs and H2FCVs. The proposed transportation platform can be implemented

in stages, as outlined below, with little initial need for new infrastructure before widespread introduction. As more vehicles come online, and infrastructure catches up, the overall CO_2 footprint improves from mitigatory, to neutral, and finally to potentially net negative.

The initial focus can be on the vehicles themselves, primarily incorporating SOFCs with high power density that can work with various fuels. Work here is already underway, with shipbuilders having recently announced partnerships with SOFC manufacturers to electrify tankers.[140, 141] At this stage, legacy fuel infrastructure can be used, and refueling times are akin to those of ICEVs and H2FCVs. Here, the shift from internal combustion engines to SOFCs will reduce CO_2 emissions by way of higher fuel efficiency. CO_2 storage on-board the vehicle can subsequently be implemented, even if the corresponding CO_2 collection/distribution infrastructure is not yet widely available. At a later stage of infrastructure development, implementation of CO_2 sequestration and/or utilization[167] can then be realized (note that local distribution could be done relatively inexpensively by retrofitting fuel supply vehicles so that they can return compressed CO_2 to centralized sites). Importantly, with the above strategy the *catch-22* of needing both infrastructure and vehicles for market penetration, a major detriment to H2FCVs and to a lesser extent BEVs, is avoided.

At all stages, fuel provenance is important because it helps determine the utilization efficiency and the amount of CO_2 released or captured. Even without CO_2 capture, the carbon footprint can be substantially decreased by shifting from fossil to bio- and electrofuels (and their production can also help alleviate renewable electricity curtailment by being produced during times of grid oversupply). Biofuels may be more desirable, given they can be produced with high efficiency (up to ~85%)[144] and have the potential to be net negative upon the introduction of any level of CO_2 sequestration.[143] On the other hand, carbon-neutral electrofuels, while less efficient

to produce (~76%),[136] have the advantage of locally closing the carbon loop – that is, by equipping fueling stations with electrolysis and fuel production capabilities to utilize CO_2 on-site. If nothing else, fossil fuels could still be conceivably made net neutral were complete sequestration to be implemented.[167]

7.6 Technological Challenges

Although there appear to be no major "show-stoppers" regarding the engineering demands for the CCFCV, the following will need to be addressed during development. An overall schematic showing the ensemble of components necessary is shown in Figure 7.4.

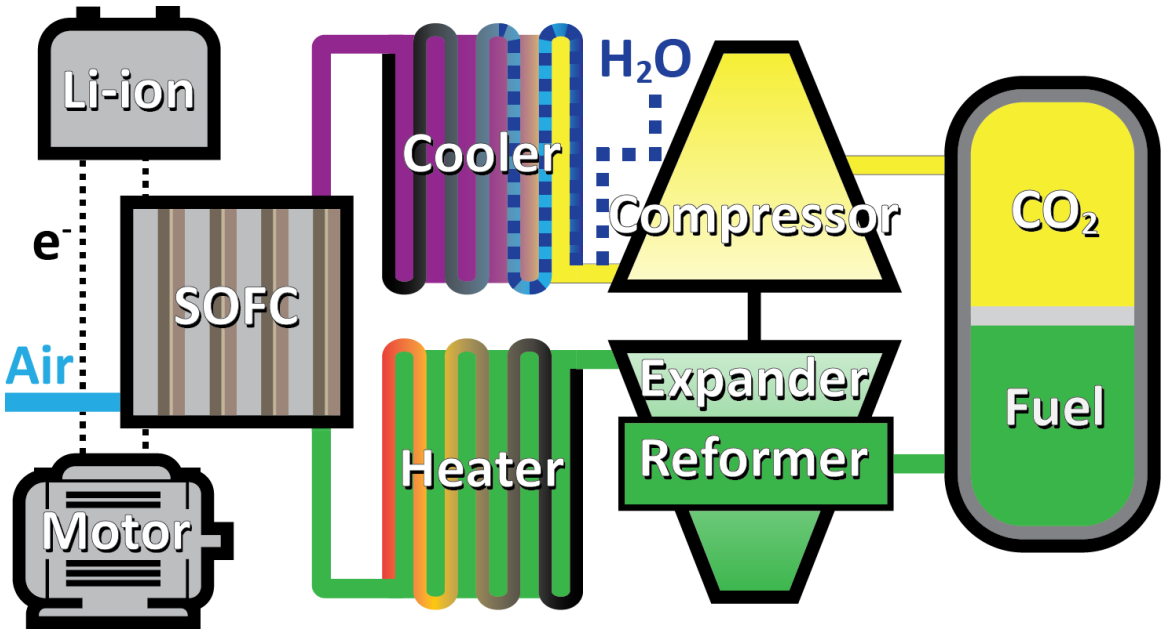

Figure 7.4 Schematic diagram of the proposed carbon capture fuel cell vehicle (CCFCV) energy conversion system. In this depiction, the SOFC is integrated with a LIB, as would be particularly advantageous for managing the variable load of smaller vehicle classes – this approach has been proposed both with low-temperature fuel cells[168-173] and SOFCs,[166, 174, 175] and provides several advantages. In the hybrid system, the SOFC provides a fairly steady power output at the average value required by the vehicle, effectively range-extending the battery. A battery pack that is small by BEV standards then provides the relatively high power required for acceleration (and for terrestrial vehicles, rapid charging during regenerative braking). In larger and steadier-power vehicles, the relative size of the LIB in the power system can be decreased or eliminated completely so long as initial SOFC startup is externally powered (e.g., via the grid).

7.6.1 Dual-chamber, pressurized tank

While safe, lightweight, high pressure tanks have been developed for use in natural gas vehicles and H2FCVs, it will be necessary to modify these with a fuel partition, most likely a flexible membrane or sliding piston. The partition will need to form a robust gas seal, and the partition material will have to be chemically stable with respect to CO_2 and fuel. Despite 250 bar or greater storage pressures, the partition and seal will only experience a negligible differential because fluids on either side will be maintained at the same pressure.

7.6.2 CO_2 compressor

Note that the size, cost, and energy requirement of compressors that reach 700 bar is expected to be substantially more than that for 250 bar. Given the relatively modest decreases in tank volume that are achieved by going to the higher pressure (except for the case of methane), 250 bar appears to be a good choice. Compressors that reach 250 bar are commercially available, compact, light-weight, and cost-effective. Typical capacity is 50 l/min, corresponding to the amount of CO_2 produced by an ~1 MW SOFC operated on methane. For the much smaller 25 kW SOFC suggested for a light-duty vehicle, a ~1 l/min compressor could be used. Further development will be useful to match size to the vehicle power requirement, improve long-term reliability, and reduce noise levels. In a case where the fuel is CH_4, a combined compressor/expander could be utilized to take advantage of the energy of expansion of the fuel to help offset compression.[176]

7.6.3 Thermal integration

The vehicle energy conversion components (Figure S1) will need to be thermally integrated in order to achieve a compact, efficient system. Heat from the SOFC exhaust (both fuel exhaust and spent air) should be used to help pre-heat incoming gases in a recuperative heat exchanger,

whereas the heat of compression can be used to offset the cooling that occurs from fuel expansion or evaporation. Thermal integration of the energy system with the vehicle cabin should also be done. That is, excess SOFC heat can be utilized for passenger compartment heating and, potentially, for cooling via an adsorption chiller;[177] this has the potential to decrease parasitic electrical requirements and thereby improve overall efficiency.

7.6.4 SOFC development and manufacturing

Although SOFCs are already undergoing early-stage commercialization, availability must be increased and costs reduced by economies of scale. Furthermore, technology development is needed to increase power density to meet the needs of vehicular applications. Although SOFCs are believed to have potential for very high power density,[178] development has been done primarily for stationary power applications. Thus, there has been little focus on achieving the high power densities (~3kW/l) achieved by low temperature hydrogen fuel cell technology.[179] Another issue is the use of the different C-based fuels mentioned above. SOFCs are most commonly used with methane, for which it is not necessary to completely reform the fuel to hydrogen. Indeed, partial methane on-cell reforming is beneficial for thermal balancing and providing high efficiency.[180] There are examples of direct operation of SOFCs on fuels including methane,[181-183] ethanol,[184] propane,[185] butane,[186] and gasoline,[187] but most likely an external reformer would be utilized to at least partially convert the fuel into a hydrogen- and methane-rich mixture prior to introduction into the SOFC in order to avoid coking.[188] Finally, a potential issue is the ceramic nature of SOFCs, and possible concerns that cell fracture could result from the vibrations and shocks during vehicle operation. While there is not extensive information available this topic, there has been considerable development of SOFCs for an auxiliary power unit in vehicles, with no apparent issues in this regard.[189, 190] It is likely that the SOFC stack can be mounted so as to sufficiently shield it from

shock and vibrations. On this note, there has been rapid development of metal-supported SOFCs that would certainly be sufficiently robust for transportation applications.[51, 191-193]

7.6.5 Matching duty cycles

Vehicles have duty cycles that are inherently intermittent. Rapid load variations during vehicle operation can be followed using a battery pack, while the SOFC operates at a steadier power level for base power and to keep the battery charged. The problem for SOFCs arises when there are long periods of vehicle inactivity; because of their high operating temperature, SOFCs are usually not amenable to frequent, quick start-ups and shut-downs. This is less of a problem for fleet and long-haul vehicles that operate regularly, but could be a serious issue for infrequently-used light-duty vehicles. The relatively long start-up time may not be problematic from an automobile user perspective because the vehicle can first be operated using battery power only, a common measure for plug-in hybrid automobiles where 10–20 kWh battery packs typically yield a 30–70 km battery-only range. However, frequent on/off cycles are not desirable from an efficiency standpoint because of the substantial energy required to heat the stack, and because they may lead to SOFC performance degradation, although the aforementioned metal-supported cells show promise in this regard.

Various strategies could be used to keep the SOFC operating much of the time, and thereby minimize the frequency of on/off cycles. For example, the SOFC can continue to operate between trips in order to re-charge the battery and can extend the charging time by working at a fraction of its maximum power output (of particular benefit for long-haul trucking in which “hotel loads” occur during overnight stays within the cab). Furthermore, the vehicle can be grid-connected when not in use; while this is currently done with BEV charging, in the CCFCV case the vehicle would supply electricity to the grid.[194] (Note that SOFCs are also being developed that can operate

reversibly,[195, 196] i.e., to convert electricity to fuel, such that they could also potentially assist with generating fuel when the grid has excess renewable electricity.)

7.6.6 Fuel and exhaust composition

In section 2, it was considered for simplicity that SOFCs produce pure H_2O-CO_2, but the exhaust in fact contains small amounts of other species. Typical fuel utilization for fuel cells is 80–90%, such that there is 10–20% residual H_2 and a smaller amount of CO in the fuel exhaust. In a conventional SOFC system, these residuals are combusted. In the proposed approach, they will be pressurized and stored together with the CO_2 – the residual amounts are small enough that they do not significantly impact the overall CO_2 storage capacity (e.g., an 80% CO_2 / 19% H_2 / 1% CO mixture yields a density of 16.4 mol/L versus 20.9 mol/L for pure CO_2 at 250 bar at 31.1°C). Prior to permanent sequestration, the excess H_2 and CO would presumably be combusted. Alternatively, since this feedstock can be used for renewable fuel production rather than being combusted, overall efficiency can be improved. One likely approach is hydrogen production in alkaline or proton-exchange-membrane electrolyzers, where a subsequent catalytic reaction with the CO_2 is used to produce syngas (H_2 + CO) and then the desired renewable fuel.[197, 198] There is clearly no problem with using the H_2 and CO-containing CO_2 in these catalytic processes. Another possibility is solid oxide electrolysis, in which it is possible to do CO_2-H_2O co-electrolysis, and it is actually desirable to have some H_2 and CO present in the input gas to avoid oxidation of the fuel electrode.[196, 199]

7.7 Summary and Future Outlook

This chapter establishes the concept of a Carbon Capture Fuel Cell Vehicle, starting from the premise of leveraging the high energy density of C-based fuels with the point source capture of CO_2 from solid oxide fuel cells. The fuels, captured carbon, and power system are compared

against Li-ion battery and hydrogen vehicles over a vehicle size class spectrum; the case for the CCFCV becomes increasingly compelling for vehicles with higher energy storage requirements. This is arguably the only viable CO_2-neutral approach for long-range freight vehicles (4% of global emissions) given the unmanageably large hydrogen tank or battery size/mass that would otherwise be needed for their operation. Therefore, vehicles operated on bio-, electro-, or fossil-fuels with on-board CO_2 capture could provide an important complement to hydrogen fuel cell and battery electric vehicles for energy-intensive vehicles. The approach is flexible and can be implemented in stages, first incorporating fuel cells and then CO_2 capture into vehicles, while developing infrastructure options to yield reduced or even negative emissions.

Of course, numerous technical, financial, and policy challenges must be surmounted to realize this technology. Regarding the vehicle itself, the proposed relies on reasonably well-developed technologies, but further refinement is needed for their integration into vehicles. Detailed cost analyses are needed; qualitatively speaking, SOFCs are currently more expensive than the proton-exchange membrane fuel cells used in H2FCVs, but should become more comparable as SOFC manufacturing ramps up, especially given that SOFCs do not utilize precious metals.[9, 142] Increasing stack lifetime is arguably the most important SOFC R&D task; it has been shown to be a determining factor in the implementation of SOFCs in ships.[142] SOFCs have been mainly developed for stationary power generation, but development towards higher power density stacks will be useful given vehicle space limitations. Additionally, while SOFCs already work well with natural gas and hydrogen, development of fuel processors for other fuels such as ethanol is needed. Finally, while storage of compressed gases on vehicles is already utilized for natural gas and hydrogen, and the pressures required for CO_2 storage are relatively low, the development of compact, light-weight on-board compressors will be important.

Techno-economic analysis will be required to identify the specific fuel choices and carbon sequestration/utilization options that, depending on the available local infrastructure, can realize the deepest reductions. Similar analysis is already ongoing to enable the decarbonization of other sectors.[136] While costs have been assessed for CO_2 distribution from fixed sources,[200] realistic cost estimates for the proposed CCFCV platform may be higher. Qualitatively, CO_2 storage and distribution infrastructure should be more cost effective than hydrogen because of the lower compression requirements and elimination of materials embrittlement issues.

Although the above challenges are significant, so too are those for the multitude of technologies needed to reach net-zero emissions in other sectors. The proposed on-board CO_2 capture approach is a viable path towards decarbonization of energy-intensive land and sea transportation, and is arguably the most reasonable option in some cases.

References

1. D. Wallace-Wells, *The Uninhabitable Earth: Life After Warming*, Tim Duggan Books, New York, First edition. edn., 2019.
2. K. S. Robinson, *The Ministry for the Future*, Orbit, New York, NY, First edition. edn., 2020.
3. BP, *Statistical Review of World Energy 70th Edition*, 2021.
4. S. J. Davis, N. S. Lewis, M. Shaner, S. Aggarwal, D. Arent, I. L. Azevedo, S. M. Benson, T. Bradley, J. Brouwer, Y. M. Chiang, C. T. M. Clack, A. Cohen, S. Doig, J. Edmonds, P. Fennell, C. B. Field, B. Hannegan, B. M. Hodge, M. I. Hoffert, E. Ingersoll, P. Jaramillo, K. S. Lackner, K. J. Mach, M. Mastrandrea, J. Ogden, P. F. Peterson, D. L. Sanchez, D. Sperling, J. Stagner, J. E. Trancik, C. J. Yang and K. Caldeira, *Science*, 2018, **360**.
5. M. Flottenkommando, *Annual Report 2021: Facts and figures on the maritime dependency of the Federal Republic of Germany*, Bundeswehr, 2021.
6. IPCC, *Climate Change 2014: Mitigation of Climate Change. Contribution of Working Group III to the Fifth Assessment Report of the Intergovernmental Panel on Climate Change*, Report 110705821X, 2014.
7. Z. Li, M. S. Pan, L. Su, P.-C. Tsai, A. F. Badel, J. M. Valle, S. L. Eiler, K. Xiang, F. R. Brushett and Y.-M. Chiang, *Joule*, 2017, **1**, 306-327.
8. E. D. Wachsman and K. T. Lee, *Science*, 2011, **334**, 935-939.
9. M. M. Whiston, I. M. L. Azevedo, S. Litster, C. Samaras, K. S. Whitefoot and J. F. Whitacre, *Joule*, 2019, **3**, 2060-2065.
10. M. Y. Lu, Doctor of Philosophy Dissertation, Northwestern University, 2019.
11. R. P. O'Hayre, S.-W. Cha, W. G. Colella and F. B. Prinz, *Fuel cell fundamentals*, Wiley, Hoboken, New Jersey, Third edition. edn., 2016.
12. S. P. Jiang, *Journal of The Electrochemical Society*, 2017, **164**, F834-F844.
13. S. Dierickx, A. Weber and E. Ivers-Tiffée, *Electrochimica Acta*, 2020, **355**, 136764.
14. M. E. Orazem and B. Tribollet, *Electrochemical impedance spectroscopy*, Wiley, Hoboken, New Jersey, 2nd edition. edn., 2017.
15. Z. Gao, L. V. Mogni, E. C. Miller, J. G. Railsback and S. A. Barnett, *Energy & Environmental Science*, 2016, **9**, 1602-1644.
16. Y. Zhang and J. D. Nicholas, *Journal of The Electrochemical Society*, 2021, **168**, 034513.
17. T. O. L. Sunde, T. Grande and M.-A. Einarsrud, in *Handbook of Sol-Gel Science and Technology*, eds. L. Klein, M. Aparicio and A. Jitianu, Springer International Publishing, Cham, 2016, DOI: 10.1007/978-3-319-19454-7_130-1, pp. 1-30.
18. A. V. Call, J. G. Railsback, H. Wang and S. A. Barnett, *Phys Chem Chem Phys*, 2016, **18**, 13216-13222.
19. M. Y. Lu, R. Scipioni, B.-K. Park, T. Yang, Y. A. Chart and S. A. Barnett, *Materials Today Energy*, 2019, **14**, 100362.
20. D. Sarantaridis and A. Atkinson, *Fuel Cells*, 2007, **7**, 246-258.
21. P. I. Cowin, C. T. G. Petit, R. Lan, J. T. S. Irvine and S. Tao, *Advanced Energy Materials*, 2011, **1**, 314-332.
22. T. L. Zhu, H. E. Troiani, L. V. Mogni, M. F. Han and S. A. Barnett, *Joule*, 2018, **2**, 478-496.

23. L. Shu, J. Sunarso, S. S. Hashim, J. Mao, W. Zhou and F. Liang, *International Journal of Hydrogen Energy*, 2019, **44**, 31275-31304.
24. N. Mahato, A. Banerjee, A. Gupta, S. Omar and K. Balani, *Progress in Materials Science*, 2015, **72**, 141-337.
25. M. Bilal Hanif, M. Motola, S. qayyum, S. Rauf, A. khalid, C.-J. Li and C.-X. Li, *Chemical Engineering Journal*, 2022, **428**.
26. A. Rothschild, W. Menesklou, H. L. Tuller and E. Ivers-Tiffée, *Chemistry of Materials*, 2006, **18**, 3651-3659.
27. J. Wang, K. Syed, S. Ning, I. Waluyo, A. Hunt, E. J. Crumlin, A. K. Opitz, C. A. Ross, W. J. Bowman and B. Yildiz, *Advanced Functional Materials*, 2021, **32**.
28. D. Neagu, V. Kyriakou, I. L. Roiban, M. Aouine, C. Tang, A. Caravaca, K. Kousi, I. Schreur-Piet, I. S. Metcalfe, P. Vernoux, M. C. M. van de Sanden and M. N. Tsampas, *ACS Nano*, 2019, **13**, 12996-13005.
29. T. L. Zhu, H. Troiani, L. V. Mogni, M. Santaya, M. F. Han and S. A. Barnett, *J Power Sources*, 2019, **439**.
30. Y. Sun, J. Li, Y. Zeng, B. S. Amirkhiz, M. Wang, Y. Behnamian and J. Luo, *J Mater Chem A*, 2015, **3**, 11048-11056.
31. D. Neagu, G. Tsekouras, D. N. Miller, H. Ménard and J. T. S. Irvine, *Nature Chemistry*, 2013, **5**, 916-923.
32. A. Yaqub, N. K. Janjua, C. Savaniu and J. T. S. Irvine, *International Journal of Hydrogen Energy*, 2015, **40**, 760-766.
33. P. W. Voorhees, *Journal of Statistical Physics*, 1985, **38**, 231-252.
34. O. Fuel Cell Technologies, *U.S. Department of Energy*, 2016, **2015**, 1-58.
35. B. Koo, K. Kim, J. K. Kim, H. Kwon, J. W. Han and W. Jung, *Joule*, 2018, **2**, 1476-1499.
36. H. Wang, K. J. Yakal-Kremski, T. Yeh, G. M. Rupp, A. Limbeck, J. Fleig and S. A. Barnett, *Journal of The Electrochemical Society*, 2016, **163**, F581-F585.
37. W. Lee, J. W. Han, Y. Chen, Z. Cai and B. Yildiz, *J Am Chem Soc*, 2013, **135**, 7909-7925.
38. G. M. Rupp, A. K. Opitz, A. Nenning, A. Limbeck and J. Fleig, *Nat Mater*, 2017, **16**, 640-645.
39. C. M. Harrison, P. R. Slater and R. Steinberger-Wilckens, *Solid State Ionics*, 2020, **354**, 115410.
40. J. Hong, S. J. Heo, A. N. Aphale, B. Hu and P. Singh, *Journal of The Electrochemical Society*, 2019, **166**, F59-F65.
41. E. F. Kukovitsky, S. G. L'Vov, N. A. Sainov, V. A. Shustov and L. A. Chernozatonskii, *Chemical Physics Letters*, 2002, **355**, 497-503.
42. D. K. Niakolas, *Applied Catalysis A: General*, 2014, **486**, 123-142.
43. F. Wang, H. Kishimoto, T. Ishiyama, K. Develos-Bagarinao, K. Yamaji, T. Horita and H. Yokokawa, *J Power Sources*, 2020, **478**, 228763.
44. H. J. T. Ellingham, *Journal of the Society of Chemical Industry*, 1944, **63**, 125-160.
45. F. D. Richardson and J. H. E. Jeffes, *Journal of the Iron and Steel Institute*, 1948, **160**, 261-&.
46. M. S. Khan, S.-B. Lee, R.-H. Song, J.-W. Lee, T.-H. Lim and S.-J. Park, *Ceramics International*, 2016, **42**, 35-48.

47. V. V. Kharton, F. M. B. Marques and A. Atkinson, *Solid State Ionics*, 2004, **174**, 135-149.
48. B.-K. Park, R. Scipioni, Q. Zhang, D. Cox, P. W. Voorhees and S. A. Barnett, *J Mater Chem A*, 2020, **8**, 11687-11694.
49. T. Yang, S. L. Kollasch, J. Grimes, A. Xue and S. A. Barnett, *Applied Catalysis B: Environmental*, 2022, **306**, 121114.
50. S. L. Zhang, H. Q. Wang, T. R. Yang, M. Y. Lu, C. X. Li, C. J. Li and S. A. Barnett, *J Mater Chem A*, 2020, **8**, 25867-25879.
51. E. Dogdibegovic, R. F. Wang, G. Y. Lau and M. C. Tucker, *J Power Sources*, 2019, **410**, 91-98.
52. B.-K. Park, J.-W. Lee, S.-B. Lee, T.-H. Lim, S.-J. Park, R.-H. Song and D.-R. Shin, *J Power Sources*, 2012, **213**, 218-222.
53. S. M. George, *Chem Rev*, 2010, **110**, 111-131.
54. A. S. Yersak, K. Sharma, J. M. Wallas, A. A. Dameron, X. Li, Y. Yang, K. E. Hurst, C. Ban, R. C. Tenent and S. M. George, *Journal of Vacuum Science & Technology A: Vacuum, Surfaces, and Films*, 2018, **36**.
55. T. M. Onn, R. Kungas, P. Fornasiero, K. Huang and R. J. Gorte, *Inorganics*, 2018, **6**, 34.
56. I. J. Raaijmakers, *ECS Transactions*, 2011, **41**, 3-17.
57. T. Keuter, G. Mauer, F. Vondahlen, R. Iskandar, N. H. Menzler and R. Vaßen, *Surface and Coatings Technology*, 2016, **288**, 211-220.
58. B.-K. Park, R. Scipioni, D. Cox and S. A. Barnett, *J Mater Chem A*, 2020, **8**, 4099-4106.
59. M. D. Groner, F. H. Fabreguette, J. W. Elam and S. M. George, *Chemistry of Materials*, 2004, **16**, 639-645.
60. C. Graves, *Technical University of Denmark, Roskilde, Denmark*, 2012.
61. E. Jones, T. Oliphant and P. Peterson, 2001.
62. J. D. Hunter, *Computing in Science & Engineering*, 2007, **9**, 90-95.
63. S. Van Der Walt, S. C. Colbert and G. Varoquaux, *Computing in science & engineering*, 2011, **13**, 22-30.
64. B. H. Toby and R. B. Von Dreele, *Journal of Applied Crystallography*, 2013, **46**, 544-549.
65. T. A. Schmauss, J. G. Railsback, M. Y. Lu, K. Y. Zhao and S. A. Barnett, *J Mater Chem A*, 2019, **7**, 27585-27593.
66. D. Ding, X. X. Li, S. Y. Lai, K. Gerdes and M. L. Liu, *Energy & Environmental Science*, 2014, **7**, 552-575.
67. M. Shah, P. W. Voorhees and S. A. Barnett, *Solid State Ionics*, 2011, **187**, 64-67.
68. J. Fleig, *Annual Review of Materials Research*, 2003, **33**, 361-382.
69. J. Nielsen and J. Hjelm, *Electrochimica Acta*, 2014, **115**, 31-45.
70. J. H. Shim, G. D. Han, H. J. Choi, Y. Kim, S. C. Xu, J. An, Y. B. Kim, T. Graf, T. D. Schladt, T. M. Gur and F. B. Prinz, *International Journal of Precision Engineering and Manufacturing-Green Technology*, 2019, **6**, 629-646.
71. Y. Gong, D. Palacio, X. Song, R. L. Patel, X. Liang, X. Zhao, J. B. Goodenough and K. Huang, *Nano Lett*, 2013, **13**, 4340-4345.
72. Y. Gong, R. L. Patel, X. Liang, D. Palacio, X. Song, J. B. Goodenough and K. Huang, *Chemistry of Materials*, 2013, **25**, 4224-4231.

73. M. Rahmanipour, Y. Cheng, T. M. Onn, A. Donazzi, J. M. Vohs and R. J. Gorte, *Journal of the Electrochemical Society*, 2017, **164**, F879-F884.
74. R. J. Gorte, *Cost-effective Manufacturing and Morphological Stabilization of Nanostructured cathodes for commercial SOFCs*, Univ. of Pennsylvania, Philadelphia, PA (United States), 2018.
75. H. J. Choi, K. Bae, D. Y. Jang, J. W. Kim and J. H. Shim, *Journal of the Electrochemical Society*, 2015, **162**, F622-F626.
76. Y. Chen, A. Hinerman, L. Liang, K. Gerdes, S. P. Navia, J. Prucz and X. Y. Song, *J Power Sources*, 2018, **405**, 45-50.
77. R. Küngas, A. S. Yu, J. Levine, J. M. Vohs and R. J. Gorte, *Journal of The Electrochemical Society*, 2012, **160**, F205-F211.
78. A. S. Yu, R. Kungas, J. M. Vohs and R. J. Gorte, *Journal of the Electrochemical Society*, 2013, **160**, F1225-F1231.
79. H. J. Choi, K. Bae, S. Grieshammer, G. D. Han, S. W. Park, J. W. Kim, D. Y. Jang, J. Koo, J. Son, M. Martin and J. H. Shim, *Advanced Energy Materials*, 2018, **8**, 1802506-1802506.
80. M. Shah and S. Barnett, *Solid State Ionics*, 2008, **179**, 2059-2064.
81. J. G. Railsback, H. Wang, Q. Liu, M. Y. Lu and S. A. Barnett, *Journal of The Electrochemical Society*, 2017, **164**, F3083-F3090.
82. K. Zhao, Master of Science, Northwestern University, 2016.
83. J. W. Elam, *Atomic Layer Deposition of Nanostructured Materials*, 2011, 227-249.
84. T. Keuter, N. H. Menzler, G. Mauer, F. Vondahlen, R. Vassen and H. P. Buchkremer, *Journal of Vacuum Science & Technology A*, 2015, **33**, 01A104.
85. R. L. Puurunen, W. Vandervorst, W. F. A. Besling, O. Richard, H. Bender, T. Conard, C. Zhao, A. Delabie, M. Caymax, S. De Gendt, M. Heyns, M. M. Viitanen, M. de Ridder, H. H. Brongersma, Y. Tamminga, T. Dao, T. de Win, M. Verheijen, M. Kaiser and M. Tuominen, *Journal of Applied Physics*, 2004, **96**, 4878-4889.
86. J. Liu, X. B. Meng, M. N. Banis, M. Cai, R. Y. Li and X. L. Sun, *Journal of Physical Chemistry C*, 2012, **116**, 14656-14664.
87. N. El-Atab, T. Gamze Ulusoy, A. Ghobadi, J. Suh, R. Islam, A. K. Okyay, K. Saraswat and A. Nayfeh, *Nanotechnology*, 2017, **28**, 445201.
88. D. M. Hausmann, E. Kim, J. Becker and R. G. Gordon, *Chemistry of Materials*, 2002, **14**, 4350-4358.
89. G. M. Rupp, A. Limbeck, M. Kubicek, A. Penn, M. Stoger-Pollach, G. Friedbacher and J. Fleig, *J Mater Chem A*, 2014, **2**, 7099-7108.
90. F. A. Patty, *Industrial Hygiene and Toxicology. Vol. 1.*, 1948.
91. L. Dieterle, D. Bach, R. Schneider, H. Störmer, D. Gerthsen, U. Guntow, E. Ivers-Tiffée, A. Weber, C. Peters and H. Yokokawa, *Journal of Materials Science*, 2008, **43**, 3135-3143.
92. J. Matsuda, S. Kanae, T. Kawabata, J. T. Chou, Y. Inoue, S. Taniguchi and K. Sasaki, *ECS Transactions*, 2017, **78**, 993-1001.
93. S. Molin, W. Lewandowska-Iwaniak, B. Kusz, M. Gazda and P. Jasinski, *Journal of Electroceramics*, 2012, **28**, 80-87.
94. H. Sumi, T. Ohshiro, M. Nakayama, T. Suzuki and Y. Fujishiro, *Electrochimica Acta*, 2015, **184**, 403-409.

95. H. Tu, *Solid State Ionics*, 1997, **100**, 283-288.
96. U. Holzwarth and N. Gibson, *Nat Nanotechnol*, 2011, **6**, 534.
97. J. Fleig, *J Power Sources*, 2002, **105**, 228-238.
98. C. Nicollet, A. Flura, V. Vibhu, A. Rougier, J. M. Bassat and J. C. Grenier, *International Journal of Hydrogen Energy*, 2016, **41**, 15538-15544.
99. R. Zazpe, M. Knaut, H. Sopha, L. Hromadko, M. Albert, J. Prikryl, V. Gartnerova, J. W. Bartha and J. M. Macak, *Langmuir*, 2016, **32**, 10551-10558.
100. H. Zhang, H. Liu, Y. Cong and W. Yang, *J Power Sources*, 2008, **185**, 129-135.
101. I. Micromeritics, *Journal*.
102. R. Glaser, T. Zhu, H. Troiani, A. Caneiro, L. Mogni and S. Barnett, *J Mater Chem A*, 2018, **6**, 5193-5201.
103. S. M. Ubnoske, Q. Peng, E. R. Meshot, C. B. Parker and J. T. Glass, *The Journal of Physical Chemistry C*, 2015, **119**, 26119-26127.
104. A. Atkinson, S. Barnett, R. J. Gorte, J. T. S. Irvine, A. J. McEvoy, M. Mogensen, S. C. Singhal and J. Vohs, *Nature Materials*, 2004, **3**, 17-27.
105. C. Tang, K. Kousi, D. Neagu and I. S. Metcalfe, *Chemistry*, 2021, **27**, 6666-6675.
106. Y. Liu, Z. Shao, T. Mori and S. P. Jiang, *Materials Reports: Energy*, 2021, **1**, 100003.
107. S. Joo, K. Kim, O. Kwon, J. Oh, H. J. Kim, L. J. Zhang, J. Zhou, J. Q. Wang, H. Y. Jeong, J. W. Han and G. Kim, *Angew. Chem.-Int. Edit.*, 2021, **60**, 15912-15919.
108. H. Kan and H. Lee, *Catalysis Communications*, 2010, **12**, 36-39.
109. B. Huang, S. R. Wang, R. Z. Liu and T. L. Wen, *J Power Sources*, 2007, **167**, 288-294.
110. S. Park, H. Han, J. Choi, S. Lee, M. Park and W. B. Kim, *Energy Technology*, 2021, **9**, 2100116.
111. M. Qin, T. Tan, K. Li, Z. Wang, H. Yang, Z. Liu, M. Zhou, T. Liu, C. Yang and M. Liu, *International Journal of Hydrogen Energy*, 2020, **45**, 21464-21472.
112. T. Tan, M. Qin, K. Li, M. Zhou, T. Liu, C. Yang and M. Liu, *International Journal of Hydrogen Energy*, 2020, **45**, 29407-29416.
113. O. Kwon, S. Joo, S. Choi, S. Sengodan and G. Kim, *Journal of Physics: Energy*, 2020, **2**.
114. T. Cao, O. Kwon, R. J. Gorte and J. M. Vohs, *Nanomaterials (Basel)*, 2020, **10**.
115. F. Liu, L. Zhang, G. Huang, B. Niu, X. Li, L. Wang, J. Zhao and Y. Jin, *Electrochimica Acta*, 2017, **255**, 118-126.
116. Y. Cao, Z. Zhu, Y. Zhao, W. Zhao, Z. Wei and T. Liu, *J Power Sources*, 2020, **455**, 227951.
117. L. Bian, C. Duan, L. Wang, L. Zhu, R. O'Hayre and K.-C. Chou, *J Power Sources*, 2018, **399**, 398-405.
118. M. Chen, D. Chen, M. Chang, H. Hu and Q. Xu, *Journal of The Electrochemical Society*, 2017, **164**, F405-F411.
119. W. Ni, T. Zhu, X. Chen, Q. Zhong and W. Ma, *J Power Sources*, 2020, **451**.
120. W. Ni, T. Zhu, X. Chen, C. Jin, Y. Bu, Q. Zhong and M. Han, *J Power Sources*, 2021, **489**, 229490.
121. M. Santaya, H. E. Troiani, A. Caneiro and L. V. Mogni, *ACS Applied Energy Materials*, 2020, **3**, 9528-9533.
122. S.-L. Zhang, D. Cox, H. Yang, B.-K. Park, C.-X. Li, C.-J. Li and S. A. Barnett, *J Mater Chem A*, 2019, **7**, 21447-21458.

123. S.-L. Zhang, H. Wang, M. Y. Lu, A.-P. Zhang, L. V. Mogni, Q. Liu, C.-X. Li, C.-J. Li and S. A. Barnett, *Energy & Environmental Science*, 2018, **11**, 1870-1879.
124. H. Zhang, T. Wang, X. Chen and W. Zhu, *Particuology*, 2016, **24**, 210-215.
125. J. Wang, J. Yang, A. K. Opitz, W. Bowman, R. Bliem, G. Dimitrakopoulos, A. Nenning, I. Waluyo, A. Hunt, J.-J. Gallet and B. Yildiz, *Chemistry of Materials*, 2021, **33**, 5021-5034.
126. E. M. Levin, C. R. Robbins and H. F. McMurdie, 1969.
127. T. G. Kollie, *Physical Review B*, 1977, **16**, 4872-4881.
128. M. Hayase, M. Shiga and Y. Nakamura, *Journal of the Physical Society of Japan*, 1973, **34**, 925-931.
129. N. Ridley and H. Stuart, *Journal of Physics D: Applied Physics*, 1968, **1**, 1291-1295.
130. S. Gates-Rector and T. Blanton, *Powder Diffraction*, 2019, **34**, 352-360.
131. S. K. Wilke and D. C. Dunand, *J Power Sources*, 2020, **448**, 227463.
132. L. Swartzendruber, V. Itkin and C. Alcock, *Journal of phase equilibria*, 1991, **12**, 288-312.
133. H. S. Kim, Y. Jeon, J. H. Kim, G. Y. Jang, S. P. Yoon and J. W. Yun, *Applied Surface Science*, 2020, **510**, 145450.
134. B. Li, S. He, J. Li, X. Yue, J. T. S. Irvine, D. Xie, J. Ni and C. Ni, *ACS Catalysis*, 2020, **10**, 14398-14409.
135. T. A. Schmauss and S. A. Barnett, *Acs Energy Lett*, 2021, **6**, 3180-3184.
136. E. Larson, C. Greig, J. Jenkins, E. Mayfield, A. Pascale, C. Zhang, Drossman, R. Williams, S. Pacala, R. Socolow, R. B. EJ Baik, R. Duke, R. Jones, B. Haley, E. Leslie, K. Paustian and A. Swan, *Net-Zero America: Potential Pathways, Infrastructure, and Impacts, interim report*, Princeton University, Princeton, NJ, 2020.
137. L. Tock and F. Maréchal, *International Journal of Hydrogen Energy*, 2012, **37**, 11785-11795.
138. E. W. Lemmon, I. H. Bell, M. L. Huber and M. O. McLinden, *Standard Reference Data Program*, 2018.
139. P. Boldrin and N. P. Brandon, *Nature Catalysis*, 2019, **2**, 571-577.
140. *Bloom and Samsung Heavy Industries plan SOFCs for ship power*, Report 1464-2859, 2019.
141. Doosan Fuel Cell and Korea Shipbuilding & Marine Engineering promote joint development of fuel cells for ships, https://www.doosanfuelcell.com/kr/media-center/medi-0101_view/?id=76&page=0&).
142. F. Baldi, S. Moret, K. Tammi and F. Maréchal, *Energy*, 2020, **194**, 116811.
143. J. Lin, T. A. Trabold, M. R. Walluk and D. F. Smith, *International Journal of Hydrogen Energy*, 2013, **38**, 12024-12034.
144. F. Müller-Langer, S. Majer and S. O'Keeffe, *Energy, Sustainability and Society*, 2014, **4**, 20.
145. F. Sabatino, A. Grimm, F. Gallucci, M. van Sint Annaland, G. J. Kramer and M. Gazzani, *Joule*, 2021, DOI: https://doi.org/10.1016/j.joule.2021.05.023.
146. R. Schmuch, R. Wagner, G. Hörpel, T. Placke and M. Winter, *Nature Energy*, 2018, **3**, 267-278.
147. *Weight and Balance Handbook (FAA-H-8083-1B)*, U.S. Department of Transportation, Federal Aviation Administration, 2016.

148. P. J. Linstrom and W. G. Mallard, *NIST Chemistry WebBook, NIST Standard Reference Database Number 69*, DOI: 10.18434/T4D303.
149. Panasonic Lithium Ion NCR1850B Specifications Sheet, https://web.archive.org/web/20181010095526/https://na.industrial.panasonic.com/sites/default/pidsa/files/ncr18650b.pdf, (accessed August 2020).
150. H. Hao, Y. Geng, J. E. Tate, F. Liu, K. Chen, X. Sun, Z. Liu and F. Zhao, *Nat Commun*, 2019, **10**, 5398.
151. Specifications Sheet, Wärtsilä Aframax WSD42 111K Tanker, https://web.archive.org/web/20200727212125/https://cdn.wartsila.com/docs/default-source/product-files/sd/merchant/tankers/data-sheet-ship-design-aframax-tanker-wsd-42-111k.pdf, (accessed July 2020).
152. Improving efficiency, https://web.archive.org/web/20210206180131/https://www.wartsila.com/sustainability/innovating-for-sustainable-societies/improving-efficiency, (accessed February 2021).
153. F. F. Yang, D. Wang, Y. Zhao, K. L. Tsui and S. J. Bae, *Energy*, 2018, **145**, 486-495.
154. Z. Salameh, in *Renewable Energy System Design*, ed. Z. Salameh, Academic Press, Boston, 2014, DOI: 10.1016/b978-0-12-374991-8.00004-0, pp. 201-298.
155. Fuels - Higher and Lower Calorific Values, https://www.engineeringtoolbox.com/fuels-higher-calorific-values-d_169.html, (accessed February 2021).
156. E. Bannon, *Electrofuels? Yes, we can … if we're efficient: Decarbonising the EU's transport sector with renewable electricity and electrofuels*, Transport & Environment, 2020.
157. *Tesla, Inc. Request for issuance of a new certificate of Conformity – Running change to add Model S 100D and New 75 kWh FW limited battery pack configuration*, 2017.
158. Toyota 2020 Mirai, https://web.archive.org/web/20210205231035/https://www.toyota.com/content/ebrochure/2020/mirai_fuelcelltech.pdf).
159. Wärtsilä X62, http://web.archive.org/web/20210206181026/https://cdn.wartsila.com/docs/default-source/product-files/engines/ls-x-engine/wartsila-o-e-ls-x62.pdf?sfvrsn=4, (accessed February 2021).
160. Tesla Model S Drive Unit - Starter Kit, https://web.archive.org/web/20210205225156/https://www.evwest.com/catalog/product_info.php?cPath=&products_id=476, (accessed February 2021).
161. Average Fuel Efficiency of U.S. Light Duty Vehicles, https://www.bts.gov/content/average-fuel-efficiency-us-light-duty-vehicles, (accessed February 2021).
162. Alternative Fuels Data Center – Fuel Properties Comparison, https://afdc.energy.gov/fuels/fuel_comparison_chart.pdf, (accessed August 2020).
163. Appendix A - Miscellaneous Data and Conversion Factors, https://www3.epa.gov/ttnchie1/ap42/appendix/appa.pdf, (accessed February 2021).
164. New Tesla Model S Now the Quickest Production Car in the World, https://www.tesla.com/blog/new-tesla-model-s-now-quickest-production-car-world, February 2021).

165. Toyota Introduces Second-Generation Mirai Fuel Cell Electric Vehicle as Design and Technology Flagship Sedan, https://web.archive.org/web/20210126062132/https://pressroom.toyota.com/toyota-introduces-second-generation-mirai-fuel-cell-electric-vehicle-as-design-and-technology-flagship-sedan/, (accessed February 2021).
166. J. J. Botti, M. J. Grieve and J. A. MacBain, *SAE100: SAE TECHNICAL PAPER SERIES*, 2005, **01-1172**, 1-13.
167. J. C. Minx, W. F. Lamb, M. W. Callaghan, S. Fuss, J. Hilaire, F. Creutzig, T. Amann, T. Beringer, W. de Oliveira Garcia, J. Hartmann, T. Khanna, D. Lenzi, G. Luderer, G. F. Nemet, J. Rogelj, P. Smith, J. L. Vicente Vicente, J. Wilcox and M. del Mar Zamora Dominguez, *Environmental Research Letters*, 2018, **13**, 063001.
168. R. K. Ahluwalia and X. Wang, *J Power Sources*, 2005, **139**, 152-164.
169. P. Brooker, *U.S. Department of Transportation's University Transportation Centers Program*, 2015, 1-11.
170. M. J. Kim and H. Peng, *J Power Sources*, 2007, **165**, 819-832.
171. R. Mauldin, Y. Baghzouz and R. F. Boehm, presented in part at the SPEEDAM 2006: International Symposium on Power Electronics, Electrical Drives, Automation and Motion, 2006.
172. E. Wood, L. J. Wang, J. Gonder and M. Ulsh, *Sae International Journal of Commercial Vehicles*, 2013, **6**, 563-574.
173. Z. Dimitrova and F. Marechal, *Renewable Energy*, 2017, **112**, 124-142.
174. K. Rajashekara, J. A. MacBain and M. J. Grieve, presented in part at the SPEEDAM 2006: International Symposium on Power Electronics, Electrical Drives, Automation and Motion, 2006.
175. Nissan, *Fuel Cells Bulletin*, 2016, **2016**, 2-3.
176. W. A. Poe and S. Mokhatab, in *Modeling, Control, and Optimization of Natural Gas Processing Plants*, eds. W. A. Poe and S. Mokhatab, Gulf Professional Publishing, Boston, 2017, DOI: 10.1016/b978-0-12-802961-9.00001-2, pp. 1-72.
177. A. Sharafian and M. Bahrami, *Renewable & Sustainable Energy Reviews*, 2014, **30**, 440-451.
178. E. D. Wachsman and K. T. Lee, *Science*, 2011, **334**, 935-939.
179. 2017 Mirai Product Information: Mirai Fuel Cell Vehicle, https://www.toyota.com/mirai/assets/core/Docs/Mirai%20Specs.pdf, (accessed July 2020).
180. R. Payne, J. Love and M. Kah, presented in part at the SOFC-11, 2009.
181. Y. B. Lin, Z. L. Zhan, J. Liu and S. A. Barnett, *Solid State Ionics*, 2005, **176**, 1827-1835.
182. M. R. Pillai, I. Kim, D. M. Bierschenk and S. A. Barnett, *J Power Sources*, 2008, **185**, 1086-1093.
183. E. P. Murray, T. Tsai and S. A. Barnett, *Nature*, 1999, **400**, 649-651.
184. M. C. Steil, S. D. Nobrega, S. Georges, P. Gelin, S. Uhlenbruck and F. C. Fonseca, *Applied Energy*, 2017, **199**, 180-186.
185. Z. L. Zhan and S. A. Barnett, *Solid State Ionics*, 2005, **176**, 871-879.
186. S. Park, J. M. Vohs and R. J. Gorte, *Nature*, 2000, **404**, 265-267.
187. Z. Zhan and S. A. Barnett, *Science*, 2005, **308**, 844-847.

188. S. Sengodan, R. Lan, J. Humphreys, D. W. Du, W. Xu, H. T. Wang and S. W. Tao, *Renewable & Sustainable Energy Reviews*, 2018, **82**, 761-780.
189. J. Rechberger, A. Kaupert, J. Hagerskans and L. Blum, *Transport Research Arena Tra2016*, 2016, **14**, 3676-3685.
190. M. D. Fernandes, S. T. D. Andrade, V. N. Bistritzki, R. M. Fonseca, L. G. Zacarias, H. N. C. Goncalves, A. F. de Castro, R. Z. Domingues and T. Matencio, *International Journal of Hydrogen Energy*, 2018, **43**, 16311-16333.
191. J. Rechberger, M. Reissig and V. Lawlor, Wiesbaden, 2018.
192. D. Udomsilp, J. Rechberger, R. Neubauer, C. Bischof, F. Thaler, W. Schafbauer, N. H. Menzler, L. G. J. de Haart, A. Nenning, A. K. Opitz, O. Guillon and M. Bram, *Cell Reports Physical Science*, 2020, **1**.
193. J. Nielsen, A. H. Persson, T. T. Muhl and K. Brodersen, *Journal of the Electrochemical Society*, 2018, **165**, F90-F96.
194. W. Kempton and J. Tomic, *J Power Sources*, 2005, **144**, 268-279.
195. M. B. Mogensen, M. Chen, H. L. Frandsen, C. Graves, J. B. Hansen, K. V. Hansen, A. Hauch, T. Jacobsen, S. H. Jensen, T. L. Skafte and X. Sun, *Clean Energy*, 2019, **3**, 175-201.
196. S. H. Jensen, C. Graves, M. Mogensen, C. Wendel, R. Braun, G. Hughes, Z. Gao and S. A. Barnett, *Energy Environ. Sci.*, 2015, **8**, 2471 - 2479.
197. K. Hashimoto, N. Kumagai, K. Izumiya, H. Takano and Z. Kato, *Energy Sustainability and Society*, 2014, **4**, 17.
198. S. Bajohr, M. Bargende, T. Block, J. Brellochs, H. Eichlseder, V. Frick, H. Gosda, F. Graf, E. Hammer, J. Hochi, O. Jochum, M. Klemm, J. Krassowski, F. Müller-Langer, R. Otten, M. Schlüter, R. Schultz, M. Specht, B. Stürmer, A. Wolany, N. T. Zimmermann and U. Zuberbühler, in *Natural Gas and Renewable Methane for Powertrains: Future Strategies for a Climate-Neutral Mobility*, ed. R. van Basshuysen, Springer International Publishing, 2016, DOI: 10.1007/978-3-319-23225-6, p. 482.
199. D. M. Bierschenk, J. R. Wilson and S. A. Barnett, *Energy & Environmental Science*, 2011, **4**, 944-951.
200. R. W. J. Edwards and M. A. Celia, *Proceedings of the National Academy of Sciences*, 2018, **115**, E8815-E8824.

Vita

Travis Anthony Schmauss attended Los Osos High School in Rancho Cucamonga, California, and went on to attend Johns Hopkins University in Baltimore, Maryland, graduating in 2016 with a Bachelor of Science in Materials Science and Engineering. There he worked in the Timothy P. Weihs research group focusing on reactive Al:Zr and Al-8Mg:Zr bi-metallic sputtered and ball-milled powders. At Northwestern he joined the Scott Barnett research group in pursuit of his Ph.D., again in Materials Science and Engineering. Extracurricularly, he was co-president of the Materials Science Student Association and the president of the Northwestern Energy Technology Group, now the Northwestern Climate Technology Club.